

1-1-2012

Abrasive Jet Micro-Machining Of Polymeric Materials

Getu Hailu
Ryerson University

Follow this and additional works at: <http://digitalcommons.ryerson.ca/dissertations>

 Part of the [Mechanical Engineering Commons](#)

Recommended Citation

Hailu, Getu, "Abrasive Jet Micro-Machining Of Polymeric Materials" (2012). *Theses and dissertations*. Paper 1393.

This Dissertation is brought to you for free and open access by Digital Commons @ Ryerson. It has been accepted for inclusion in Theses and dissertations by an authorized administrator of Digital Commons @ Ryerson. For more information, please contact bcameron@ryerson.ca.

ABRASIVE JET MICRO-MACHINING OF POLYMERIC MATERIALS

by

Getu Hailu

Dipl. Ing., Slovak Technical University, Bratislava, Slovakia, 1997

M.A.Sc. Ryerson University, Toronto, Canada, 2007

A dissertation

presented to Ryerson University

in partial fulfillment of the
requirements for the degree of

Doctor of Philosophy

in the program of

Mechanical Engineering

Toronto, Ontario, Canada, 2012

© Getu Hailu 2012

AUTHOR'S DECLARATION

I hereby declare that I am the sole author of this dissertation. This is a true copy of the dissertation, including any required final revisions, as accepted by my examiners.

I authorize Ryerson University to lend this dissertation to other institutions or individuals for the purpose of scholarly research.

I further authorize Ryerson University to reproduce this dissertation by photocopying or by other means, in total or in part, at the request of other institutions or individuals for the purpose of scholarly research.

I understand that my dissertation may be made electronically available to the public.

ABSTRACT

Abrasive Jet Micro-machining of Polymeric Materials

Doctor of Philosophy, 2012

Getu Hailu

Mechanical Engineering

Ryerson University

In the abrasive jet micro-machining (AJM) process, a jet of small particles is directed through an erosion resistant mask opening so that micro-sized features (i.e., micro-channels, holes, etc.) can be machined for the fabrication of micro-devices such as micro-fluidic and micro-electro-mechanical-systems (MEMS). Polymeric materials and elastomers have found applications in a wide variety of micro-devices. This thesis investigates the AJM of such materials, addressing the major challenges that must be overcome in order for the process to gain wider acceptance in industry. The thesis first presents a novel cryogenically assisted abrasive jet micro-machining (CAJM) technique that enables the micro-machining of elastomers such as polydimethylsiloxane (PDMS) that cannot be machined at room temperature. It was found that the erosion rate during CAJM is greatly increased, and the degree of particle embedment greatly decreased, compared to room temperature experiments. A finite element (FE) analysis was used to investigate the relationships between erosion, the heat transfer of the cooling jet and the resulting target temperature during the CAJM of channels in PDMS. The analysis illustrated the asymmetric nature of the cooling with much more cooling occurring towards the trailing edge of the jet. It was found that the predicted shape of the evolving

machined surface profiles was improved significantly when a FE model was used to account for thermal distortion occurring during the CAJM process.

An unwanted consequence of the AJM of polymeric materials was found to be particle embedding. Criteria leading to the embedding of spherical and angular particles in such materials were identified and modelled using rigid plastic analyses. It was found that the likelihood of embedding was proportional to the static coefficient of friction between the particle and the target for angular particles, and the depth of penetration for spherical particles.

Scanning electron microscopy with EDX was used to measure the area coverage of embedded Al_2O_3 particles in polymers and elastomers, in order to evaluate various cleaning methods that were developed. It was found that glass bead blasting at 45° followed by the freezing technique was the best method to remove embedded particles, leading to 100% removal in some cases.

AKNOWLEDGEMENTS

First and foremost I am heartily thankful to my supervisors Dr. Marcello Papini and Dr. J.K. Spelt for their enthusiastic guidance, support, great insights and perspectives from the initial to the final level of this project. I appreciate all their contributions of time and ideas to make my graduate experience productive and stimulating. One simply could not wish for better or friendlier supervisors.

I am grateful to Joseph Amankrah and Qiang Li for their technical support during various stages of this research. I am grateful to Prof. V. Chan for allowing me to use the static charge remover.

I would like to thank Ryerson University, the Vanier Canada Graduate Scholarship program and The Ministry of Training, Colleges and Universities for financial support through the Ontario Graduate Scholarship (OGS) program.

This research was supported with funding from the Natural Sciences and Engineering Research Council of Canada (NSERC) and Canada Research Chairs Program.

Last but not least I would like to thank my wife, Maria, for her unconditional love, relentless support, encouragement and trust in whatever I do.

DEDICATION

To my grandfather

TABLE OF CONTENTS

AUTHOR'S DECLARATION	ii
ABSTRACT	iii
AKNOWLEDGEMENTS	v
DEDICATION	vi
TABLE OF CONTENTS	vii
LIST OF TABLES	xi
LIST OF FIGURES	xiii
LIST OF APPENDICES	xxi
NOMENCLATURE	xxii
1 Introduction.....	1
1.1 Motivation.....	3
1.2 Thesis Objectives.....	6
1.3 Thesis Organization.....	7
2 Literature Review.....	9
2.1 Solid Particle Erosion of Polymers and Elastomers.....	9
2.1.1 Process Parameters Affecting the Solid Particle Erosion of Polymers.....	10
2.1.1.1 Particle Shape and Size.....	11
2.1.1.2 Particle Hardness.....	11
2.1.1.3 Erodent Velocity.....	12
2.1.1.4 Particle Flux.....	12
2.1.1.5 Impact Angle.....	13
2.1.2 Target Material Parameters Affecting the Solid Particle Erosion of Polymers ..	13
2.1.2.1 Mechanical Properties.....	13
2.1.2.2 Morphological Properties.....	16
2.1.2.3 Thermal Properties.....	17
2.2 Abrasive Jet Micro-machining of Polymers.....	18
2.3 Particle Embedding during Solid Particle Erosion.....	20

2.4	Chapter Summary.....	24
3	Experimental Apparatus Used for AJM and Solid Particle Erosion Experiments....	26
3.1	Experimental Setup	26
3.2	Masks	29
3.3	Nozzles.....	30
3.4	Particle and Machined Feature Characterization	31
4	Cryogenically Assisted Abrasive Jet Micro-machining (CAJM)	35
4.1	Cryogenic Abrasive Jet Micro-machining Apparatus.....	35
4.2	Experiments.....	38
4.2.1	Erosion Rate Measurements.....	39
4.2.2	Masked Micro-channels and Holes.....	41
4.3	Results and Discussion.....	41
4.3.1	Erosion Rate Measurements.....	41
4.3.1.1	Erosion Rate Measurements of ABS.....	41
4.3.1.2	Erosion Rate Measurements of PDMS.....	46
4.3.1.3	Erosion Rate Measurements of PTFE	49
4.3.2	Masked Channels and Holes	53
4.4	Chapter Summary.....	58
5	Thermal Analysis of Cryogenically Assisted Abrasive Jet Micro-machining of PDMS.....	59
5.1	Experiments.....	60
5.1.1	CAJM Experiments.....	60
5.2	Heat Transfer Analysis of CAJM for PDMS Targets	61
5.2.1	CAJM of holes in PDMS: Stationary Heat Sink.....	62
5.2.2	CAJM of Unmasked Channels in PDMS: Moving Heat Sink	66
5.2.2.1	FE Model of Moving Heat Sink.....	67
5.2.2.2	Verification of Model.....	71
5.2.2.3	Surface Temperature Distribution along Scanning Direction for Unmasked Channels.....	73
5.2.3	CAJM of Masked Channels in PDMS: Moving Heat Sink.....	77

5.3	Surface Evolution in CAJM.....	79
5.3.1	Case I: Model without Thermal Strain.....	79
5.3.2	Case II: Model Including Thermal Strain	83
5.3.3	CAJM of Other Features	88
5.4	Chapter Summary.....	91
6	Conditions Leading to Embedding of Angular and Spherical Particles during the Solid Particle Erosion of Polymers	92
6.1	Experiments.....	92
6.1.1	Erodent and Target Materials.....	92
6.1.2	Particle Impact Experiments	94
6.1.3	Dynamic Hardness Measurements	97
6.2	Models for Particle Embedding.....	99
6.2.1	Model for Embedding of Angular Particles	99
6.2.2	Angular Particle Embedding Criteria-Analysis.....	105
6.2.3	Angular Particles Embedding Criteria: Comparison with Experimental Results	108
6.2.4	Model for Embedding of Spherical Particles	114
6.2.5	Spherical Particle Embedding Criteria-Comparison with Experimental Results	115
6.3	Chapter Summary.....	121
7	Reduction of Particle Embedding in Solid Particle Erosion of Polymers.....	122
7.1	Experiments.....	122
7.1.1	Materials.....	122
7.1.2	Machining Experiments	123
7.1.3	Methodologies for Removal of Embedded Particles.....	124
7.1.4	Surface Evaluation Methods	126
7.2	Results and Discussion.....	129
7.2.1	Particle Embedding in PMMA.....	129
7.2.2	Particle Embedding in PDMS, PTFE and ABS with Cryogenic AJM.....	134
7.3	Chapter Summary.....	139

8	Conclusions and Future Work.....	140
8.1	Summary of Useful Findings	140
8.1.1	Novel Cryogenic AJM	140
8.1.2	Particle Embedding Following Solid Particle Erosion.....	141
8.2	Original Contributions.....	143
8.3	Recommendations for Future Work.....	144
9	Appendices.....	147
10	References	183

LIST OF TABLES

Table 5-1 Comparison of measured temperatures at the center of an unmasked channel with the corresponding FE-predicted results at different scan speeds.	72
Table 5-2 Comparison of root-mean-square errors of the predicted channel profiles for Case I (Fig. 5.11, no thermal strain) and Case II (Fig. 5.13, thermal strain) models.	87
Table 5-3 Comparison of channel depths (Z) predicted ignoring thermal strain (Case I, Fig. 5.11), and considering thermal strain (Case II, Fig. 5.13) with experimentally measured depths at channel center ($Y=0$) and at $Y=150\ \mu\text{m}$	88
Table 6-1 Dynamic hardness values of target polymers	98
Table 6-2 Comparison of the predicted fraction of embedded particles (Model P) with the experimentally measured results (Expt P). μ - coefficient of static friction value determined using comparison with experimental data at 90° then used to model P at 60° and 30° ; A - particle angularity; Diff - difference between experimentally measured and predicted fraction of embedded particles.	110
Table 6-3 Particle and target material properties. Subscripts 1 and 2 are for target and particle, respectively. * Values obtained from [33]. ** Values obtained from [129].	114
Table 7-1 Fractional area coverage of Al_2O_3 particles (\pm the standard deviation of 5 measurements) after 1-4 passes of the nozzle in PMMA before and after post blasting with glass beads. Removal efficiency defined as: $100 \times (\text{area coverage before glass bead blasting} - \text{area coverage after glass bead blasting}) / (\text{area coverage before glass bead blasting})$	130
Table 7-2 Fractional area coverage of Al_2O_3 particles (\pm the standard deviation of 5 measurements) after cleaning procedures described in Section 7.1.3 were applied to 4-pass machined PMMA samples. Removal efficiency = $100 \times (\text{area coverage after blasting with glass bead at } 45^\circ - \text{area coverage after cleaning procedure}) / (\text{area coverage after blasting with glass bead at } 45^\circ)$	132

Table 7-3 Average channel cross-sectional area (\pm the standard deviation of measurements of 3 sections) of PMMA target material removed when machining unmasked channels at 0.5 mm/s before and after preconditioning with embedding particles as described in Section 7. 1. 2(b). From each sample, 5 representative 0.25 x 0.2 mm areas were used to calculate the average (plus or minus the standard deviation) fractional area covered by Al ₂ O ₃ particles after preconditioning.	133
Table 7-4 Percentage area covered by embedded Al ₂ O ₃ particles (\pm the standard deviation of 5 measurements) after AJM with and without the use of LN ₂	134
Table 7-5 Percentage area covered by Al ₂ O ₃ in ABS, PDMS and PTFE before and after cleaning the samples that had been machined using LN ₂ . Glass bead blasting (GB) at 45° -7.1.3(i); GB at 45° followed by application of PVC adhesive tape – 7.1.3(iv); GB at 45° followed by distilled H ₂ O wetting and freezing – 7.1.3(v); GB at 45° followed by NaOH wetting and freezing – 7.1.3(vi).....	135
Table G 1 Summary of measured particle sizes and aspect ratios. Numbers in brackets indicate the number of particles measured. Diff.: Difference, Clemex: measured using optical size analyzer, Diff=2 x abs(Clemex-Shadowgraphy)/Clemex+Shadowgraphy).....	176

LIST OF FIGURES

Figure 1.1 Typical AJM process	1
Figure 3.1 Typical abrasive jet micro-machining experimental set-up.....	27
Figure 3.2 Detail A: Experimental apparatus, MB1005 and its parts.	27
Figure 3.3 Detail B: Experimental apparatus, computer controlled linear stage.	28
Figure 3.4 Masking device for channel machining.....	29
Figure 3.5 Metal masks for fabricating micro-holes.....	30
Figure 3.6 Nozzles: (a) a round nozzle (760 μm inside diameter) used for erosion rate measurements and machining unmasked channels, (b) round nozzle (1.5mm inside diameter) used for particle impact experiments and (c) Rectangular (0.3 mm x 3.8 mm) slot nozzle used for machining masked channels and holes.....	30
Figure 3.7 Schematic of the laser shadowgraphy experimental setup for measurement of particle size and velocity distribution.....	32
Figure 3.8 Clemex PS3 particle size analyser.....	33
Figure 3.9 NANOVEA ST400 optical profilometer.....	34
Figure 4.1 Cryogenic abrasive jet micro-machining setup.	36
Figure 4.2 Schematic of the LN ₂ pressurizing and dispensing equipment.....	36
Figure 4.3 Schematic of LN ₂ injection to the abrasive jet during CAJM process.	37
Figure 4.4 Al ₂ O ₃ particles used in the experiments.	38
Figure 4.5 Erosion rate of ABS as a function of impact angle, with and without using LN ₂ . Experimental conditions: 25 μm Al ₂ O ₃ particles, 760 μm round nozzle, abrasive jet pressure of 200 kPa, LN ₂ pressure of 170 kPa, nozzle centreline to surface distance of 20 mm. Error bars represent \pm standard error of the mean.	42
Figure 4.6 EDX analysis of surfaces when machining ABS with and without using LN ₂ at 90° impact angle. White dots are embedded Al ₂ O ₃ particles.	44
Figure 4.7 Average area coverage by Al ₂ O ₃ particles between samples machined without and with LN ₂ . The error bars show the standard error (the deviation of the mean value) based on three randomly selected representative, 0.5x0.5 mm areas, as explained in Section 4.3.1.1.	45

Figure 4.8 Erosion rate of PDMS as a function of impact angle, with and without using LN ₂ .	47
Figure 4.9 Individual impact site (a) in PDMS under cryogenic conditions and (b) in glass at room temperature condition showing similar micro-chipping mechanism of material removal.	48
Figure 4.10 Erosion rate of PTFE as a function of impact angle, with and without using LN ₂ .	50
Figure 4.11 PTFE sample machined with (a) brown Al ₂ O ₃ and (b) with white Al ₂ O ₃ . Machined under ambient temperature conditions at 90° impact.	52
Figure 4.12 Three dimensional profiles of channels and holes micro-machined in three polymers using CAJM. Experimental conditions: LN ₂ pressure of 170 kPa, rectangular 0.3 mm x 3.8 mm slot nozzle launching 25 μm Al ₂ O ₃ particles at normal incidence, abrasive mass flow rate of 5.21 g/min, abrasive jet pressure of 200 kPa. Channel profiles shown after ten 1 mm/s passes and hole profiles shown after eight 0.5 mm/s passes.	54
Figure 4.13 Cross sectional profiles of: (a) channels and (b) holes machined using CAJM.	56
Figure 5.1 Temperature at different depths within the target as a function of time for a stationary cooling jet predicted by Eq. (5. 5). The depth into the surface is measured from the front side of the target; i.e. from the surface on which the jet impinges. The bold solid horizontal line shows the glass transition temperature (T_g) of PDMS (-120°C).	64
Figure 5.2 Depth into the PDMS target of thermal front at $T_g=-120$ °C predicted by Eq. (5. 5), and location of erosion front (based on maximum etch rate) as a function of time. Zero depth corresponds to the surface once it reached -120°C and erosion began.	65
Figure 5.3 Leading and trailing edges of scanning abrasive/cooling jet.	67
Figure 5.4 Schematic of the moving circular heat sink and the meshed half model exploiting symmetry. C is the distance between two sets of elements. The semi-	

circles show areas to which h and T are applied as the heat sink moves in the positive X -direction. Zero heat flux was assumed on the plane of symmetry.	68
Figure 5.5 Gaussian distribution of the heat transfer coefficient, h , over the 6 mm diameter impingement area estimated using the correlation of [104].	69
Figure 5.6 Temperature distribution in PDMS predicted by the analytical and finite element models at the surface along the direction of motion (X -axis) through the center of the circular cooling jet ($Y=0$) for $q''=9500 \text{ W/m}^2$, $r=3 \text{ mm}$. $X=0$ represents the center of the moving jet.	73
Figure 5.7 Temperature distribution in PDMS predicted by the finite element model at the surface along the direction of motion (X -axis) for different scan speeds through the center of the circular cooling jet ($Y=0$). The bold solid horizontal line shows the glass transition temperature (T_g) of PDMS (-120°C). $X=0$ represents the center of the moving jet and negative X corresponds to material in the wake of the jet.	75
Figure 5.8 Schematic of the moving rectangular heat sink and the meshed half model exploiting symmetry.	77
Figure 5.9 FE predicted temperature distributions in masked PDMS samples at the surface along the direction of motion (X -axis) and through the center of the mask opening ($Y=0$), for different scan speeds. The Gaussian convective heat transfer coefficient distribution was used. $X=0$ represents the center of the moving jet.	78
Figure 5.10 Coordinates for channel cross-sectional profiles. α is the angle between the Z -component of the particle velocity vector, v , and the tangent to the channel surface in the Z - Y plane.	81
Figure 5.11 Case I: Measured and predicted micro-channel profiles for CAJM of PDMS. Predictions based on the measured first pass profile at room temperature to obtain $\gamma^*(Y^*)$. CAJM conditions: slot nozzle (0.3 mm x 3.8 mm), 0.5 mm/s scan speed.	83
Figure 5.12 Two-dimensional finite element mesh of the cold PDMS profile between the masks after the first pass under the LN_2 cooled jet. Model width was 500 μm and height was 4 mm.	84

Figure 5.13 Case II: Measured and predicted surface profiles solved using the cold profile of the first pass $\gamma^*(Y^*)$. $E=615$ kPa, $\nu=0.49$, CAJM conditions: slot nozzle (0.3 mm x 3.8 mm), 0.5 mm/s scan speed.	86
Figure 5.14 Mesh of a PDMS sample 5 cm long x 4 mm thick constrained at the ends. .	89
Figure 5.15 Surface profiles of PDMS after one cryogenic machining pass at two temperatures: Solid line shows profile measured at room temperature. Dashed line shows the predicted shape of the same profile after having been thermally deformed by cooling to -150 °C.	90
Figure 6.1 Images of 136 μm garnet particles using: (a) 3D SEM stereo reconstruction, (b) SEM viewed at 75° from the plane of the holder.	94
Figure 6.2 SEM micrographs of embedded particles incident to surface at 90° in: (a) LDPE, (c) ABS, and (d) PMMA. (b) shows EDX map of Fe confirming presence of embedded particles in LDPE.	97
Figure 6.3 Geometry and orientation of indenting particles: θ - initial particle orientation; α - impact angle; V_i - initial velocity; A - particle angularity; h - particle side length.	100
Figure 6.4 Shadowgraphy measurements of particle size distribution (equivalent diameter) for 136 μm and 103 μm nominal size garnet particles.	101
Figure 6.5 Shadowgraphy measurements of aspect ratio (d/D , Fig. 6.3) of 136 μm and 103 μm nominal size garnet particles.	102
Figure 6.6 Shadowgraphy measurements of velocity distribution of 136 μm 103 μm nominal size garnet particles.	103
Figure 6.7 Particles in flight as they exit the nozzle during shadowgraphic measurement.	104
Figure 6.8 Forces acting on the left and right sides of an angular particle in full contact along both faces when it begins the rebound phase of contact. F_{ne}^L and F_{ne}^R are the elastic normal forces, F_{te}^L and F_{te}^R are the tangential elastic forces.	106
Figure 6.9 Minimum velocities that caused embedding in PMMA as a function of the particle orientation, θ , (Fig. 6. 8) at different impact angles (α) using 136 μm garnet particles.	113

Figure 6.10 (a) Predicted trajectory of steel sphere impacting a polyethylene target at (a) 35° impact angle and 288 m/s velocity, 4 mm particle diameter; (b) at 70° impact angle and 260 m/s incident velocity, 2 mm particle diameter. The target surface is at Z=0, and the trajectory is modeled from first contact to the point at which the particle comes to rest.....	117
Figure 6.11 Comparison of model and experimental [33] results for embedding of 4 mm diameter steel spheres in polyethylene. Δ: measured incident velocities that resulted in embedding [33]; □: predicted incident velocities that resulted in embedding with rigid plastic model; ×: predicted incident velocities that resulted in embedding, elastic-plastic model.....	118
Figure 6.12 Comparison of predicted (elastic-plastic model) and measured [33] indentation depths at 90°	120
Figure 7.1(a) EDX mapping of Al in PMMA; white areas represent aluminum, and (b) final area coverage of aluminum oxide obtained from image processing.....	127
Figure 7.2 SEM of embedded particles in PDMS. Blasting conditions as described in Section 7.1.2(a)	128
Figure 7.3 (a) Embedded Al ₂ O ₃ particle in PDMS. Blasting conditions as described in Section 7.1.2(a) under cryogenic conditions, (b) energy dispersive X-ray analysis of PDMS sample blasted with alumina particles showing dominant Al peak due to embedding of Al ₂ O ₃ particle	136
Figure 7.4 Development of composite layer in ABS during AJM. Cross-sections through the surface region after increasing numbers of passes of the scanning nozzle: (a) 1 pass, (b) 2 passes, (c) 3 passes, and (d) 4 passes. Blasting conditions as described in Section 7. 1. 2(a) under ambient temperature conditions.....	138
Figure A 1 EDX analysis of surfaces when machining ABS with and without using LN ₂ at 30° impact angle. White dots are embedded Al ₂ O ₃ particles	147
Figure A 2 EDX analysis of surfaces when machining ABS with and without using LN ₂ at 60° impact angle. White dots are embedded Al ₂ O ₃ particles.....	148
Figure A 3 EDX analysis of surfaces when machining PDMS with and without using LN ₂ at 30° impact angle. White dots are embedded Al ₂ O ₃ particles	148

Figure A 4 EDX analysis of surfaces when machining PDMS with and without using LN ₂ at 60° impact angle. White dots are embedded Al ₂ O ₃ particles.	149
Figure A 5 EDX analysis of surfaces when machining PDMS with and without using LN ₂ at 90° impact angle. White dots are embedded Al ₂ O ₃ particles.	149
Figure A 6 EDX analysis of surfaces when machining PTFE with and without using LN ₂ at 30° impact angle. White dots are embedded Al ₂ O ₃ particles.	150
Figure A 7 EDX analysis of surfaces when machining PTFE with and without using LN ₂ at 60° impact angle. White dots are embedded Al ₂ O ₃ particles.	150
Figure A 8 EDX analysis of surfaces when machining PTFE with and without using LN ₂ at 90° impact angle. White dots are embedded Al ₂ O ₃ particles.	151
Figure B 1 Schematic of the moving heat sink.	152
Figure B 2 Temperature distribution in PDMS predicted by the analytical models at the surface along the direction of motion (<i>X</i> -axis) through the center of the circular cooling jet (<i>Y</i> =0) for $q''=9500 \text{ W/m}^2$, $r=3\text{mm}$, $v=1\text{mm/s}$, $X=0$ represents the center of the moving jet.	155
Figure C 1 Temperature distributions in PDMS at the surface along the direction of motion (<i>X</i> -axis) for different scan speeds and two convective heat transfer coefficient distributions – uniform and Gaussian.	157
Figure D 1 Schematic of overlapping heat sinks: (a) 1mm apart from their centers, (b) 2 mm apart from their centers, (c) 3mm apart from their centers and (d) two consecutive heat sinks. Hatched region shows the area overlapped.	158
Figure D 2 FE predicted temperature distributions in masked PDMS samples at the surface along the direction of motion (<i>X</i> -axis) and through the center of the mask opening (<i>Y</i> =0), for different scan speeds with overlapping heat sinks. The Gaussian convective heat transfer coefficient distribution was used. $X=0$ represents the center of the moving jet.	159
Figure E 1 Air-abrasive mixture hand piece with LN ₂ entraining device.	160
Figure F 1 Measured masked channel center depths as a function of scan speed using CAJM at two abrasive mass flow rates: $M1= 2.83 \text{ g/min}$ and $M2= 6.1 \text{ g/min}$	162

Figure G 1 Particle size distribution of nominally 100 μm particle Al_2O_3 , average diameter=137 μm , Standard deviation = 43.5, Number of measurements = 12965. Measurement by optical particle analyzer (Clemex PS3 Research System, Clemex Technologies Inc., Longueuil, Quebec, Canada).	164
Figure G 2 Particle size distribution of nominally 100 μm particle Al_2O_3 , average diameter=126 μm , Standard deviation = 35, Number of measurements = 9702. Shadowgraphy measurements using a laser shadowgraphy system (LaVision GmbH, Goettingen, Germany).	165
Figure G 3 Aspect ratio distribution of nominally 100 μm Al_2O_3 particle, average aspect ratio=0.55, Standard deviation = 0.14. Number of measurements = 12965. Measurement by optical particle analyzer (Clemex PS3 Research System, Clemex Technologies Inc., Longueuil, Quebec, Canada).	166
Figure G 4 Aspect ratio distribution of nominally 100 μm particle Al_2O_3 , average aspect ratio=0.57 μm , Standard deviation = 0.15, Number of measurements = 9702. Shadowgraphy measurements using a laser Shadowgraphy system (LaVision GmbH, Goettingen, Germany).	167
Figure G 5 Particle size distribution of nominally 150 μm particle Al_2O_3 , average diameter=189 μm , Standard deviation = 44, Number of measurements = 12433. Measurement by optical particle analyzer (Clemex PS3 Research System, Clemex Technologies Inc., Longueuil, Quebec, Canada).	168
Figure G 6 Particle size distribution of nominally 150 μm particle Al_2O_3 , average diameter=162 μm , Standard deviation = 35, Number of measurements = 5211. Shadowgraphy measurements using a laser shadowgraphy system (LaVision GmbH, Goettingen, Germany).	169
Figure G 7 Aspect ratio distribution of 150 μm Al_2O_3 particle, average aspect ratio=0.54, Standard deviation = 0.12. Number of measurements = 12433. Measurement by optical particle analyzer (Clemex PS3 Research System, Clemex Technologies Inc., Longueuil, Quebec, Canada).	170

Figure G 8 Aspect ratio distribution of nominally 150 μm particle Al_2O_3 , average aspect ratio=0.6 μm , Standard deviation = 0.13, Number of measurements = 5211. Shadowgraphy measurements using a laser Shadowgraphy system (LaVision GmbH, Goettingen, Germany).....	171
Figure G 9 Particle size distribution of 136 μm garnet particle, average diameter=158 μm , Standard deviation = 63, Number of measurements = 8068. Measurements using optical particle size analyser (Clemex PS3 Research System, Clemex Technologies Inc., Longueuil, Quebec, Canada).....	172
Figure G 10 Particle size distribution of 103 μm garnet particle, average diameter=114 μm , Standard deviation = 25, Number of measurements = 8686. Measurements using optical particle size analyser (Clemex PS3 Research System, Clemex Technologies Inc., Longueuil, Quebec, Canada).....	173
Figure G 11 Aspect ratio distribution of 136 μm garnet particle, average aspect ratio=0.62 μm , Standard deviation = 0.13, Number of measurements = 25461. Measurements using optical particle size analyser (Clemex PS3 Research System, Clemex Technologies Inc., Longueuil, Quebec, Canada).....	174
Figure G 12 Aspect ratio distribution of 103 μm garnet particle, average aspect ratio=0.65 μm , Standard deviation = 0.12, Number of measurements = 22025. Measurements using optical particle size analyser (Clemex PS3 Research System, Clemex Technologies Inc., Longueuil, Quebec, Canada).....	175
Figure H 1 Qualitative comparison of particles (a) Grittal [®] particles placed on inclined, SEM at 75° incidence to the detector, (b) Al_2O_3 particles placed on inclined, SEM at 75° incidence to the detector and (c) garnet particle observed from side under optical microscope.....	178
Figure I 1 Randomly generated rhombi (equivalent of 103 μm nominal diameter garnet particles).....	181
Figure I 2 Randomly generated rhombi (equivalent of 103 μm nominal diameter garnet particles).....	182

LIST OF APPENDICES

Appendix A	EDX Analysis of Surfaces Machined with and without LN ₂	147
Appendix B	Analytical Solution of a Moving Circular Heat Sink with Uniform Heat Flux Distribution.....	152
Appendix C	Comparison of Temperature Distributions: Heat Sink with Uniform and Gaussian Distributions of h_c	156
Appendix D	CAJM of Masked Channels: Overlapping Moving Heat Sinks.....	158
Appendix E	Device with LN ₂ Entraining Nozzle.....	160
Appendix F	Effect of Particle Dose.....	161
Appendix G	Particle Size, Aspect Ratio and Area Distributions.....	163
Appendix H	Blocky Particle Selection.....	177
Appendix I	Matlab [®] Program for Calculation of Randomly Selecting Area and Aspect Ratio Distributions and Calculating Rhombus Geometries.....	179

NOMENCLATURE

The definition of symbols in alphabetical order:

Symbol	Name	Unit
a	Area	[mm ²]
a_{pl}	Area of a moving circular heat sink	[mm ²]
A	Particle angularity	[°]
A^*	Complementary particle angularity	[°]
C	Constant	[non-dimensional]
c_c	crack length	[μm]
C_p	Specific heat capacity	[Jkg ⁻¹ K ⁻¹]
d	Minor axis of a rhombus	[mm]
D	Major axis of a rhombus	[mm]
E	Elastic modulus	[MPa]
E_1	Elastic modulus of particle	[MPa]
E_2	Elastic modulus of target	[MPa]
F_{ne}^L	Elastic normal force acting on the left side of a particle	[N]
F_{ne}^R	Elastic normal force acting on the right side of a particle	[N]
F_{te}^L	Elastic tangential force acting on the left side of a particle	[N]
F_{te}^R	Elastic tangential force acting on the right side of a particle	[N]
f_i	Impact zone frequency	[s ⁻¹]
$g(\alpha)$	A function describing the impact angle dependence of erosion	[non-dimensional]
H	Hardness	[Pa]
h_c	Convective heat transfer coefficient	[Wm ⁻² K ⁻¹]
h	Particle side length	[mm]
K	Constant	[non-dimensional]
K_t	Time constant	[non-dimensional]
L	Characteristic length	[μm]
k	Velocity exponent	[non-dimensional]
k_2	Constant	[non-dimensional]
m	Mass of particle	[kg, g, mg]
n_1	Parametric exponent	[non-dimensional]
n_2	Parametric exponent	[non-dimensional]
q''	Heat flux	[Wm ⁻²]
p	Pressure	[Nm ⁻²]
p_d	Dynamic hardness	[N]
R	Particle radius	[μm]
r	Crater radius	[μm]

s	Thickness of chip removed	[μm]
T	Temperature	[K]
T_E	Tearing energy	[$\text{kgm}^2\text{s}^{-2}$]
T_i	Initial temperature	[K]
t_i	Average time interval between impacts	[s]
u	Pecelt number	[non-dimensional]
V	Volume	[μm^3]
V_i	Initial velocity	[ms^{-1}]
$V(0)$	Velocity at the center of the jet	[ms^{-1}]
v	Scan speed	[mms^{-1}]
v_j	Abrasive jet centerline average velocity	[ms^{-1}]
v_p	Particle velocity	[ms^{-1}]
W	Mask width	[μm]

Greek symbols

α	Impact angle	[$^\circ$]
α_{td}	Thermal diffusivity	[m^2s^{-1}]
α_t	Coefficient of thermal expansion	[K^{-1}]
β	Focus coefficient	[non-dimensional]
β_i	Biot number	[non-dimensional]
ε	Erosion efficiency	[non-dimensional]
ε_u	Ultimate elongation	[mm]
θ, θ^*	Incident particle orientation	[$^\circ$]
θ_p	Temperature drop at a point	[K]
κ	Thermal conductivity	[$\text{Wm}^{-1}\text{K}^{-1}$]
μ	Tangential force to normal elastic force ratio	[non-dimensional]
μ_{crit}	Critical coefficient of friction	[non-dimensional]
ν	Poisson ratio	[non-dimensional]
ν_1	Poisson ratio of particle	[non-dimensional]
ν_2	Poisson ratio of target	[non-dimensional]
ρ	Density	[kgm^{-3}]
ρ_s	Density of target material	[kgm^{-3}]
ρ_p	Particle density	[kgm^{-3}]
σ_t	Tensile stress	[Pa]
σ_u	Ultimate stress	[Pa]
σ_{y1}	Yield strength	[Pa]
τ	Minimum frequency needed for thermal effects to be significant	[s^{-1}]
ϕ	Particle mass flux	[$\text{kgm}^{-2}\text{s}^{-1}$]
$\phi(0)$	Particle mass flux at the center of the jet	[$\text{kgm}^{-2}\text{s}^{-1}$]
ω	Dimensionless number related to the time to reach steady state	[non-dimensional]

1 Introduction

Abrasive jet micro-machining (AJM) is a micro-machining process in which a jet of small particles is directed through an erosion resistant mask opening so that micro-sized features (i.e. micro-channels, holes, etc.) can be machined for the fabrication of micro-fluidic devices, micro-electro-mechanical-systems (MEMS), and opto-electronic components (Fig. 1.1).

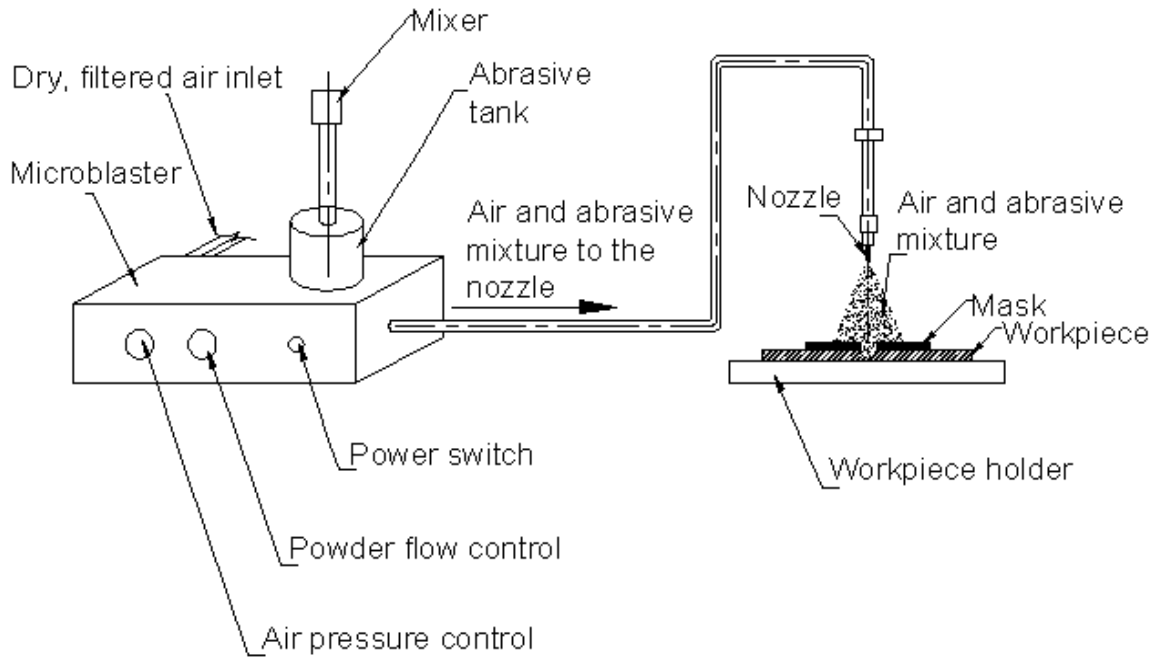


Figure 1.1 Typical AJM process

Figure 1.1 shows a typical AJM setup consisting of a commercial micro-blaster (MB) unit, particle delivery system and a workpiece holder. Filtered, dry air enters through the back of the MB. The pressure regulator allows system pressure adjustment to

the desired value. The regulated air then passes through a mixing chamber and enters the pressure tank where the pressure builds up until it reaches the regulated pressure. The workpiece is held on a computer controlled linear stage (workpiece holder). The computer controlled stage enables movement of the workpiece in the desired direction at the desired velocity. The mask defines the size and shape of machined features.

1.1 Motivation

AJM has several advantages over other machining processes. A particularly attractive feature of AJM is that channels of varying depth can be micro-machined by a simple change in nozzle scan speed. Such three dimensional features are difficult to fabricate, for example, by traditional wet (material is dissolved when immersed in a chemical solution) etching using chemicals. Other advantages of AJM over machining processes such as wet and dry (material is sputtered or dissolved using reactive ions) etching are:

- (i) very low capital cost,
- (ii) very little part vibration or chatter,
- (iii) can machine heat sensitive materials.

This thesis will focus on the AJM of polymers such as acrylonitrile butadiene styrene (ABS), polytetrafluoroethylene (PTFE), polymethylmethacrylate (PMMA) and elastomers such as polydimethylsiloxane (PDMS) which have found applications in a wide variety of micro-devices. For example, polymeric materials are useful in the micro-fluidic industry because they offer a wide range of physical and chemical properties, have the advantages of low cost, good processibility for mass production, and are biocompatible, disposable and/or recyclable [1-4]. Also, polymers have much greater thermal expansion coefficients than silicon and a much larger deflection at the same

average temperature, thus making polymeric thermal actuators in micro-electro-mechanical-systems (MEMS) devices more efficient than their silicon counterparts [5].

Fluoropolymers such as PTFE have become of interest in the micro-fluidic industry because of their excellent chemical resistance. Furthermore, due to their low refractive indices, they are ideal for use in creating integrated waveguides in a large variety of sensors [6]. Fluoropolymer substrates offer significant cost reductions for these applications when compared to ceramic substrates such as glass and Si, (cheaper by \$CAD 0.20 per cm²) [6]. In addition, at room temperature, due to its high wear resistance [7], PTFE can also be used as a masking material for the AJM of brittle materials such as glass and silicon. The use of ABS for manufacturing micro-fluidic devices has been demonstrated by deJong et al. [8] using phase separation micro-moulding techniques.

PDMS offers excellent physical and mechanical properties such as high gas permeability, high compressibility, optical clarity, physical and chemical stability (almost inert) and usability over a wide range of temperatures (-100 °C to 100 °C). Examples of some of the devices which have been manufactured using PDMS include mechanical sensors such as accelerometers, sensors with an integrated ion-sensitive field effect transistor used to measure ion concentrations in solutions, and micro-fluidic chips [9].

PMMA, a thermoplastic polymer, is a very attractive alternative to glass substrates in micro-fluidic applications because it is inexpensive and has excellent

optical, electric and mechanical properties. Since it is a relatively rigid polymer, PMMA can be a suitable replacement for PDMS in micro-fluidic applications where the dimensional variation of the micro-channel due to the native elasticity of PDMS may limit its application [10].

Although AJM can be applied as a cost-effective, environmentally-friendly micro-machining process to polymers, it has been observed that sharp abrasive particles can become embedded [11, 12] possibly affecting the performance of AJM fabricated devices. For example, embedded particles are a potential concern in the performance of AJM fabricated devices such as micro-fluidic chips [13]. Furthermore, they may shield the surface from subsequent impacts resulting in a reduced erosion rate [12, 14]. This thesis is thus motivated by:

- 1) a need to develop an alternative, rapid and cost effective fabrication technique that enhances material removal rate in polymeric materials and enables the micro-machining of elastomeric materials which are of importance in micro-fluidics, MEMS and opto-electronics device manufacturing.
- 2) a need to understand the conditions that lead to particle embedding during the AJM of polymers, and the development of techniques and procedures for the removal of embedded particles.

1.2 Thesis Objectives

The primary objective of the thesis was to investigate AJM methodologies that enhance the material removal rate in polymers and enable the AJM of elastomers for fabrication of micro-devices with minimal particle embedding.

The secondary contributing objectives of the thesis were:

- (i) to develop a cryogenic abrasive jet micro-machining (CAJM) technique to allow the micromachining of elastomeric materials such as PDMS.
- (ii) to investigate the applicability of CAJM to enhance material removal rate in ABS and PTFE.
- (iii) to study the CAJM process parameters that influence the erosion rate and mechanism of material removal, so that the surface evolution of micro-channels and holes in polymeric materials can be accurately modeled.
- (iv) to determine and model the conditions that lead to embedding of angular and spherical particles during AJM.
- (v) to quantify the amount of embedded particles, and develop techniques and procedures to remove them.

1.3 Thesis Organization

The thesis has been organized as follows:

Chapter 2 presents a literature review pertinent to solid particle erosion and the AJM of polymeric materials and parameters that influence their erosion rates.

Chapter 3 describes the equipment used in AJM operations.

In Chapter 4, cryogenic abrasive jet micro-machining (CAJM) was investigated as a novel means of etching features in elastomeric materials such as PDMS, which are very difficult or impossible to machine using AJM at room temperature. The feasibility of the technique to enhance the material removal rate in the AJM of ABS and PTFE was also investigated.

In Chapter 5, thermal analyses of CAJM of PDMS were carried out for the micro-machining of holes and channels. A finite element analysis (FEA) was used to simulate a moving heat sink to investigate the general cooling behaviour during the machining of unmasked and masked channels and to assess the influence of the jet scanning speed. A coupled thermal/structural finite element analysis was used to examine the influence of thermally induced strains on the final room-temperature shape of micro-machined features.

In Chapter 6, the criteria under which embedding of both angular and spherical particles occur at oblique and normal impact angles were established. Conditions under which particle embedding occurred when 103 μm and 136 μm angular garnet particles impacted ABS, PMMA and low density polyethylene (LDPE) at various impact angles were determined using a rigid plastic impact model. The conditions under which 4 mm diameter spherical steel particles embedded in medium density polyethylene (MDPE) at different impact angles were also established.

In Chapter 7 the area covered by embedded aluminum oxide particles following the solid particle erosion of ABS, PTFE, PMDS and PMMA were measured. Several techniques and procedures for the removal of the embedded particles were studied under cryogenic and room temperature conditions.

Chapter 8 summarizes the major findings of the thesis, and presents recommendations for future work.

2 Literature Review

This chapter presents a brief review of the available literature regarding the target materials and impact parameters that influence the solid particle erosion of polymers and elastomers. It also presents a brief review of the literature pertaining to particle embedding during solid particle erosion processes, and recent work on the AJM of polymers.

2.1 Solid Particle Erosion of Polymers and Elastomers

Solid particle erosion is a dynamic process in which material is removed from a target surface as a result of mechanical interaction between impinging particles and the target surface. The material removal mechanisms involved can be due to large scale deformation, fracture, cutting, or a combination of these. Solid particle erosion mechanisms can be classified into two categories, cutting wear and repeated deformation. In brittle erosion processes: deformation wear and fracture are the main mechanisms, while ductile erosion processes exhibit cutting wear [15, 16]. At shallower impact angles, cutting wear (ductile erosion) prevails, and at high impact angles deformation wear (brittle erosion) prevails [17]. Because AJM involves the mechanical removal of target material due to the impact of a jet of solid particles, it can benefit from the vast literature on solid particle erosion phenomena.

2.1.1 Process Parameters Affecting the Solid Particle Erosion of Polymers

Due to the wide variety of physical and mechanical properties of polymers, investigations of solid particle erosion behaviours of polymers usually have focused on a particular type. Because polymeric materials are soft, with the exception of elastomers, the erosion rate (mass loss of the substrate material/mass of erodent particle launched) of polymers is generally two to three orders of magnitude higher than that of metallic materials [18]. For ductile polymers, there may be an initial mass gain, known as an incubation period, due to particle embedding, and maximum erosion occurs at low impact angles. Elastomers behave in this manner, but the weight loss in elastomers is much lower than that found in ductile thermoplastics, and in some cases the material does not reach a steady state erosion rate at a normal impact angle [18]. The solid particle erosion mechanism for elastomers is generally tearing and fatigue while for ductile polymers erosion occurs through cutting and chip formation. For brittle polymers, crack formation is the main erosion mechanism [19].

Solid particle erosion of polymers and elastomers is a complex process which is influenced by many parameters. These parameters can be broadly classified into two categories: process parameters (impact parameters) and material parameters (mechanical, physical and morphological properties). Process parameters such as the impact angle, impact velocity and particle flux are important because they, together with the characteristics of the erodent particles (e.g. size, shape, hardness and mass), affect the

local concentration of erosive energy on the impacted surface. On the other hand, the response of the target material is also a crucial factor that can affect the mechanisms of erosive wear.

2.1.1.1 Particle Shape and Size

Sharp angular particles produce more erosion than spherical particles if all other properties are the same [17, 20]. The material removal rate of ductile materials varies with particle size. The erosion rate increases as the particle size increases up to a certain point, after which the erosion rate remains constant with increasing particle size [20].

2.1.1.2 Particle Hardness

It has been reported that the hardness of impacting particles affects the erosion rate of polymers. Generally hard particles remove more target material than soft particles, but it is impossible to isolate hardness completely from other features of the particle (e.g., shape) [18]. It has been noted that even if a particle is hard but relatively blunt it is unlikely to cause severe damage to the target, especially in ductile targets [18].

2.1.1.3 Erodent Velocity

Particle velocity is one of the most important parameters that influence the solid particle erosion of polymers. When the incoming particles are perpendicular to the target surface (normal impact) the erosion rate is usually assumed to be directly proportional to a power of the particle velocity (v_p) according to [21]:

$$E_r \propto v_p^k \quad (2.1)$$

where k is found experimentally to usually be between 2 and 3 for polymeric materials eroding in ductile manner, and between 3 and 5 for those polymers and polymer composites eroding in brittle manner [22, 23]. The velocity exponent (k) depends on process conditions such as particle velocity and size, and mechanical properties of the target and the erodent particles [24].

2.1.1.4 Particle Flux

Theoretically, the erosion rate of a material should be independent of the particle flux (mass of particles striking a target per unit area per unit time) striking a target since it is assumed that all the particles hit the target with the same velocity and impact angle [18]. But after a certain limit, increasing the particle flux can result in a decreased erosion rate [25, 26] due to collisions between incoming and rebounding particles [25, 26].

2.1.1.5 Impact Angle

Many researchers have reported that the target material removal rate depends on impact angle [27, 28]. In general, for ductile materials, the peak material removal occurs at oblique impact angles, while for brittle materials, it occurs at, or close to, normal incidence (90°). In the erosion of brittle materials, the material is removed mainly due to crack formation and chipping mechanisms [15, 16] that are most evident at perpendicular incidence where the energy transfer to the substrate through the normal velocity component is maximum [21, 29]. At oblique impact angles, the target material is cut and ploughed by sharp edged eroding particles [15] so that mechanisms associated with the tangential component of incident velocity contribute to erosion. Most polymers erode in a ductile manner, exhibiting a maximum erosion rate at a shallow impact angles where the cutting action is most effective [15, 16].

2.1.2 Target Material Parameters Affecting the Solid Particle Erosion of Polymers

2.1.2.1 Mechanical Properties

Material properties strongly affect the erosive wear of polymeric materials, and they have thus been studied extensively [e.g. 30-32]. Many researchers have focused on investigating the relationship between the bulk mechanical properties and the resulting erosive wear [30, 31, 33-36], even though the thermal, mechanical and chemical

degradations occurring during solid particle erosion can change the properties of the eroded layers from those of the bulk material [37]. The following mechanical properties are commonly thought to influence the erosive wear of polymeric materials [18]:

- hardness,
- tensile strength,
- Young's modulus ,
- yield stress,
- ultimate strength,
- elongation,
- tearing energy (for elastomers).

Erosive wear decreases with increasing target hardness when the erosion process takes place at oblique angles. On the other hand, elastomeric materials show generally better erosion resistance at lower values of hardness. Several researchers have attempted to incorporate material parameters and introduce empirical relationships in order to predict erosive wear [19, 36-39]. Sundararajan et al. [40] have introduced a parameter known as the *erosion efficiency* (ε) which they claim is capable of identifying the dominant micro-mechanism leading to erosive wear for a wide range of materials including coatings, metals and ceramics. This parameter is given as:

$$\varepsilon = \frac{2E_r H}{\rho v^2} \quad (2.2)$$

where E_r is the erosion rate, H is the target hardness, ρ and v are the density and velocity

of the erodent material, respectively. As can be seen from Eq. (2.2), hardness is the only target material parameter included in the analysis.

According to the work of Ratner et al., [41], the wear rate of rubber has been found to be inversely proportional to the ultimate tensile stress and elongation:

$$E_r \propto \frac{1}{\sigma_u \varepsilon_u} \quad (2.3)$$

where σ_u and ε_u are the ultimate tensile stress and elongation, respectively. The term $\sigma_u \varepsilon_u$ gives the approximate area under the stress-strain curve to fracture, consequently yielding an estimate of the energy to fracture.

Arnold and Hutchings [42] reported that the wear mechanism in the erosion of elastomers involves the propagation of fatigue cracks due to repeated indentation. They estimated the fatigue crack growth rate due to the surface tensile stress by assuming that the stress acts on the edge of the crack, growing vertically into the surface, from which the tearing energy (T_E) was estimated as follows [42]:

$$T_E = \frac{K c_c \sigma_t^2}{E} \quad (2.4)$$

where E is the tensile elastic modulus, σ_t is the tensile stress, c_c is the instantaneous crack length and K is a parameter which is a function of strain.

During solid particle erosion, the incident particle kinetic energy is transferred into plastic deformation of the target and rebound kinetic energy of the particle [43]. The energy transferred to the target material depends on the mechanical properties of the target and the erodent, such as Young's modulus and hardness. For example, the ratio of the particle rebound velocity to the incident velocity (the coefficient of restitution) was suggested as a useful parameter used to qualitatively assess the target damage [43]. If the coefficient of restitution is high, the elastic deformation of the target is high, which means the target material experiences less damage [43].

2.1.2.2 Morphological Properties

According to Friedrich [44], the molecular and morphological structures of semicrystalline polymers have a tremendous effect on the erosion resistance. For example, the less crystalline, highly atacticⁱ polypropylene (semicrystalline, 20% atactic) exhibited the highest wear resistance. Polypropylene (semicrystalline, 5% atactic), on the other hand, with a higher crystallinity and lower atactic content, eroded much faster, especially when the morphology was coarse spheruliticⁱⁱ.

ⁱ Polymers with molecules in which substituent groups of atoms are arranged at random above and below the backbone chain of atoms.

ⁱⁱ Spherulites are spherical semi-crystalline regions inside non-branched linear polymers.

Barkoula et al. [18] investigated the effect of crystallinity on the erosive wear of different grades of polyethylene (PE) and found that an increase in crystallinity led to a steep increase in the erosion rate and the effect of crystallinity was more pronounced at low impact angles. As the impact angle proceeded to 90° the crystallinity had less influence on the erosion rate [18].

2.1.2.3 Thermal Properties

Polymers have long chain molecules that are entangled with one another. These chains are able to slide over one another at moderate temperatures; however, as the temperature is decreased to the glass transition temperature and below, most polymers stiffen and behave more like glasses. The tensile strength, compressive strength and Young's modulus of most polymers increase or remain constant as the temperature is decreased, while the elongation to failure decreases to extremely low values at cryogenic temperatures. As a result, the high strain mechanical response of a polymeric material is strongly affected by both temperature and strain rate and, depending upon these parameters, may range from ductile yielding to brittle fracture [45-47]. For example, Hiltner and Baer [48] found that contact with liquid nitrogen significantly altered the tensile behaviour of polycarbonate and poly(ethylene terephthalate) between 45 K and 80 K. Specimens tested under these conditions were heavily crazed, and the abrupt yielding was thought to be a consequence of craze nucleation and growth.

To summarize, the solid particle erosion of polymers is a complex process in which the material removal mechanism and rate are controlled by many variables such as impact angle, particle flux, size and type of particles, temperature, and target mechanical and morphological properties.

2.2 Abrasive Jet Micro-machining of Polymers

Traditional micro-fabrication technologies have been adapted from the electronics industry, which use brittle materials such as ceramics and glass. However, these materials and their associated traditional fabrication methods (e.g. wet chemical etching) are relatively expensive [49-51]. As mentioned in Section 1.1, AJM can be advantageously applied as a cost-effective and rapid alternative micro-machining technology for polymers. For example, based on the data provided in Ref. [12], the etch rate of PMMA using AJM at room temperature was on the order of 185 $\mu\text{m}/\text{min}$. Using deep reactive ion etching, for example, Zhang et al. [52], reported the etch rate of PMMA to be 0.40 $\mu\text{m}/\text{min}$, when using a maximum power of 60 W, beyond which the material became distorted. Using an ArF excimer laser having a 193 nm wavelength and 100 mJ max power, Hsieh et al. [53] found a PMMA etch rate of 10 $\mu\text{m}/\text{min}$.

These advantages motivated previous studies of the erosion mechanisms associated with the AJM of features such as channels and holes in acrylic polymers such as polymethylmethacrylate (PMMA) [11, 12]. PMMA was found to have a typically

ductile erosion response, characterized by a maximum erosion rate at 25° impact angle [11]. The channels machined in PMMA exhibited much steeper sidewalls and flatter central sections than those reported for the abrasive jet micro-machining of glass. Steeper sidewalls were obtained because the maximum erosion rate for PMMA occurred at a relatively shallow angle, thus accelerating the surface evolution of the sloped sidewalls [11].

As mentioned in Section 1.1, in addition to PMMA, there is great interest in the use of elastomeric materials such as PDMS and polymers such as PTFE for fabrication of micro-devices; which are either impossible to micro-machine or have very low material removal rate under ambient temperature conditions. Despite the fact that it is well known that the mechanical properties of many polymers change significantly at low temperatures [54-57], the use of a cryogenically assisted abrasive jet machining system for polymers has never been investigated. Cryogenic machining using cutting tools has been used for metals [57, 58], and Muju and Pathak [59] reported an increased material removal rate in the abrasive jet machining of glass that was cooled using liquid nitrogen. Cryogenic blasting for coating removal has also been studied by a number of researchers. For example, Weston et al. [60], used dry ice (CO₂) blasting to strip paint, while Spur et al. [61] examined the possibility of blasting dry ice to remove silicone seals from an engine. Finally, Brewis et al. [62] have examined the possibility of using cryoblasting using solid CO₂ as a pre-treatment for aluminum.

Chapters 4 and 5 of this thesis investigated cryogenic abrasive jet micromachining (CAJM) as a novel means of etching features in elastomeric materials such as PDMS, which are very difficult or impossible to machine using AJM under ambient temperature conditions. The feasibility of the technique to enhance the material removal rate in the AJM of ABS and PTFE was also investigated.

2.3 Particle Embedding during Solid Particle Erosion

In most cases, particle embedding has been reported as an unwanted consequence of solid particle erosion. For example, Day et al. [63] reported that grit contamination of Hastelloy[®] X (nickel-chromium-iron-molybdenum alloy) sheet by fused alumina increased with increasing impact angle, grit size, blasting pressure and number of blasting passes. Particle embedding has been reported to reduce the effectiveness of grit blasting of metal surfaces because of decreased adhesion of plasma and ceramic coatings [63, 64]. Rajahram et al. [65] reported that fragmented silica sand erodent particles were embedded into the UNS S31603 stainless steel, which caused formation of stress concentrated regions thus contributing to crack initiation. Brown and Edington launched spherical glass beads of 70 μm nominal diameter at 133 m/s speed and observed that fragments were embedded in single crystal copper target [66]. They reported that local heating effects were maximized because of the low thermal conductivity of the embedded erodent glass fragments [66, 67].

Papini and Spelt [68, 69] developed a model to analyze the erosion of targets of arbitrary dynamic hardness and friction coefficient due to the impact of individual angular particles with the purpose of predicting crater size, shape, and rebound parameters as a function of incident velocity, angle, particle orientation, and shape. They found that particles with high angularity are generally more likely to embed at high angles of attack regardless of their orientation for both the constant friction and frictionless cases.

A number of studies have reported that particle embedding reduced the erosion rate of the target material. For example, Zu et al. [70] attributed a decrease in the erosion rate of an aluminum alloy to embedded silica particles. Kim [71] reported that the erosion rate of high purity reaction-bonded silicon nitride discs decreased due to the embedding of 100 μm silicon carbide particles blasted at 900 °C.

The erosion rate of PMMA machined with 25 μm Al_2O_3 particles was reported to depend on the jet scanning direction when the nozzle was inclined with respect to the target surface at 55° [12]. EDX (energy dispersive x-ray) mapping of the forward and backward micro-machined channels showed that there was more particle embedding in case of the forward machining than backward, which decreased the material removal rate at a 55° impact angle. The difference was explained in terms of differences in the energy flux distribution at the leading and trailing edges of the blast pattern which affected net

particle embedding and hence the resistance of the material to erosion in subsequent passes [12].

In machining operations particle embedding may reduce the efficiency of chip removal. For example, Zhou and Bahadur [72] reported that embedded silicon carbide particles may have prevented the removal of a chip from a Ti-6Al-4V substrate by blocking the cutting action of an impacting particle.

Walley and Field [33] have reported embedding of fragmented sand particles of 50 μm maximum size into polyethylene targets during the initial incubation period of erosion testing. It was not clear if the original sand particles with sizes from 300 μm - 600 μm , launched at 36 ± 6 m/s, broke on initial impact or when struck by subsequent impacts. Friedrich [44] launched 500 μm steel balls at 57 m/s and observed that steel particles smaller in size than the launched ones were embedded in polyethylene targets at -35 °C and in polybutene-1 at room temperature. He reasoned that the erodent material must have contained broken irregular-shaped steel particles besides the steel balls because it was unlikely that the steel balls fragmented upon impact. Harris and Beevers [73] reported that the use of smaller alumina particles increased embedding on mild steel and aluminum in contrast to the results of Day et al. [63] who reported that an increase in the size of particles increased grit contamination.

The quantification of embedded particles can be complicated by the difficulty in distinguishing small embedded particles from the surrounding rough target surface. In most cases, SEM in conjunction with EDX has been found to be useful in quantifying the amount of embedded particles. Momber et al. [64] reviewed problems associated with grit contamination and the resulting adhesion problems on hot-rolled low-carbon steel containing different alloying elements. They used scanning electron microscopy (SEM) and image analysis to quantify embedding, finding that embedded 165 μm aluminum oxide particles covered approximately 8% of the surface of a steel alloy after 300 s of blasting.

Lathabai et al. [14] using SEM in backscattered mode and EDX analysis have shown the existence of embedded particles in a 500 μm thick flame sprayed Nylon 11 coating after blasting with 10 μm SiO_2 particles at 3.5 m/s, indicating that particle embedding can occur even at relatively lower speeds with relatively smaller particles. They also suggested that the embedded particles may contribute to a shielding effect. Sari [74] also used EDX analysis to observe the embedment of fractured aluminum oxide particles in a polyphenylene sulfide (PPS) composite following impact of angular Al_2O_3 particles (150 μm -212 μm) at 1.57 m/s.

Amada et al. [75] used an electron probe micro-analyzer (EPMA) and image analysis to determine that up to 10% of the surface area of grit-blasted steel was covered by Al_2O_3 and ZrO_2 . Gröbl et al. [76] used SEM and X-ray microanalysis techniques to

count embedded alumina particles on titanium-aluminum alloy hip implants after grit blasting, measuring 154 per mm² in the size range 15-95 μm.

Several methods of removal of embedded particles have been investigated. Negri et al. [77] conducted experiments in a flow chamber to investigate the effects of chemical solutions on the detachment of 0.3 μm and 3 μm alumina particles embedded in GaAs wafers after mechanical polishing. They found that an ammonia solution gave the best particle removal rate (80%). Toscano and Ahmadi [78] used CO₂ pellets to remove embedded silica particles in silicon wafer and they reported that the effectiveness of the surface cleaning increased as the nozzle-substrate angle decreased; i.e. as the tangential component of the impact velocity increased.

Chapter 6 of this thesis examines the conditions under which particle embedding of angular and spherical particles occur when impacting ABS, PMMA and LDPE at various impact angles and compares the results with published data. In chapter 7, various techniques for particle removal were also investigated, as was the minimization of embedding by the use of cryogenic AJM.

2.4 Chapter Summary

A review of the literature suggests that there is increasing interest in the use of polymeric materials for fabrication of micro-devices and that the properties of polymers

significantly change as the temperature is decreased. It also indicates the occurrence of particle embedding during solid particle erosion and its unwanted consequence which could affect the performance of AJM machined devices such as micro-fluidic chips. These factors motivated the studies in the present thesis.

3 Experimental Apparatus Used for AJM and Solid Particle Erosion Experiments

This chapter gives a general overview of the experimental apparatus used to investigate the AJM and solid particle erosion of polymers at room temperature. It also describes the measurement equipment used to characterize the eroded profiles and erodent particles. Additional details of the cryogenic abrasive jet micro-machining setup and the details of the experimental procedures are described in later chapters.

3.1 Experimental Setup

Figure 3.1 shows the AJM setup used in the present work, consisting of a commercial micro-blaster unit (MB 1005 Microblaster, Comco, Inc., Burbank, CA, USA), into which a mixing device was incorporated to the micro-blaster tank [79] prevent particle bed compaction (Fig. 3.1). The regulated dry, filtered air passes through the mixing chamber and enters the pressure tank where it builds up until it reaches the regulated pressure (Fig. 3.2).

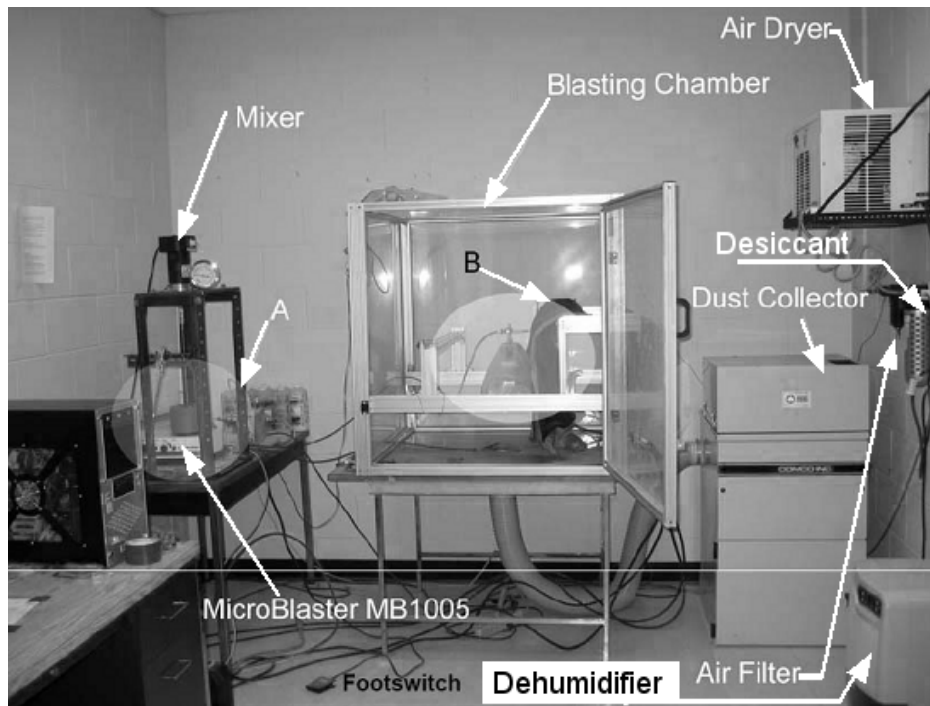


Figure 3.1 Typical abrasive jet micro-machining experimental set-up.

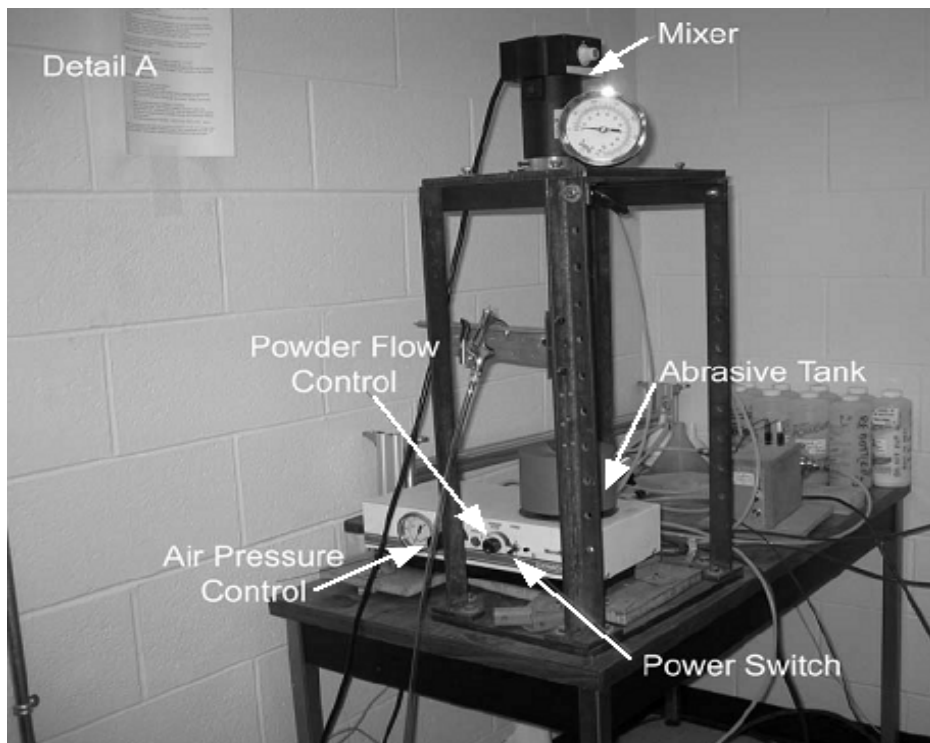


Figure 3.2 Detail A: Experimental apparatus, MB1005 and its parts.

The apparatus was used to determine erosion rates, machine micro-holes and micro-channels, and carry out solid particle erosion experiments, as explained in more detail in Chapters 4, 5, 6 and 7. Fig. 3.3 shows a typical setup used for the micro-machining of a masked channel using a masking device which is held on a computer controlled linear stage (Fig. 3.3) having $0.5\ \mu\text{m}$ accuracy. Air and abrasive mixture flow through the nozzle is achieved by stepping on the footswitch (Fig. 3.1). The dust collector provides appropriate airflow through the blasting chamber to extract the spent abrasive (Fig. 3.1). The humidity of the work-space is regulated with the dehumidifier (Fig. 3.1).

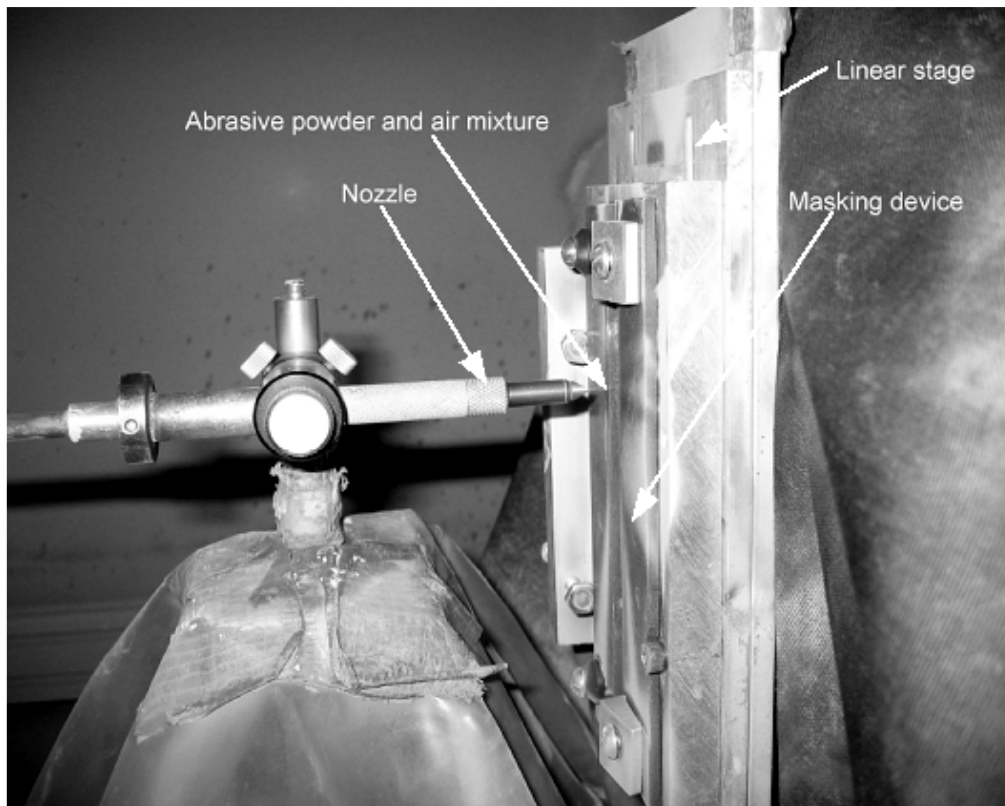


Figure 3.3 Detail B: Experimental apparatus, computer controlled linear stage.

3.2 Masks

Two 1 mm thick tool steel plates having sharply machined edges which can be clamped a fixed distance apart (depending on the desired channel width) onto the target were designed to act as masks for the machining of masked channels (Fig. 3.4). The mask for the AJM of holes consisted of a 1 mm thick tool steel plate into which round $800\pm 60\ \mu\text{m}$ diameter holes were drilled (Fig. 3.5).

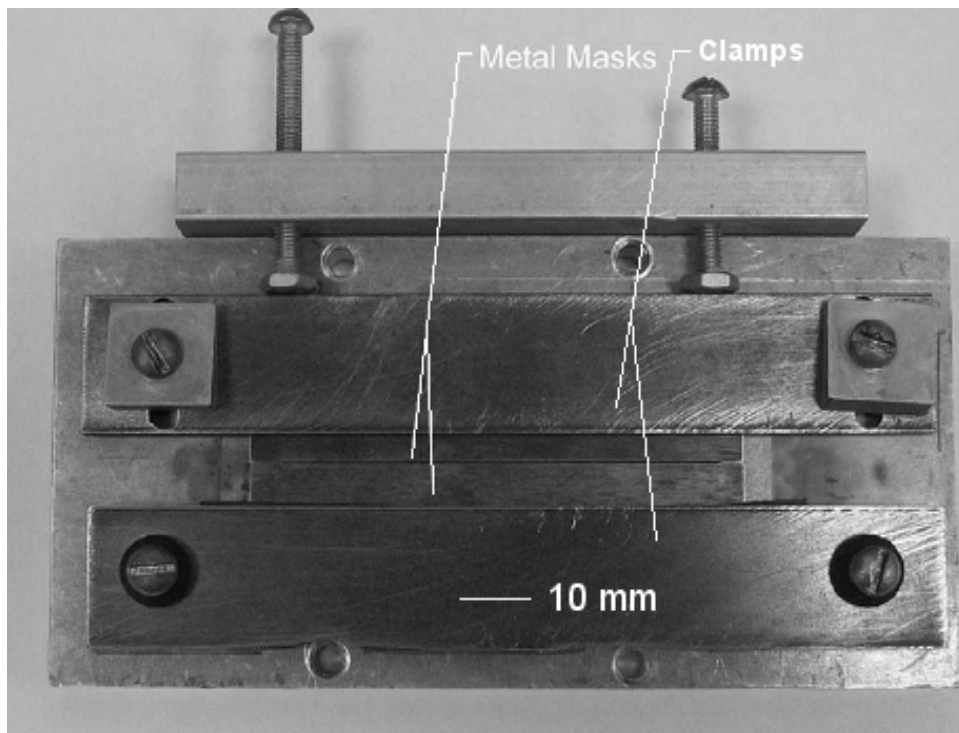


Figure 3.4 Masking device for channel machining.

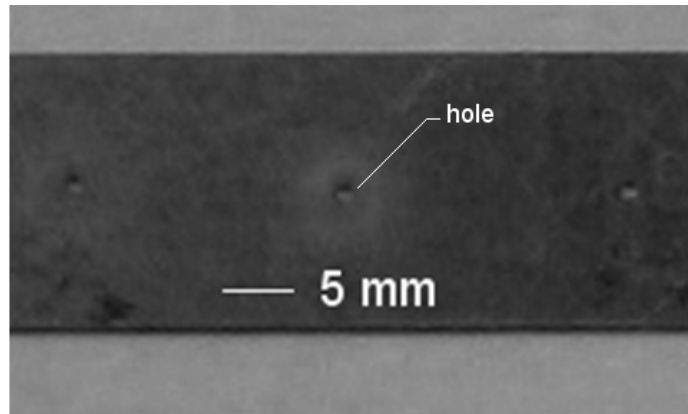


Figure 3.5 Metal masks for fabricating micro-holes.

3.3 Nozzles

Different kinds of nozzles were used depending on the type of experiment performed. A round nozzle having an inside diameter of $760\ \mu\text{m}$ (Fig. 3.6a) was used for erosion rate measurements and the machining of unmasked channels (Chapter 4, 5 and 7). A round nozzle with an inside diameter of 1.5 mm (Fig. 3.6b) was used to obtain discrete, non-overlapping craters (Chapter 6). A rectangular slot nozzle (0.3 mm x 3.8 mm) was used (Fig. 3.6c) for micro-machining masked channels and holes (Chapter 4 and 5).

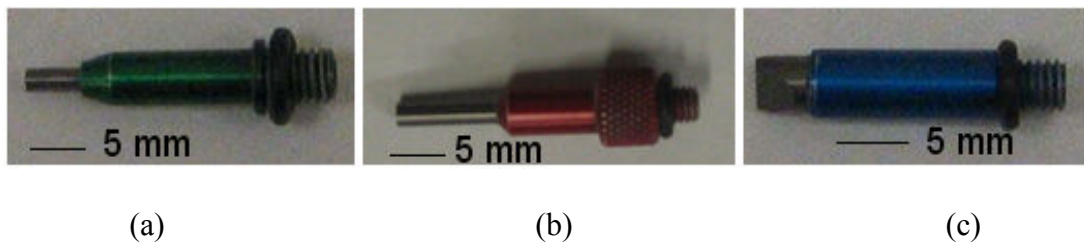


Figure 3.6 Nozzles: (a) a round nozzle ($760\ \mu\text{m}$ inside diameter) used for erosion rate measurements and machining unmasked channels, (b) round nozzle (1.5mm inside diameter) used for particle impact experiments and (c) Rectangular (0.3 mm x 3.8 mm) slot nozzle used for machining masked channels and holes.

3.4 Particle and Machined Feature Characterization

Measurements of the particle velocity, size, area and aspect ratio distributions were performed using a laser shadowgraphy system (LaVision GmbH, Goettingen, Germany). High resolution images (Chapter 6) of the shadows of particles were obtained to allow for simultaneous measurement of particle size, velocity and aspect ratios (defined as the particle length to width ratio) with image resolution 4K (4096×2160). The laser shadowgraphy system (Fig. 3.7) consisted of a double pulse laser (Nd YAG: neodymium: yttrium aluminum garnet) with high efficiency diffuser (Lavisision GmbH, Goettingen, Germany) which was placed opposite to a high speed dual-frame CCD camera (Imager Pro PlusX, Lavisision GmbH, Goettingen, Germany) with a high magnification zoom lens (Navitar zoom 12x, Navitar Inc., Rochester, New York, USA). The abrasive jet was incident in a plane parallel to the camera lens (Fig. 3.7). The depth of focus defined the plane of particles on which the measurement was made. Computer software (Davis software, Lavisision GmbH, Goettingen, Germany) was used to process and analyze the images and evaluate the sizes and velocities of the individual particles.

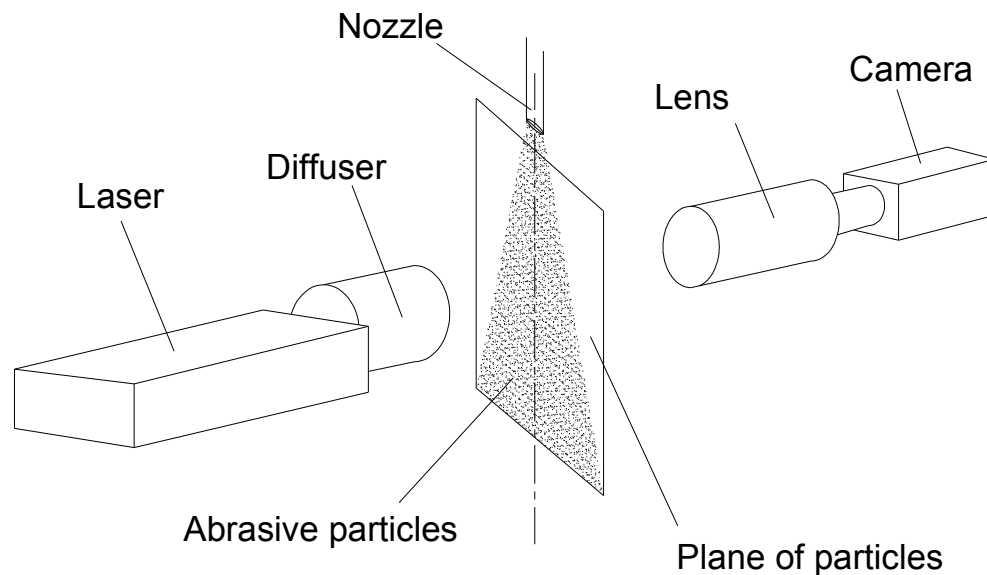


Figure 3.7 Schematic of the laser shadowgraphy experimental setup for measurement of particle size and velocity distribution.

An optical particle size analyser (Clemex PS3 Research System, Clemex Technologies Inc., Longueuil, Quebec, Canada) was also used to obtain particle size distributions (Chapter 4, 5, 6 and 7). The system enables an automated image analysis combining an automated microscope and an imaging workstation with particle characterization software (Fig. 3.8). Using the Clemex computer software, which implements filters allowing for automatic corrections due to, for example, particle agglomeration, the particle circular diameter, aspect ratio and standard deviation were determined. The system was used with a 50X magnification.

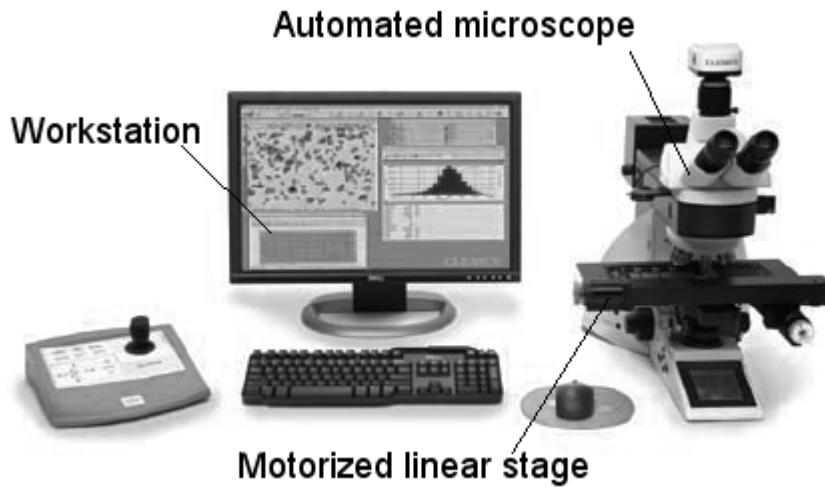


Figure 3.8 Clemex PS3 particle size analyser.

Profiles of the machined features (Chapter 4, 5) were measured using an optical profilometer (NANOVEA ST400 Micro Photonics Inc., Irvine, CA, USA). A 1.2 mm modular optical pen with 25 nm and 1.55 μm depth and lateral resolution respectively, was used to obtain cross-sectional profiles of machined channels. Nanovea 3D acquisition software (NANOVEA ST400 Micro Photonics Inc., Irvine, CA, USA) was used with the profilometer (Fig. 3.9) in order to measure the size and shape of the eroded profiles. Professional 3D software (NANOVEA ST400 Micro Photonics Inc., Irvine, CA, USA), which provided a set of surface analysis tools which were used to further process the measured profiles to, for example, obtain 3D images (Section 4.3.2).

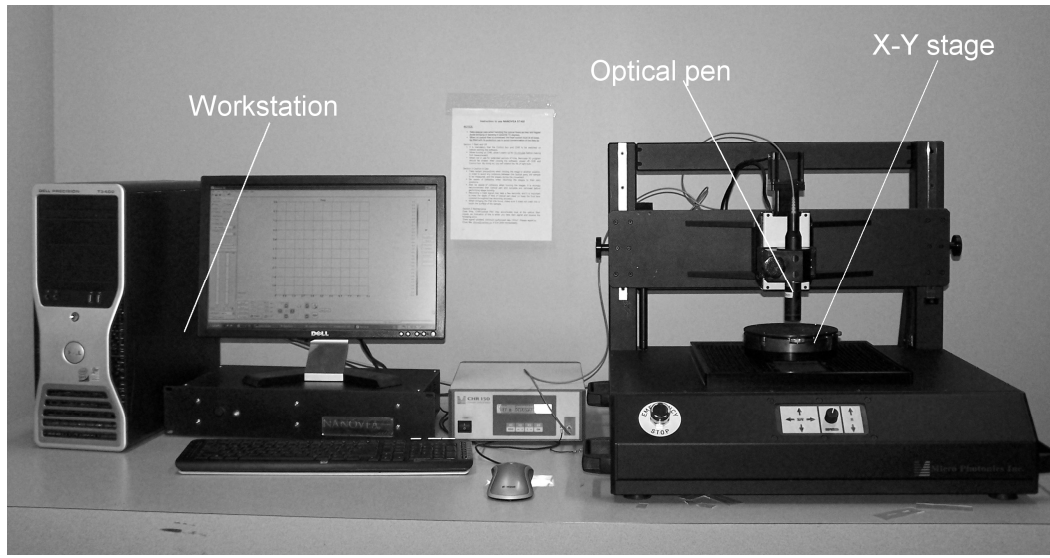


Figure 3.9 NANOVEA ST400 optical profilometer.

A mechanical profilometer (Form Talysurf 50, Taylor Hobson, Leicester, UK) was used to observe and study the topology of micro-machined parts and obtain surface roughness. A stylus arm having 16 nm resolution was used to obtain the surface roughness of the machined profiles (Chapter 4).

A Scanning Electron Microscope-SEM (JEOL JSM-630LV, Japan) in conjunction with EDX was used to quantify the amount of embedded particles (Chapter 4, 7). Also, SEM was used to qualitatively characterize the shape of different particles (Chapter 6, Appendix H)

4 Cryogenically Assisted Abrasive Jet Micro-machining (CAJM)

This chapter describes the development of an apparatus that can be used to enhance the material removal rate in ABS and PTFE and enables machining of PDMS by cooling them to cryogenic temperatures using a stream of liquid nitrogen (LN_2). Erosion rate measurements on the two polymeric materials (ABS and PTFE) and an elastomer (PDMS) with and without the use of LN_2 are compared along with the profiles of micro-machined channels and holes. Much of the material in this chapter has been published by the present author in [80, 81].

4.1 Cryogenic Abrasive Jet Micro-machining Apparatus

A novel cryogenic abrasive jet micro-machining (CAJM) apparatus (Fig. 4.1) was developed that enables etching features in elastomeric materials such as PDMS, which are very difficult or impossible to machine using AJM under ambient temperature conditions. A separate system, shown in Fig. 4.2, provides a liquid nitrogen (LN_2) stream that is injected into the abrasive jet. In this system, an open cryogenic container was placed in the pressure vessel with a tube extending down into the LN_2 .

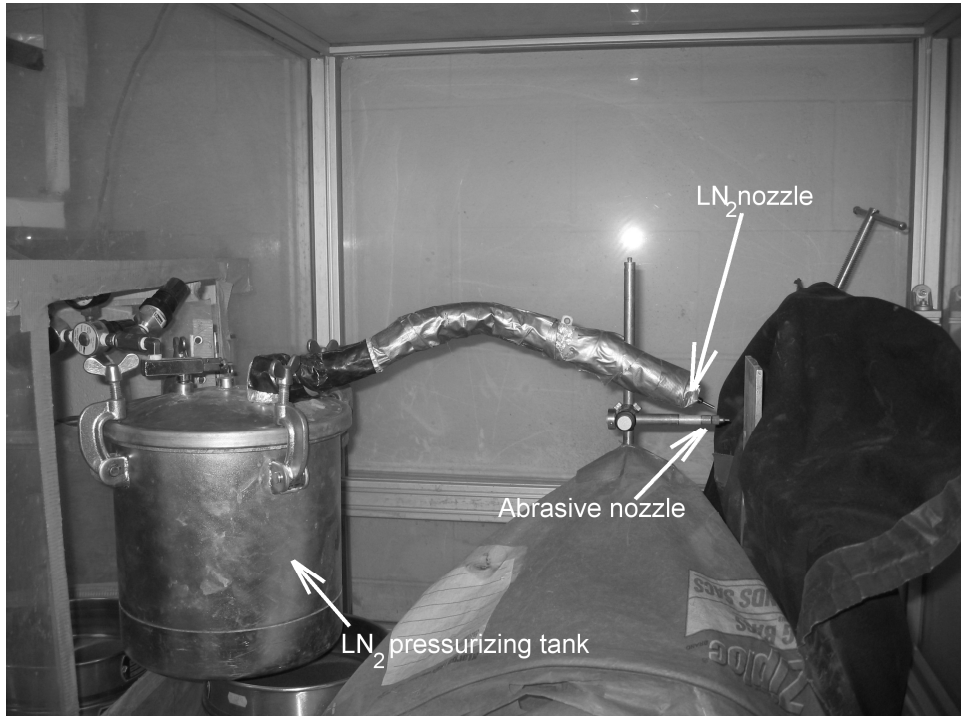


Figure 4.1 Cryogenic abrasive jet micro-machining setup.

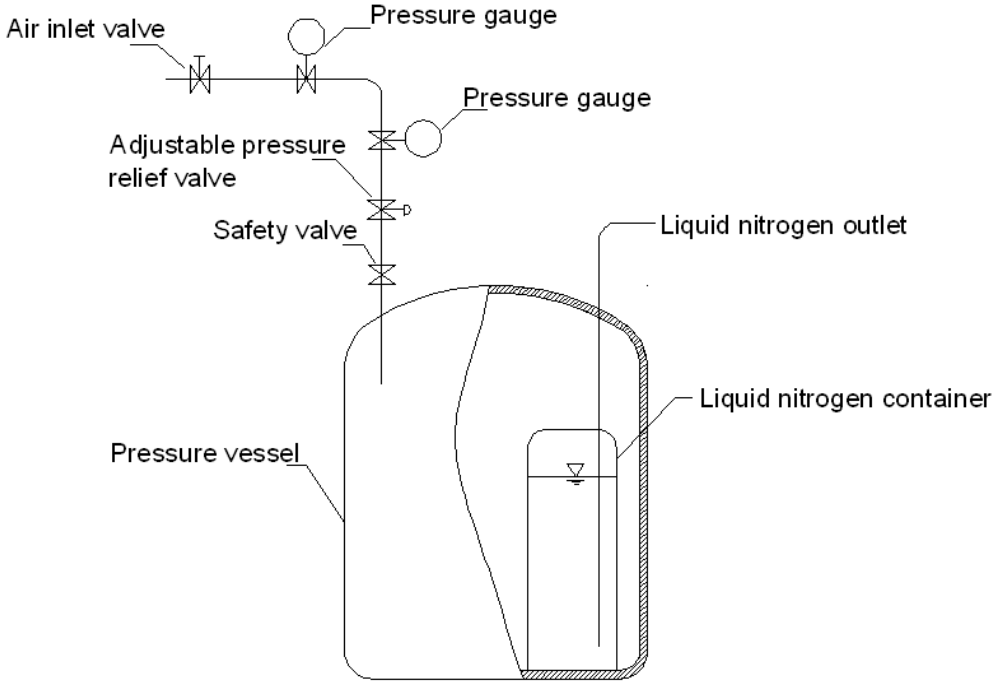


Figure 4.2 Schematic of the LN2 pressurizing and dispensing equipment.

After the pressure vessel was closed, pressurized air at 170 kPa caused the LN₂ to flow through the tube into the abrasive jet through a 1.2 mm diameter nozzle. The LN₂ nozzle was positioned beside the abrasive jet nozzle with its centerline inclined approximately 10° from that of the abrasive jet (Fig. 4.3). The inclination of the nozzle at 10° minimized the deflection of the abrasive particles while still providing an adequate mixing of the LN₂ with the abrasive jet.

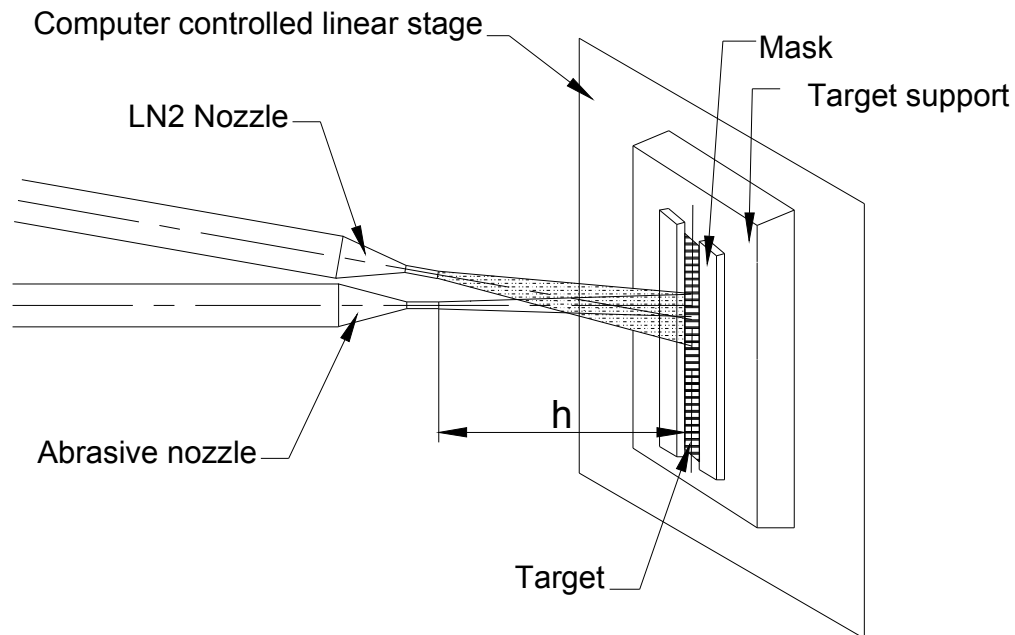


Figure 4.3 Schematic of LN₂ injection to the abrasive jet during CAJM process.

The temperature within the LN₂ cooled jet at the surface of the target was measured using a 80 μm diameter K-type thermocouple, and found to be -150 °C, which is above the boiling point of LN₂ at atmospheric pressure (-196 °C), but below the lowest

glass transition temperature of the three polymers (-120 °C for PDMS) that were considered in this study.

4.2 Experiments

All experiments were conducted using a commercial micro-blaster described in Section 3.1 with granular aluminum oxide powder (Fig. 4.4) of 25 μm (Comco Inc., USA) nominal diameter (hardness of 20 GPa [27]).

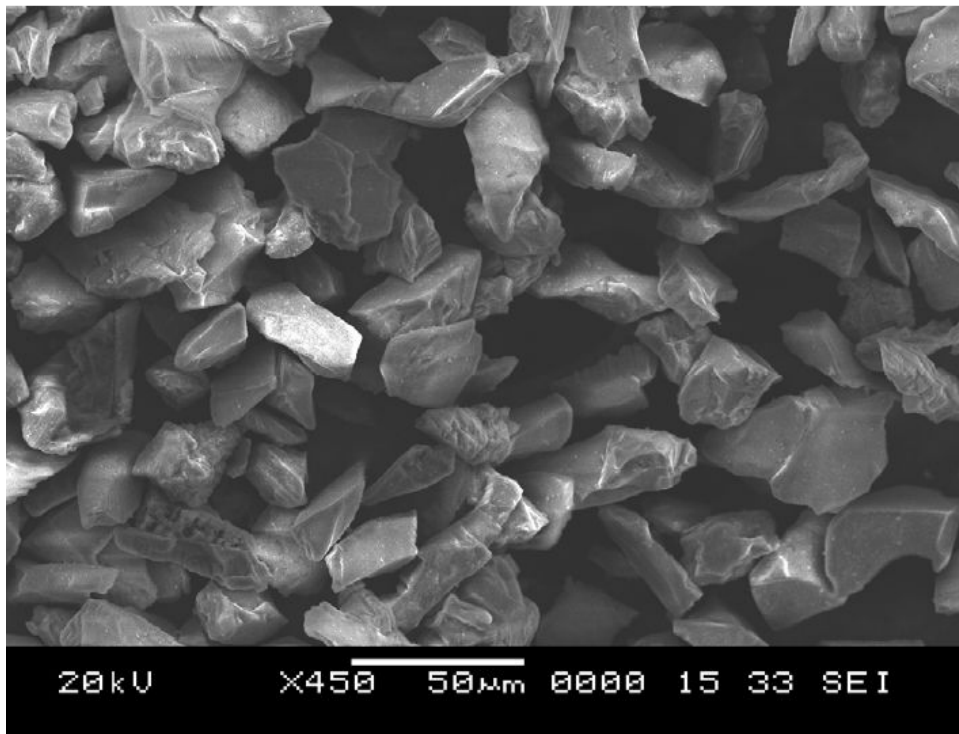


Figure 4.4 Al_2O_3 particles used in the experiments.

Using the optical particle size analyser described in Section 3.4, the powder was found to have a log-normal size distribution with a mean diameter of 31.5 μm and a

standard deviation of 7 μm . The stand-off distance (h) (Fig. 4.3) between the abrasive nozzle tip and the target was held constant at 20 mm, perpendicular to the target in all cases. The chosen pressure and standoff distance are consistent with typical AJM conditions used by a number of investigators [26, 82-85], and have been optimized for a number of factors. For example, measurements have shown that use of a shorter standoff distance results in a lower particle velocity, since the particles are still accelerating up to 20 mm from the nozzle [86]. Moreover, a shorter standoff distance and a higher pressure increase the particle and air mass flux to the surface. Shorter standoff distance can also result in a reduced erosion rate due to increased collisions between incident and rebounding particles [87-91].

The nozzle was held stationary in all cases, and the target sample was mounted on a computer controlled linear stage that was held stationary when measuring erosion rates, and moved at a constant speed of either 1 mm/s or 0.5 mm/s when machining masked channels and holes, respectively.

4.2.1 Erosion Rate Measurements

In order to gain an understanding of the changes in solid particle erosion brought about by the temperature changes, the erosion rates (mass of target material removed per unit mass of abrasive blasted) of PDMS, ABS and PTFE were measured both at room temperature and with the cryogenic cooling. The measurements were made with a round

nozzle having inside diameter 760 μm as described in Section 3.1 with the centerline of the jet axis oriented at angles of 30°, 60°, and 90° ($\pm 1^\circ$) to the target surface. The aluminum oxide powder (Fig. 4.4) was blasted at an average flow rate of 2.83 g/min (standard deviation of 0.12 g/min). The flow rate was measured prior to each experiment by blasting the powder into a sealed container with a particulate filter for 2 min prior to each machining experiment. At room temperature, the average velocity of the particles across the jet for this nozzle was 100-110 m/s, and the maximum velocity was 160 m/s [79], as measured using a phase doppler particle analyser [92].

A solenoid-actuated shutter with an electronic timer was placed in front of the nozzle to fix the blasting duration for a given sample at 40 s. Prior to blasting, the samples were first weighed using an electronic balance with 0.1 mg accuracy and after blasting, each target sample was cleaned and reweighed to determine the mass loss. The average abrasive flow rate was multiplied by the exposure time to obtain the mass of particles blasted over the 40 s duration. The non-dimensional erosion rates were then calculated as the mass of material removed per unit mass of particles launched.

To estimate the repeatability of the measurements within a particular experiment as well as between experiments, the erosion rate measurements were repeated on the ABS samples three times, each time using three measurements at each impact angle. The standard error, both within and between sets of experiments, was found to be approximately 10% of the average value for ABS machined at 90°, 60° and 30°.

4.2.2 Masked Micro-channels and Holes

Masked channels and holes were machined using masks described in Section 3.2 in cast ultraviolet cured PDMS (resin supplied by Ellsworth Adhesives, Burlington, ON, Canada), engineering grade high impact ABS (Warehouse Plastics, Scarborough, ON, Canada) and Teflon[®] PTFE (McMaster Carr, USA). The masks were clamped approximately 300 μm apart onto the target. A rectangular slot nozzle described in Section 3.3 was used to micro-machine the channels and holes with 25 μm aluminum oxide powder at a mass flow rate of 5.21 g/min (standard deviation 0.11 g/min). During the machining of channels the specimen was moved at 1 mm/s over an 8 mm length with the wider nozzle dimension perpendicular to the channel axis. During the machining of holes the sample was moved past the stationary abrasive jet using a target scanning speed of 0.5 mm/s.

4.3 Results and Discussion

4.3.1 Erosion Rate Measurements

4.3.1.1 Erosion Rate Measurements of ABS

Figure 4.5 shows the erosion rate of ABS as a function of impact angle both without and with LN₂ cooling. At 30° incidence, the erosion rate is greater at room

temperature than with LN₂ cooling, but at a 90° impact angle, the erosion rate at room temperature was negative, implying a mass gain from embedding particles, as shown in Fig. 4.5. Such embedding has been reported previously in, for example, PMMA [11, 31].

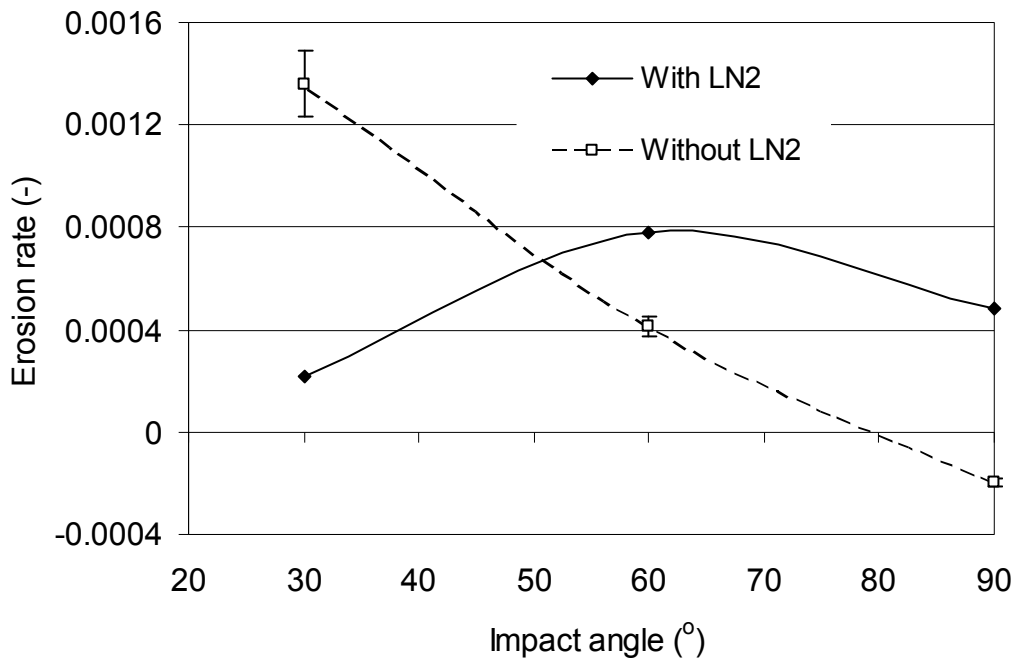


Figure 4.5 Erosion rate of ABS as a function of impact angle, with and without using LN₂. Experimental conditions: 25 μm Al₂O₃ particles, 760 μm round nozzle, abrasive jet pressure of 200 kPa, LN₂ pressure of 170 kPa, nozzle centreline to surface distance of 20 mm. Error bars represent ±standard error of the mean.

In order to compare the relative particle embedding with and without the use of LN₂, scanning electron microscopy (SEM) with energy dispersive x-ray spectroscopy (EDX) was used to map the relative amounts of Al₂O₃ particles remaining in the substrate after machining. For this purpose, a set of channels without metal masks were machined

with and without LN₂ at 30°, 60° and 90° impact angles, using the 760 μm round nozzle, and a 0.5 mm/s scan speed.

Half of the sample micro-machined at room temperature, and half of the sample micro-machined using LN₂, were analyzed simultaneously so that a direct comparison could be made. For example, the top half of Fig. 4.6 shows the results of the EDX mapping for the ABS sample machined at 90° without LN₂, and the bottom half shows the sample micro-machined using LN₂. The white dots represent the embedded Al₂O₃ particles. Similar figures obtained for ABS at 60°, 30°, PTFE at 90°, 60°, 30°, and PDMS at 90°, 60°, 30° are shown in Appendix A. Using digital image analysis software (ImageJ software - <http://rsb.info.nih.gov/ij/>), three randomly selected representative 0.5x0.5 mm areas were used to calculate the fraction of the total area covered by these white dots. Detailed steps of the image analysis are given in Section 7.1.4.

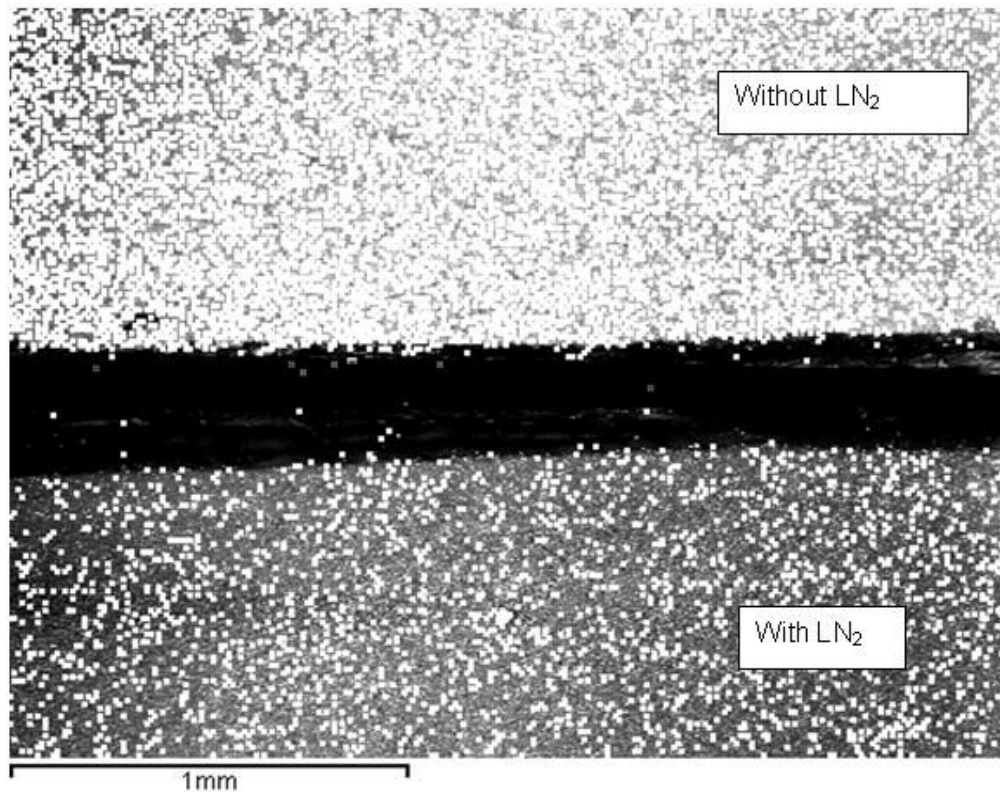


Figure 4.6 EDX analysis of surfaces when machining ABS with and without using LN₂ at 90° impact angle. White dots are embedded Al₂O₃ particles.

Figure 4.7 presents the average fractional area coverage for samples machined without and with LN₂. The area coverage by embedded particles when machining without LN₂ was highest at 90° impact angle. The result is consistent with previous observations for the embedding of quartz sand particles on polyethylene [33]. At all impact angles, the area covered by Al₂O₃ was decreased by machining with LN₂.

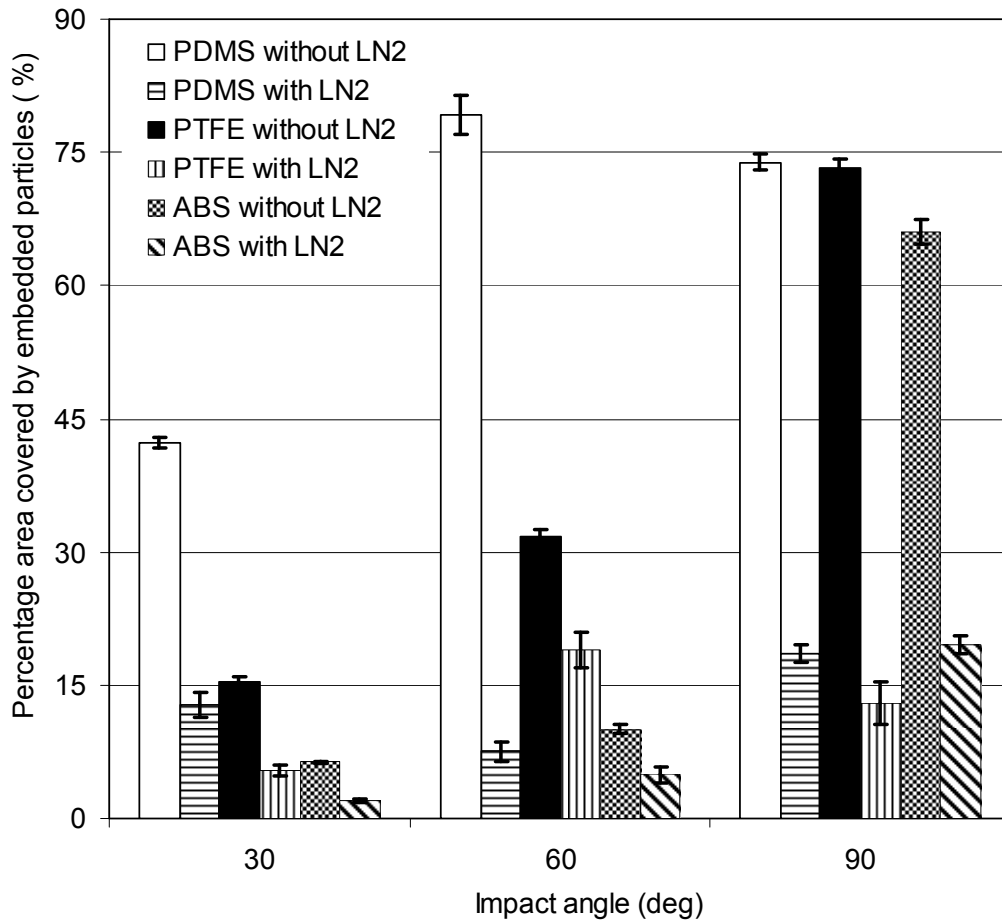


Figure 4.7 Average area coverage by Al_2O_3 particles between samples machined without and with LN_2 . The error bars show the standard error (the deviation of the mean value) based on three randomly selected representative, 0.5×0.5 mm areas, as explained in Section 4.3.1.1.

The greatest ABS erosion rate without LN_2 was observed at an impact angle of 30° , indicating a typically ductile erosive response at room temperature. This result is in agreement with the results reported for ABS [93]. However, when LN_2 was used, the peak of the erosion rate shifted to 60° , suggesting a change in the ABS removal mechanism as the temperature was reduced.

The observations indicate that the use of LN₂ allows for machining operations in ABS that must be performed at normal incidence, such as hole drilling, that are not possible at room temperature. The use of LN₂ also reduces particle embedding. However, oblique blasting of features such as channels in ABS is more efficient at room temperature, since the overall highest erosion rate is achieved at 30° under these conditions.

4.3.1.2 Erosion Rate Measurements of PDMS

Figure 4.8 shows for conditions used without the use of the LN₂, the erosion rate of PDMS became increasingly negative, i.e. a mass gain, with increasing impact angle, and it can thus be concluded that it is impossible to perform AJM of PDMS at room temperature. From the two curves in Fig. 4.8, it is clear that CAJM provides the ability to machine channels and drill holes in PDMS at all impact angles, which would otherwise be impossible.

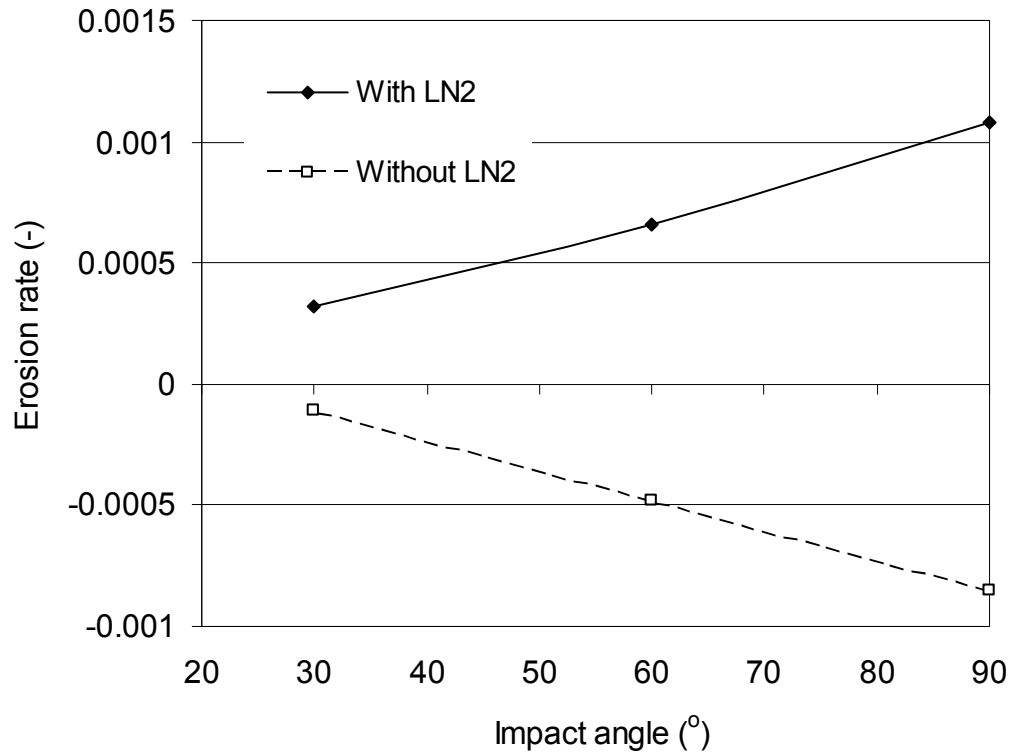
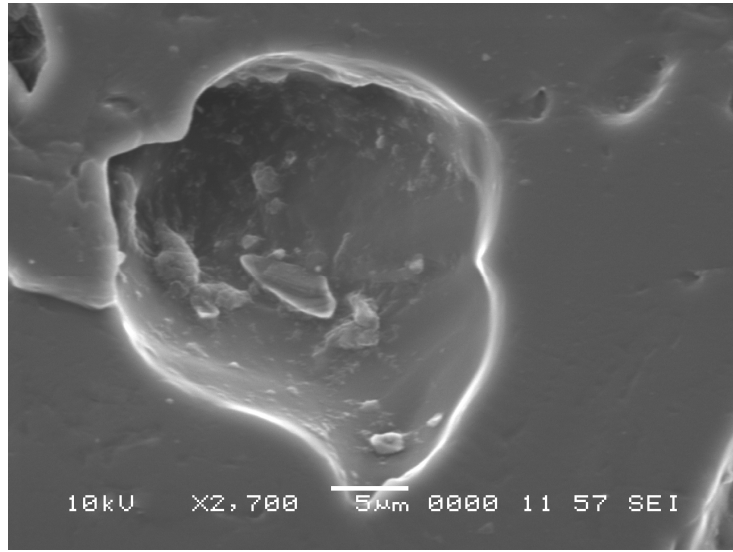
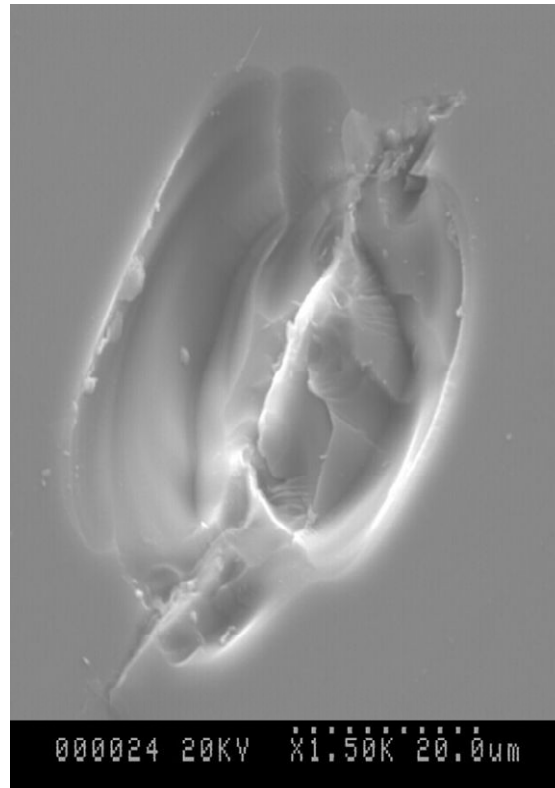


Figure 4.8 Erosion rate of PDMS as a function of impact angle, with and without using LN₂.

The erosion rate increased with an increase in impact angle when LN₂ was used, exhibiting a maximum at normal incidence, which is typical of a brittle erosive response, and indicates that the PDMS hardened at the cryogenic temperature. Evidence of material removal by chipping mechanisms is given in Fig. 4.9a, which compares PDMS machined under a cryogenic condition to glass machined under room temperature conditions (Fig. 4.9b) [94].



(a)



(b)

Figure 4.9 Individual impact site (a) in PDMS under cryogenic conditions and (b) in glass at room temperature condition showing similar micro-chipping mechanism of material removal.

From Fig. 4.7, it can be seen that the average area covered by embedded particles in the case of samples machined without LN₂ was very high at all impact angles. The high degree of particle embedding into the soft PDMS substrate at room temperature may be responsible for the inability to machine it, since the embedded particles likely shield the surface from successive particle impacts, as has been previously found for other polymers [12]. As expected, the average area coverage by embedded particles was smaller at a 30° impact angle, than it was at 90° and 60°; however, it is not clear why it was slightly larger at 60° than at 90°.

4.3.1.3 Erosion Rate Measurements of PTFE

Figure 4.10 shows the dimensionless erosion rate of PTFE as a function of impact angle both with and without LN₂ cooling. Ductile solid particle erosion behaviour is generally characterized by a peak erosion rate at shallow impact angles, e.g. 15°-30° [95, 96]. This behaviour was observed for PTFE machined at room temperature, which had a peak erosion rate at 30° incidence. The result is in agreement with previous results for other thermoplastic polymers [95, 96]. When LN₂ was used, however, PTFE showed a relatively weak dependence of erosion rate on impact angle with a maximum erosion rate at 60°, indicating that it eroded in neither a fully brittle nor ductile manner. From Fig. 4.7, it is seen that the average area covered by embedded particles when machining without LN₂ was greatest at 90°, which is the angle at which the difference in material removal rate with and without the use of LN₂ was also the largest. This result is

consistent with the hypothesis that embedded Al_2O_3 particles may shield the PTFE from further erosion. The difference in particle embedding when machining with and without LN_2 decreased as the impact angle decreased, narrowing the gap between the dashed and the solid curves of Fig. 4.10.

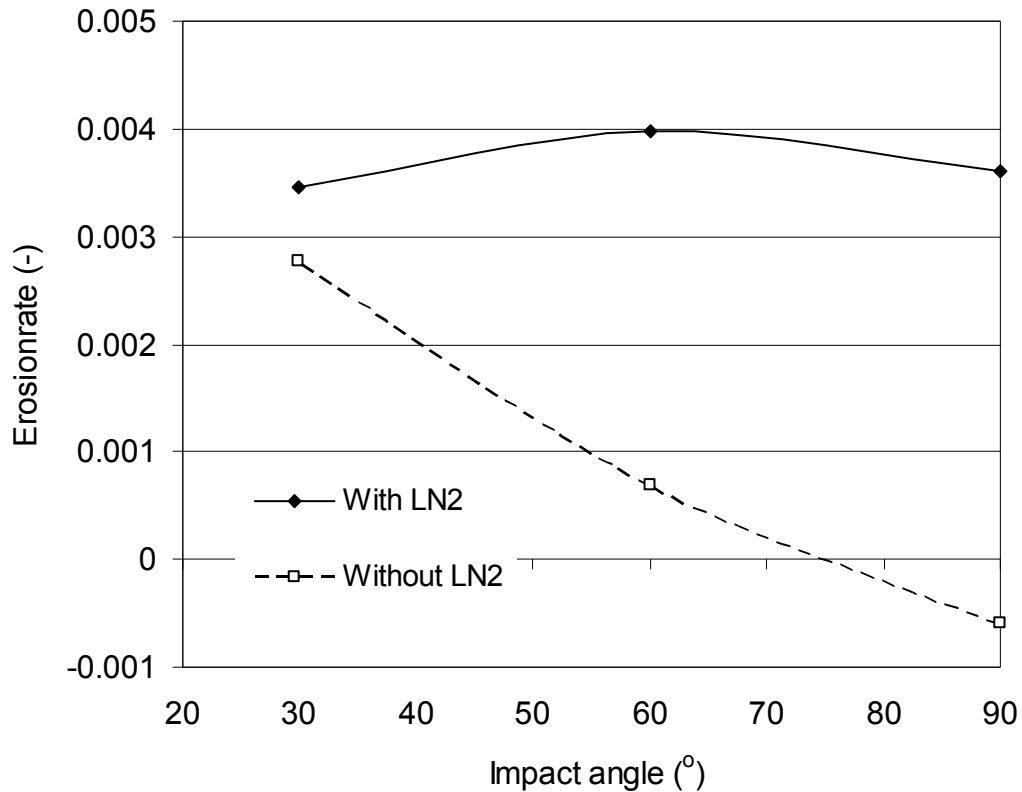


Figure 4.10 Erosion rate of PTFE as a function of impact angle, with and without using LN_2 .

It is concluded that CAJM of PTFE can be useful for drilling holes, since drilling is a micro-machining operation carried out at normal impact angle, where at room temperature the machining is not possible. CAJM can also be used to increase the machining rate for channels in PTFE at all angles of attack, with a greatly reduced particle embedding effect when compared to room temperature machining.

It was noted that the surface of the PTFE changed color from white before machining, to dark brown after machining at room temperature. Rao et al. [31] also saw a colour change from white to light brown after glass bead impact, and attributed it to heat generation during impact. However, they used a 1.18 mm diameter round nozzle with a very high blast duration of up to 15 min conditions that are much more aggressive than those used presently. In order to determine if local heating occurred that might influence the erosion rate when machining PTFE without LN₂, the analysis of Walley and Field [33] was used. The impact zone frequency, i.e. the average impact frequency (f_i) of erodent particles to an area (a) equal to the average crater size, can be calculated as follows:

$$f_i = \frac{\phi a}{m} \quad (4.1)$$

where $a=5.321 \times 10^{-4} \text{mm}^2 \pm 3.5 \times 10^{-5} \text{mm}^2$ (standard deviation) is the average crater size of 5 individual measurements, $m=3.191 \times 10^{-5} \text{mg}$ is the mass of one Al₂O₃ particle, and $\phi = 8.445 \text{kgm}^{-2}\text{s}^{-1}$ is the particle flux at the center of the jet. For the present conditions, $f_i = 141 \text{s}^{-1}$. The minimum frequency needed for thermal effects to be significant is given by [33]:

$$\tau = \frac{\kappa}{\rho_s C_p a} \quad (4.2)$$

where the density $\rho_s=2290 \text{kgm}^{-3}$, the specific heat $C_p=1.39 \times 10^3 \text{Jkg}^{-1}\text{K}^{-1}$ and the thermal conductivity $\kappa=0.333 \text{Wm}^{-1}\text{K}^{-1}$ are physical properties of the PTFE [97]. Since $f_i=141 \text{s}^{-1}$ was less than the calculated minimum frequency $\tau=196 \text{s}^{-1}$ needed for thermal effects to

be significant, it was concluded that heating was negligible in the present experiments and could not explain the darkening phenomenon. The reciprocal of Eq. (4.1) can also be used to obtain an order of magnitude estimate of the time interval between particle impacts, as also shown by both Hutchings and Levy [98] and Doyle and Ball [99].

The darkening in the present room temperature PTFE experiments was observed to decrease as the impact angle decreased, indicating that its likely cause was the embedding of the brown aluminum oxide particles. The result is supported by the observation that no significant darkening of the PTFE surface was observed at any impact angle when the LN₂ was used and, therefore, the embedding was greatly reduced, as shown in Fig. 4.7. Further support for this hypothesis came from a simple machining experiment in which the brown aluminum oxide powder was replaced by an otherwise identical white aluminum oxide powder, resulting in much less darkening of the PTFE after machining (Fig. 4.11).

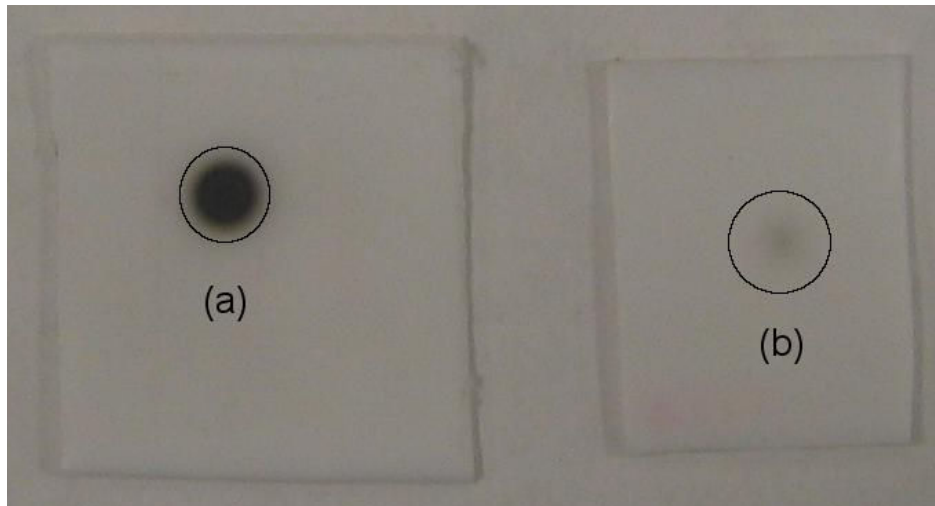


Figure 4.11 PTFE sample machined with (a) brown Al₂O₃ and (b) with white Al₂O₃. Machined under ambient temperature conditions at 90° impact.

4.3.2 Masked Channels and Holes

The primary objective of these experiments was to investigate the possibility of using LN₂ cooling to micro-machine features in polymers that are otherwise impossible or difficult to machine at room temperature. Figure 4.12 shows 3D optical profilometry (described in Section 3.4) scans of the channels and holes micro-machined in PTFE, ABS and PDMS using CAJM under identical conditions for each of the polymers. Although the shapes are broadly similar, differences exist in the depth and sidewall slopes. Figures 4.13a and 4.13b show the cross-sectional profiles of the channels and the holes. The average maximum depth obtained per pass for the channels was 15 μm for PTFE, 7.5 μm for ABS and 6.7 μm for PDMS. By way of comparison, previous experiments with PMMA under identical conditions but at room temperature gave 36 μm/pass [11].

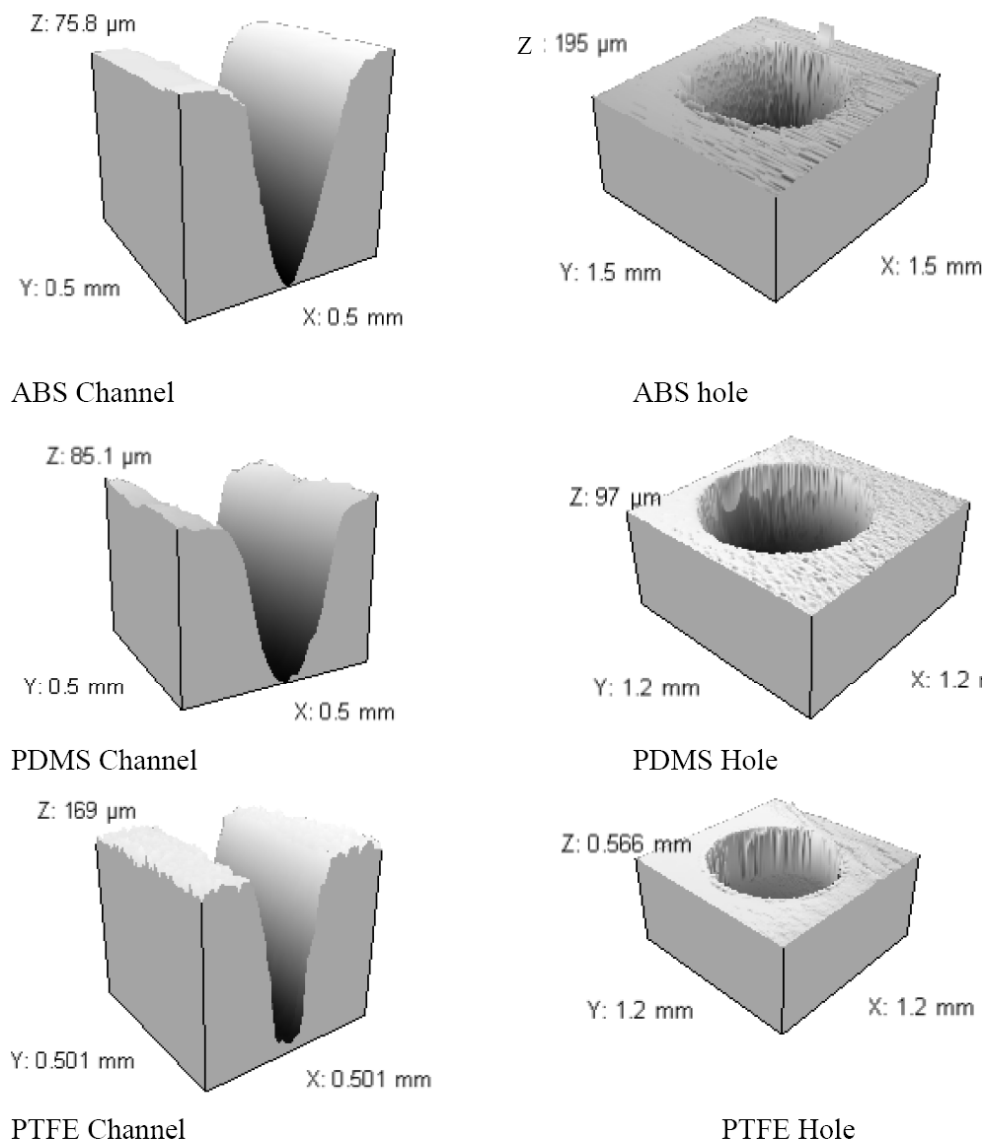
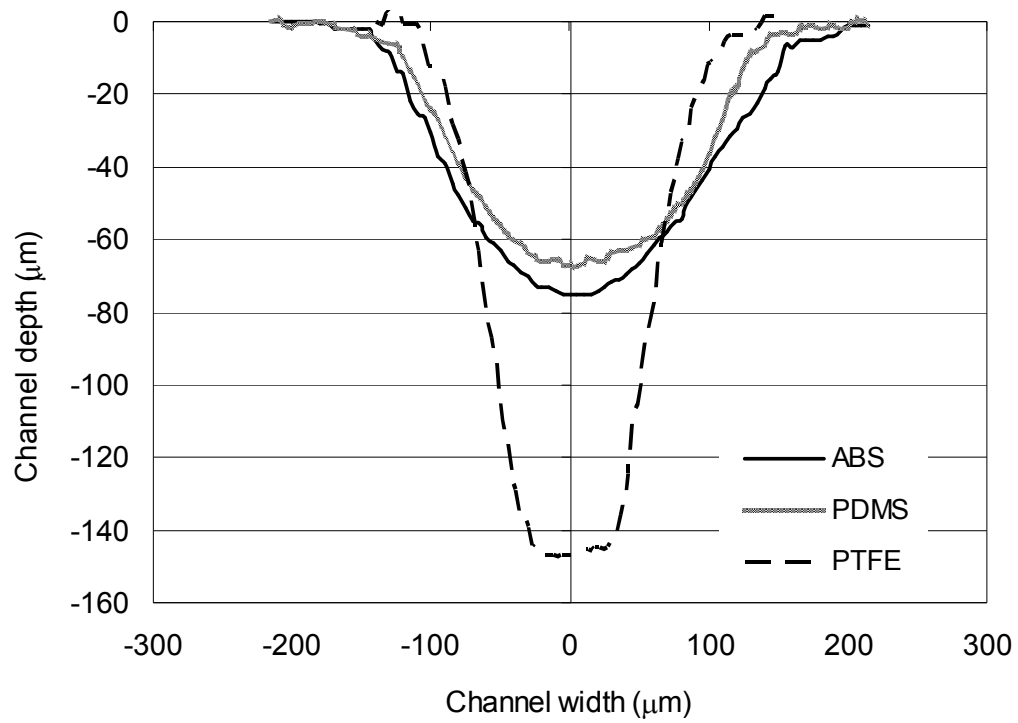
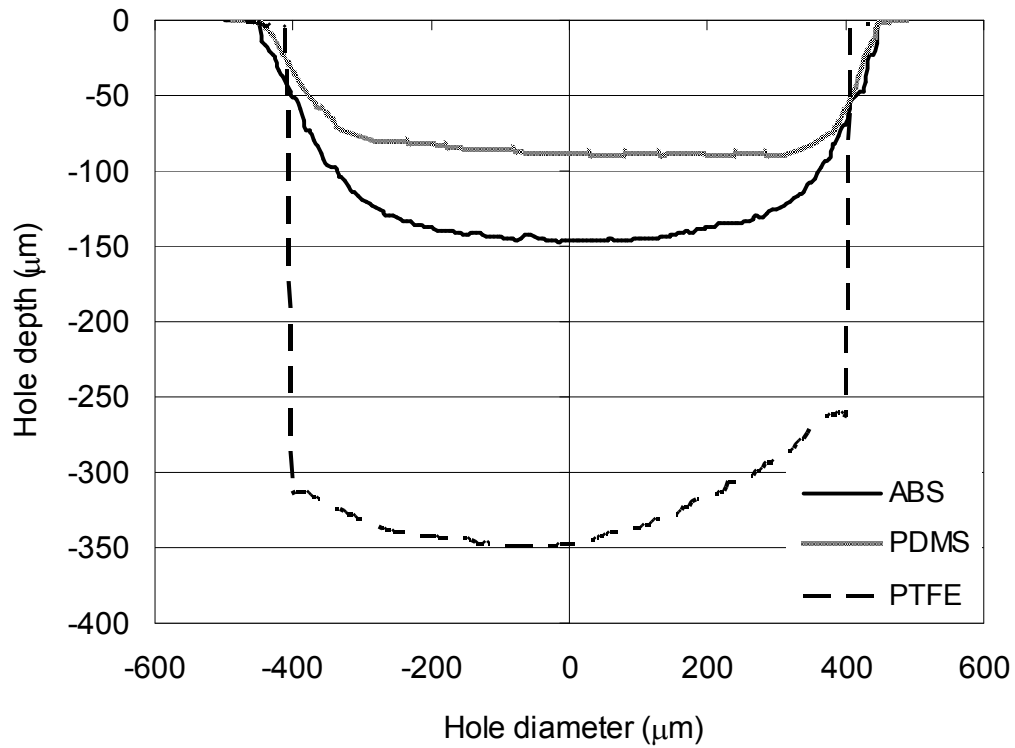


Figure 4.12 Three dimensional profiles of channels and holes micro-machined in three polymers using CAJM. Experimental conditions: LN_2 pressure of 170 kPa, rectangular 0.3 mm x 3.8 mm slot nozzle launching 25 μm Al_2O_3 particles at normal incidence, abrasive mass flow rate of 5.21 g/min, abrasive jet pressure of 200 kPa. Channel profiles shown after ten 1 mm/s passes and hole profiles shown after eight 0.5 mm/s passes.

The average sidewall angles, measured from the horizontal, of the channels in figure 4.13 a were found to be 19° for ABS, 38° for PDMS and 67° for PTFE. The slope of the PTFE channel was approximately equal to that of a PMMA channel (72°) of approximately equal depth machined at room temperature [11]. The steep sidewalls and relatively flat bottoms found in the PTFE channels and holes machined using CAJM, were probably due to the weak dependence of erosion rate on the impact angle. On the other hand, the shallower slopes observed when using LN₂ cooling with PDMS and ABS are consistent with an increasing amount of brittle erosion which tends to slow the lateral erosion of sidewalls as they steepen [100].



(a)



(b)

Figure 4.13 Cross sectional profiles of: (a) channels and (b) holes machined using CAJM.

The sidewall slopes of the holes followed a similar trend as seen in figure 4.13b, with a 50° sidewall angle for ABS, 57° for PDMS and almost 90° for PTFE. The slopes were steeper for the holes than the channels simply because the holes were machined to a greater depth.

The average surface roughness of the bottoms of the holes was measured using a mechanical stylus profilometer described in Section 3.4 and found to be 0.26 μm for PDMS, 0.23 μm for ABS and 0.41 μm for PTFE. These values are less than the 0.6-0.9 μm and 0.6-0.8 μm ranges obtained for PMMA, and borofloat glass, respectively, at room temperature [94].

It was also of interest to determine if the application of LN_2 caused an increase in the erosion of the steel masks used in the machining of the channels and holes. Optical profilometer scans of the steel mask surfaces after blasting under the given conditions with, and without LN_2 , indicated that 0.036 mm^3 and 0.025 mm^3 , respectively, of mask material were removed per gram of blasted aluminum oxide. These low material removal rates suggest the possible use of steel shadow or contact masks for patterning for device fabrication using CAJM.

4.4 Chapter Summary

The major findings of this chapter can be summarized as follows:

- (a) The novel cryogenic abrasive jet micro-machining apparatus was found to be effective in cooling the target materials thus enabling the micro-machining of PDMS, and enhancing the erosion rates in ABS and PTFE.
- (b) PDMS targets: AJM at room temperature was impossible at all angles of attack. CAJM allowed the drilling of holes and machining of channels at all impact angles.
- (c) PTFE targets: AJM at room temperature was impossible at normal incidence. CAJM improved the etch rate, and allowed the drilling of holes and the machining of channels, at all impact angles.
- (d) ABS targets: AJM at room temperature was impossible at normal incidence. CAJM allowed the drilling of holes at normal incidence and improved the etch rate of holes and channels machined at intermediate angles of attack.
- (e) At all angles of attack and for all the tested materials, CAJM reduced the amount of particle embedding. Polymeric materials that show a high degree of particle embedding and an incubation period at room temperature, such as ABS and PTFE, could efficiently be machined using CAJM at normal impact which is of particular importance in drilling through holes.
- (f) CAJM resulted in smoother surface finishes in all investigated polymers as compared to surface finishes obtained in PMMA and borofloat glass when machined under ambient temperature conditions.

5 Thermal Analysis of Cryogenically Assisted Abrasive Jet Micro-machining of PDMS

The previous chapter demonstrated the feasibility of machining a number of polymers including PDMS using CAJM. This chapter presents a detailed analysis of the heat transfer mechanisms occurring in CAJM, and demonstrates ways in which the process can be optimized to achieve the minimum required cooling. Heat transfer analyses of the cryogenic machining of PDMS were conducted for two purposes: (i) to determine the rate of cooling in the current CAJM setup for efficient machining, and (ii) to determine the effect of the thermal strains that occur during cooling on the final room-temperature shapes of the micro-machined features. The finite element predictions were compared with experimental results. Much of the material in this chapter has been published in [101, 102].

5.1 Experiments

5.1.1 CAJM Experiments

Masked and unmasked channels and unmasked holes were machined in PDMS using the CAJM setup described in Section 4.1 and experimental conditions described in Section 4.2. The PDMS samples (Sylgard[®] 184 silicone elastomer, Ellsworth Adhesives, Germantown, WI, USA) were cured in a vacuum oven for 4 h at 75 °C. All experiments at a given condition were repeated three times, and profiles of the machined features were measured using the optical profilometer described in Section 3.4.

The unmasked CAJM of channels and holes was performed using the 760 μm inner diameter nozzle described in Section 3.3 at an abrasive (granular aluminum oxide powder of 25 μm , Fig. 4.4) mass flow rate of 2.83 g/min (standard deviation of 3 measurements = 0.12 g/min). To evaluate the speed of the erosion front with the nozzle stationary (Section 5.2.1), three unmasked holes were machined with the nozzle held over a stationary target for 50 s. The maximum depths of the holes were measured to be 101 μm , 113 μm and 107 μm (107 μm average), corresponding to an average etch rate at the center of the hole of 2.14 $\mu\text{m/s}$ over the 50 s dwell time. The fastest etch rate of 2.26 $\mu\text{m/s}$, corresponding to the maximum hole depth of 113 μm , will be used in Section 5.2.1 to compare the speed of the thermal propagation front to that of the erosion front in the PDMS. To evaluate the machinability of PDMS at temperatures above the glass

transition (Section 5.2.2.3), three unmasked channels were machined in PDMS at a 2 mm/s scan speed and the maximum center depths were 5.7 μm , 4.6 μm and 4.8 μm (i.e. an average value of 5 $\mu\text{m} \pm 0.6 \mu\text{m}$).

For the CAJM of the masked channels the steel plates described in Section 3.2 were clamped approximately 500 μm apart onto the target to act as the masks. The rectangular slot nozzle, described in Section 3.3, was held stationary and the target sample was scanned in front of it using a computer controlled linear stage having $\pm 1 \mu\text{m}$ accuracy. Three masked micro-channels were machined at a 0.5 mm/s scan speed, and the maximum depths at the center of the micro-channels were measured using the optical profilometer described in Section 3.4, as 89 μm , 78 μm and 84 μm (i.e. an average value of 84 μm).

5.2 Heat Transfer Analysis of CAJM for PDMS Targets

In previous studies it was hypothesized that PDMS cannot be machined using an abrasive jet unless it is cooled sufficiently; e.g. below its glass transition temperature (Chapter 4). Therefore, for CAJM to be effective the PDMS should be cooled adequately to a depth that is at least as large as the machined depth. In other words, the thermal cooling front must advance into the target at a rate that is higher than the material removal rate. If the thermal front advances much faster than the material removal rate, the temperature distribution can be obtained by neglecting the motion of the heat sink

relative to the eroding solid boundary. On the other hand, a moving boundary heat transfer analysis is required when the thermal front moves at a speed that is comparable to the erosion front.

5.2.1 CAJM of holes in PDMS: Stationary Heat Sink

In this case, the heat sink (i.e. the cryogenic jet) is stationary over the target and, as will be shown later, because of the high heat flux obtained in the current experimental setup, the speed at which the thermal front advanced was much greater than that of the erosion front. Consequently, the temperature distribution could be solved as if the heat sink were acting on a stationary interface. To determine the cooling rate, the PDMS target was considered to be a semi-infinite, 4 mm thick slab, initially at a uniform temperature, $T(x, t=0) = T_i$ and subject to convective cooling by the cold abrasive jet having temperature $T_\infty < T_i$. The initial temperature was assumed 25 °C throughout the PDMS. Heat conduction on the back face was assumed to be negligible. This one-dimensional transient heat conduction problem is described by [103]:

$$\frac{\partial^2 T}{\partial x^2} = \frac{1}{\alpha_{td}} \frac{\partial T}{\partial t} \quad (5.1)$$

where T is the temperature (K) and α_{td} is the thermal diffusivity (m^2s^{-1}). The appropriate surface convection boundary conditions and initial condition are given by:

$$\left. \frac{\partial T}{\partial x} \right|_{x=0} = 0, \quad (5.2)$$

$$-\kappa \left. \frac{\partial T}{\partial x} \right|_{x=L} = h_c [T_\infty - T(L, t)] \quad \text{for } t > 0 \quad (5.3)$$

$$T|_{t=0} = T_i \quad (5.4)$$

where $x=0$ and $x=L$ represent the back and the front side (on which the jet impinges) of the slab, respectively. The solution to Eq. (5.1) is [103]:

$$T(x, t) = T_i + (T_\infty - T_i) \left\{ 1 - \operatorname{erf} \left(\frac{x}{2\sqrt{\alpha_{id}t}} \right) - \left[\exp \left(\frac{h_c x}{\kappa} \right) + \frac{h_c^2 \alpha_{id} t}{\kappa^2} \right] \left[1 - \operatorname{erf} \left(\frac{x}{2\sqrt{\alpha_{id}t}} + \frac{h_c \sqrt{\alpha_{id}t}}{\kappa} \right) \right] \right\} \quad (5.5)$$

The PDMS density (ρ), thermal conductivity (κ) and specific heat capacity (C_p) were assumed constant. Their values ($\rho=970 \text{ kgm}^{-3}$, $C_p=1.46 \times 10^3 \text{ Jkg}^{-1}\text{K}^{-1}$, $\kappa=0.15 \text{ Wm}^{-1}\text{K}^{-1}$, $\alpha_{id}=\kappa/\rho C_p$) were obtained from a polymer data book [97]. The initial target temperature (T_i) was assumed to be uniform at room temperature (25 °C). It was assumed that the convective heat flux due to the gas flow would not be affected significantly by the abrasive particles in the jet since the particle flux was relatively sparse and the particles were in contact with the cooled jet only during their brief flight over the 20 mm stand-off. The average convective heat transfer coefficient, $h_c=916 \text{ Wm}^{-2}\text{K}^{-1}$, was calculated using the model described in [104] for an impinging jet. Figure 5.1 shows the temperature distribution at various positions, as predicted by Eq. (5.5). The

curve at 0.02 μm corresponds to the thickness of a typical chip removed during blasting, as discussed below.

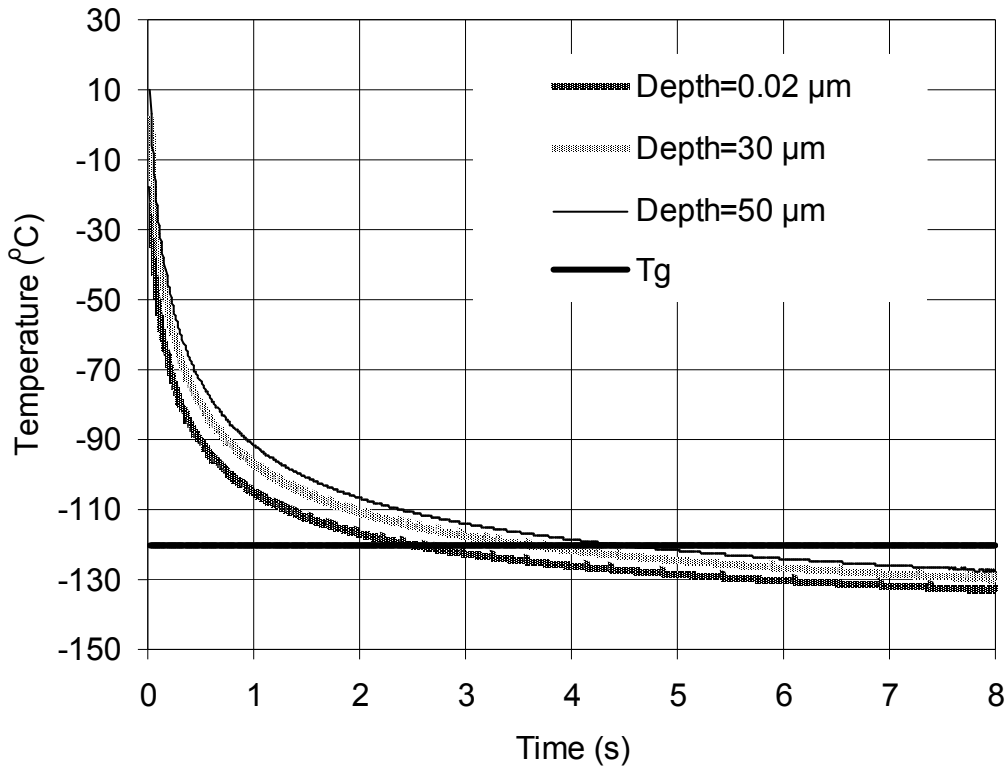


Figure 5.1 Temperature at different depths within the target as a function of time for a stationary cooling jet predicted by Eq. (5. 5). The depth into the surface is measured from the front side of the target; i.e. from the surface on which the jet impinges. The bold solid horizontal line shows the glass transition temperature (T_g) of PDMS (-120°C).

The propagation of the thermal front into the substrate (i.e. the time required to reach the -120 °C glass transition temperature at different depths within the PDMS target) can be inferred from Fig. 5.1, and is plotted for shallower depths in Fig. 5.2. Figure 5.2 also shows the location of the erosion front at the center of the machined hole as it moves with the average constant etch speed of 2.26 $\mu\text{m/s}$ (113 $\mu\text{m}/50$ s, the highest etch rate measured in Section 5.1.1). Figure 5.2 demonstrates that, under the present conditions,

the thermal front propagation into the substrate was nearly twelve times faster than the erosion front of the stationary nozzle as the jet machined a hole. This fast thermal propagation implies that the target PDMS was being cooled more than necessary and that the CAJM process could be further optimized to conserve LN₂ by decreasing its flow rate, or perhaps by pulsing the LN₂ jet so that the surface was only cooled periodically.

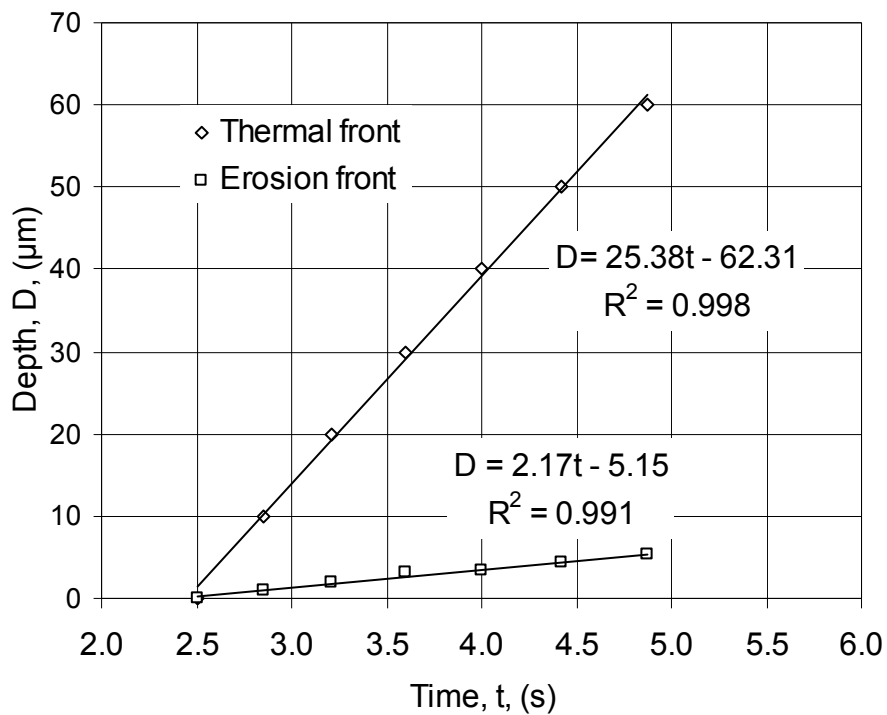


Figure 5.2 Depth into the PDMS target of thermal front at $T_g = -120$ °C predicted by Eq. (5. 5), and location of erosion front (based on maximum etch rate) as a function of time. Zero depth corresponds to the surface once it reached -120 °C and erosion began.

It is useful to apply the results of Fig. 5.2 to the machining of a single average chip from the PDMS erosion front. Assuming that each particle removes a cylindrical chip having a diameter equal to the equivalent spherical diameter of the particle ($25 \mu\text{m}$), the average time interval (t_i) between particle impacts at the center of the hole in a

surface zone equal to the projected particle area ($a=4.909 \times 10^{-4} \text{ mm}^2$) was calculated using the reciprocal of Eq. 4.1. For the present system, (760 μm nozzle, 20 mm stand-off distance, 2.83 g/min flow rate, $\phi=8.445 \text{ kgm}^{-2}\text{s}^{-1}$), the reciprocal of Eq. (4.1) yields $t_i=7.7$ ms. The thickness of a target chip removed by a single particle is then $s=(113 \mu\text{m}/50 \text{ s}) \times 7.7 \times 10^{-3} \text{ s}$ ($s \approx 0.02 \mu\text{m}$), and the time to cool this chip is 0.7 ms (rate of thermal front advance $25.38 \mu\text{ms}^{-1}$; Fig. 5.2) – much shorter than the estimated average time between impacts ($t_i=7.7$ ms).

The comparison of the time required to cool a chip with the time between impacts is helpful in establishing the limit for the validity of the present heat transfer analysis; i.e. the assumption of a stationary heat transfer boundary. This assumption is valid as long as the rate of heat transfer is sufficient to cool the target to the desired minimum temperature in the average time between impacts.

5.2.2 CAJM of Unmasked Channels in PDMS: Moving Heat Sink

The micro-machining of channels requires that the target move relative to the abrasive and cooling jets. In CAJM, both the erosive energy and cooling rate vary across the jet. Therefore, for effective machining it is important to know the effect that scan speed has on both the target temperature and the resulting erosion rate. In particular, it is of interest to determine what portion of the target covered by the jet footprint is below a certain temperature. An analytical solution for the transient temperature field in a half-

space under a moving circular heat source or sink of prescribed heat flux was presented in [105]. The current problem, however, involved a different boundary condition - the prescribed convective heat transfer coefficient of a moving cooling jet, as illustrated in Fig. 5.3. The problem was solved using a finite element model based on the ANSYS Parametric Programming Language.

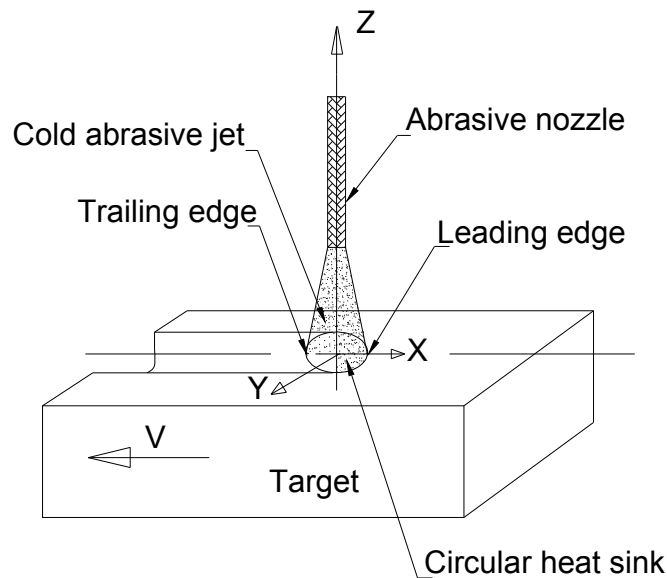


Figure 5.3 Leading and trailing edges of scanning abrasive/cooling jet.

5.2.2.1 FE Model of Moving Heat Sink

The moving cooling jet was simulated by shifting the surface loads (convective heat transfer coefficient and jet temperature at the surface of the PDMS) from one set of elements representing the 6 mm diameter heat sink to another set at each time step (Fig. 5.4). A similar approach has been employed by a number of researchers [106, 107] to investigate the moving heat source problem in laser machining operations.

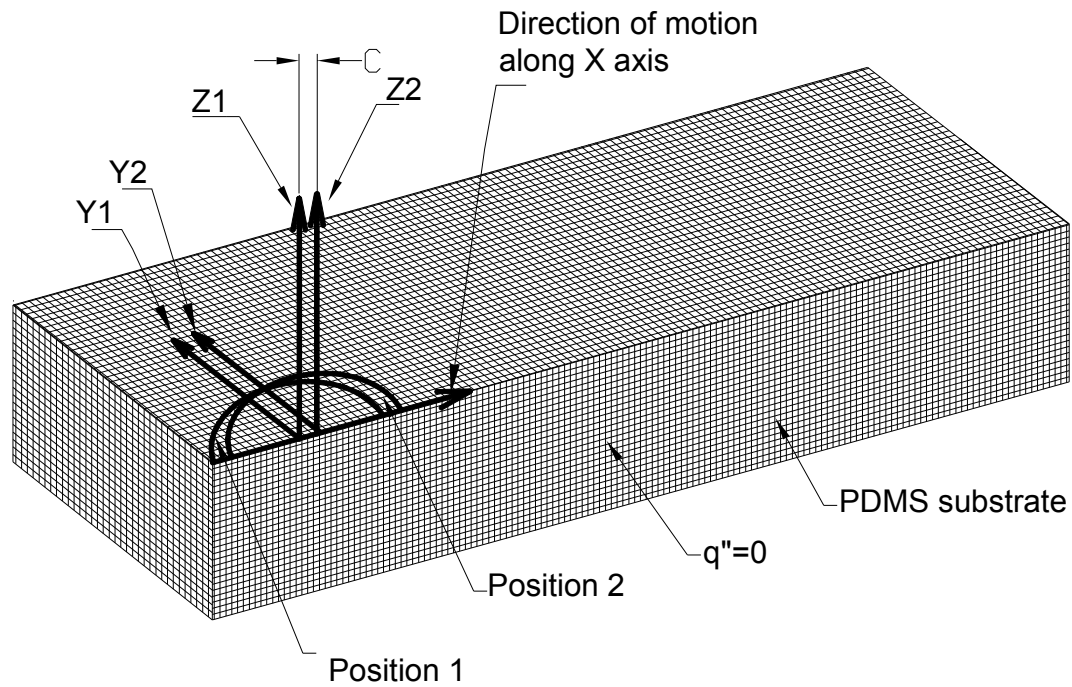


Figure 5.4 Schematic of the moving circular heat sink and the meshed half model exploiting symmetry. C is the distance between two sets of elements. The semi-circles show areas to which h and T are applied as the heat sink moves in the positive X -direction. Zero heat flux was assumed on the plane of symmetry.

The convective heat transfer coefficient (h_c) was assumed to have a Gaussian distribution (Fig. 5.5) over the 6 mm diameter impingement area (footprint) of the circular jet [108].

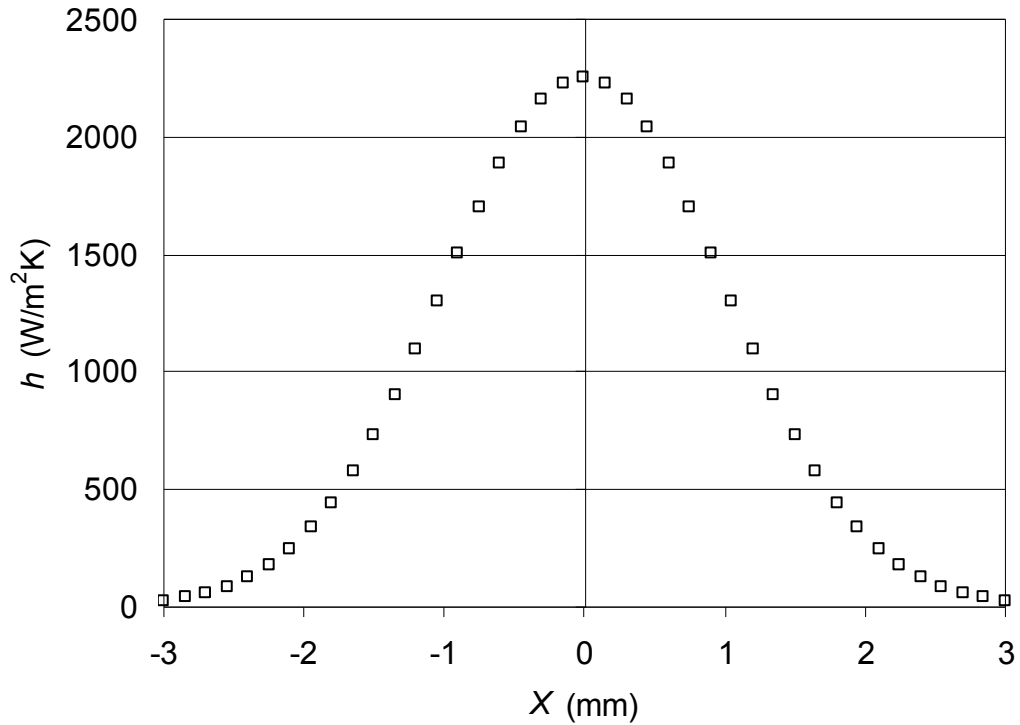


Figure 5.5 Gaussian distribution of the heat transfer coefficient, h , over the 6 mm diameter impingement area estimated using the correlation of [104].

The mean value of the heat transfer coefficient over this footprint was estimated to be $916 \text{ Wm}^{-2}\text{K}^{-1}$ using the correlation of [104]. Therefore, a Gaussian distribution of h_c over the 6 mm diameter impingement area implies a peak value of $2,255 \text{ Wm}^{-2}\text{K}^{-1}$ at the center of the jet with a standard deviation of $216 \text{ Wm}^{-2}\text{K}^{-1}$. The jet temperature was assumed to be $-150 \text{ }^\circ\text{C}$ and the PDMS was assumed to be initially at $25 \text{ }^\circ\text{C}$. The modeled geometry of the PDMS was a slab that was 75 mm long in the direction of scanning, 5 mm wide and 2 mm thick. This model length ensured sufficient time for the establishment of a steady-state temperature distribution in the PDMS around the moving cooling jet.

The PDMS was meshed with Solid70 thermal elements utilizing the symmetry along the axis of jet motion. Zero heat flux was assumed on the plane of symmetry. The elements were cube-shaped, 0.15 mm on each side, which resulted in a Biot number $\left(Bi = \frac{h_c \Delta x}{\kappa} \right)$ approximately equal to 1 over the element depth using the average convective heat transfer coefficient $h_c=916 \text{ Wm}^{-2}\text{K}^{-1}$ and thermal conductivity $\kappa=0.15 \text{ Wm}^{-1}\text{K}^{-1}$. The small Biot number implies that temperature gradients over the 0.15 mm depth of the surface elements, and certainly over the 0.02 μm depth of a single micro-machined chip ($Bi=0.00012$), were negligible (Section 5.2.1). Therefore, it was only necessary to demonstrate that the mesh was sufficiently fine to give a converged surface temperature. Using a finer mesh of 0.125 mm resulted in a relatively small change in surface temperature (less than 2 °C) for a scan speed of 1 mm/s; therefore, a mesh of 0.15 mm was used throughout. A similar approach, in which the element size was reduced until the change in temperature at the surface was less than 3 °C, was employed in [109] to simulate a laser welding process. For the transient heat transfer analysis occurring at each jet position (Fig. 5.4), the time step size was automatically determined within ANSYS. The length of the dwell time of the jet at each position was set as the distance between consecutive positions (C in Fig. 5.4) divided by the jet scan speed.

5.2.2.2 *Verification of Model*

The validity of the predictions of the FE model, and thus also the use of the assumed Gaussian heat transfer coefficient distribution, were assessed by comparing the predicted and measured temperatures at the center of the moving jet. T-type thermocouples (500 μm bead radius) were embedded by immersing them in the liquid PDMS resin and holding them in position with the bead against the bottom of the mould as the PDMS cured. These unmasked PDMS samples were then machined at various scan speeds using the CAJM setup. The location of the thermocouples was aligned with the center of the jet and the temperature was monitored using a thermocouple reader with 0.8 $^{\circ}\text{C}$ accuracy (FLUKE[®] 714 thermocouple calibrator, Fluke Corporation, USA). Each experiment at a given scan speed was repeated twice. As the cold abrasive jet passed over the thermocouple, the surrounding PDMS was eroded only slightly (less than about 5 μm), and this effect could be neglected. Table 5.1 compares the measured minimum temperatures with those predicted by the FEA at a depth equal to the bead radius.

Table 5-1 Comparison of measured temperatures at the center of an unmasked channel with the corresponding FE-predicted results at different scan speeds.

Scan Speed (mm/s)	Measured Minimum Temperature		FEA Minimum Temperature T (°C)	Difference between average exp. value and FEA (%)
	Exp.1, T (°C)	Exp. 2, T (°C)		
2	-73	-76	-60	20
1	-98	-102	-79	21
0.5	-115	-111	-88	22
0.3	-138	-134	-94	31

The measured minimum temperature agreed reasonably well with that at the center of the jet footprint indicating the suitability of the assumed heat transfer coefficient. Although the agreement was not as good at the lowest scan speed, for the typical scan speeds used in AJM and in this work (0.5 mm/s), the predicted and measured temperatures were within 22% of each other.

To gain further confidence in the present FE approach, the FE surface boundary condition was changed to a moving circular heat sink with a uniform heat flux distribution ($q''=9500 \text{ Wm}^{-2}$), and the results were compared with the analytical solution under these conditions from Ref. [105]. Figure 5.6 shows that the predicted surface temperature distribution along the center of the jet path ($Y=0$, Fig. 5.4) in the direction of motion (X -axis) of the two models agreed closely. Appendix B gives details of the analytical solution.

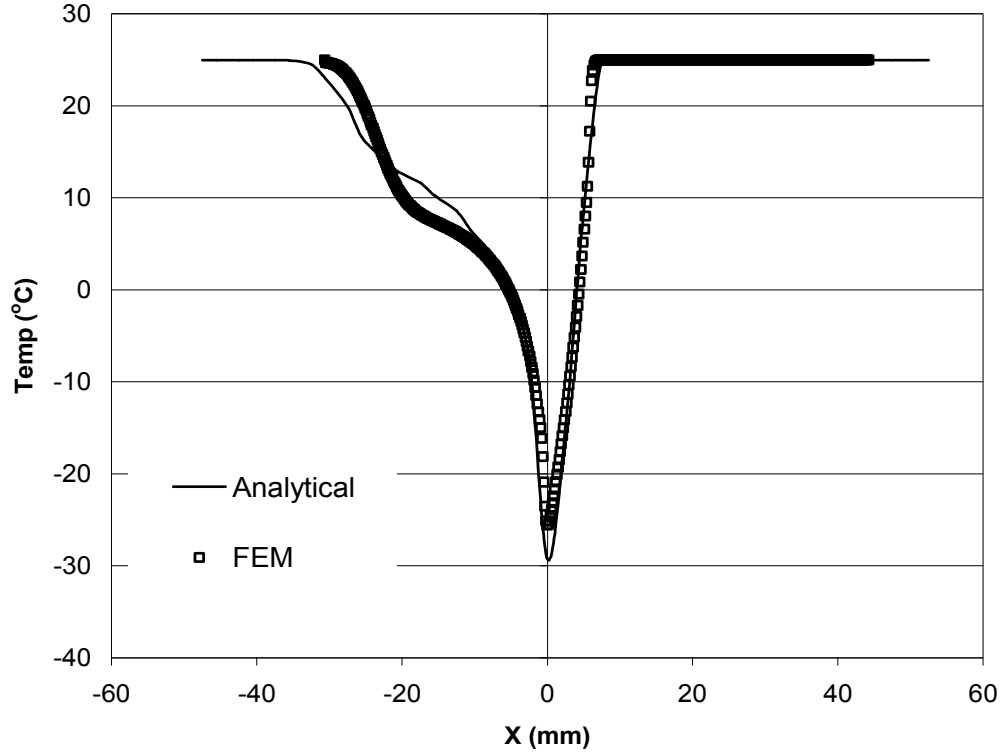


Figure 5.6 Temperature distribution in PDMS predicted by the analytical and finite element models at the surface along the direction of motion (X -axis) through the center of the circular cooling jet ($Y=0$) for $q''=9500 \text{ W/m}^2$, $r=3 \text{ mm}$. $X=0$ represents the center of the moving jet.

5.2.2.3 *Surface Temperature Distribution along Scanning Direction for Unmasked Channels*

Figure 5.7 shows the surface temperature distribution along the center of the jet path ($Y=0$, Fig. 5.3) in the direction of motion (X -axis) at different scan speeds. As described above, the heat transfer coefficient was assumed to have a Gaussian distribution with an average value of $916 \text{ Wm}^{-2}\text{K}^{-1}$.

In Fig. 5.7, negative values of X correspond to material that is in the wake of the jet, and machining can occur anywhere over the 6 mm jet diameter. The surface temperatures of Fig. 5.7 can be used to estimate the temperature distribution inside the substrate at a depth equal to $0.02\ \mu\text{m}$, which was the approximate thickness of the chip of PDMS removed by an impacting aluminum oxide particle. The results of Section 5.2.1 indicate that the newly exposed surface after chip removal was sufficiently cooled for machining prior to the impact of the next chip at that same location. Therefore, the model represents the temperature distribution of the near-surface region throughout the machining. The effect of the distribution of h_c (Gaussian vs. uniform) was also investigated and it was found that the uniform h_c distribution produces lower temperatures, particularly ahead of the jet centerline ($X=0$). Appendix C gives details of the comparison.

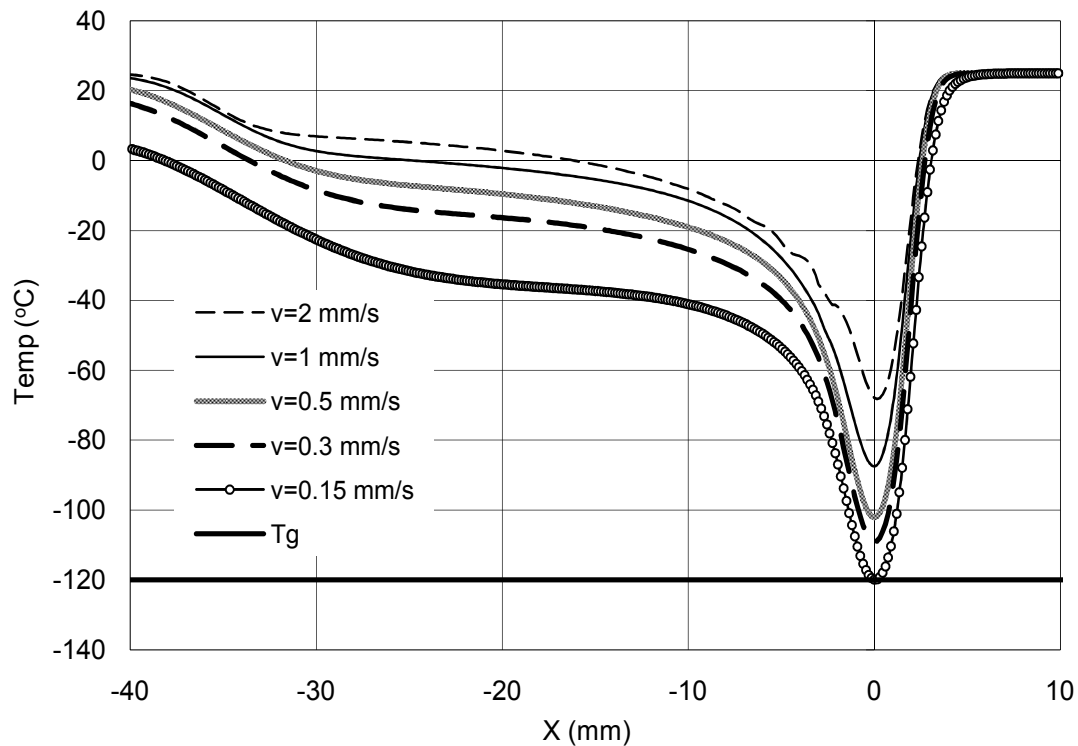


Figure 5.7 Temperature distribution in PDMS predicted by the finite element model at the surface along the direction of motion (X -axis) for different scan speeds through the center of the circular cooling jet ($Y=0$). The bold solid horizontal line shows the glass transition temperature (T_g) of PDMS (-120°C). $X=0$ represents the center of the moving jet and negative X corresponds to material in the wake of the jet.

As expected, the temperature falls at a given position within the 6 mm jet footprint and behind it as the scan speed decreases. Although the minimum temperature is reached at the center of the jet, the distribution is highly asymmetric with much more cooling occurring in the wake.

Although the present model assumed that the abrasive jet and the cooling jet occupied the same volume, it may be more efficient for the cold jet to precede the abrasive jet so that cooling occurs sooner for a given scan speed and heat transfer

coefficient. Also, it is possible to overlap the cold jets to obtain larger footprint. The temperature distribution at the surface of the target material in case of overlapping heat sinks was also investigated. It was found that the largest distance cooled (5.5 mm) to a temperature of -67°C (possible to machine PDMS) was obtained when the heat sinks were situated 3 mm apart from their centers, i.e. when the trailing edge of the leading heat sink was coincident with the center of the trailing heat sink. Appendix D gives the details.

Figure 5.7 makes it possible to investigate the relationships between erosion, the heat transfer of the cooling jet and the resulting target temperature. For example, the experiments of Section 5.1.1 showed that it was possible to machine an unmasked channel in PDMS to an average center depth of $5\ \mu\text{m}$ after one pass at a 2 mm/s scan speed. Figure 5.7 suggests that the centerline temperature was approximately $-67\ ^{\circ}\text{C}$ at this scan speed, suggesting the possibility that a medium other than LN_2 , such as dry ice, could be used to effectively cool the PDMS substrate.

Because the present set-up suggested that the LN_2 flow could be optimized, a few improvements to the LN_2 dispensing equipment were proposed for future consideration (Appendix E). It is noted that for effective machining of channels it is not only the cooling temperature that should be considered, but also the dose of particles the target sees at a given scan speed. The effect of changing particle dose received per unit area on the erosion rate was investigated. For example, scan speeds of 3 mm/s produced

negligible erosion at a mass flow rate of 2.83 g/min. However, when the particle mass flow rate was increased to 6.1 g/min, an appreciable erosion rate could be measured at the same scan speeds of 3 mm/s. Details are presented in Appendix F.

5.2.3 CAJM of Masked Channels in PDMS: Moving Heat Sink

The cooling of the masked channels was modeled using FEA in the same manner as described in Section 5.2.2.1, except that that the cooling jet footprint was rectangular (Fig. 5.8) with a width of 0.6 mm (width of mask opening, i.e. 4 x 0.15 mm, which is the element size) and a length of 6 mm (size of jet in scanning direction).

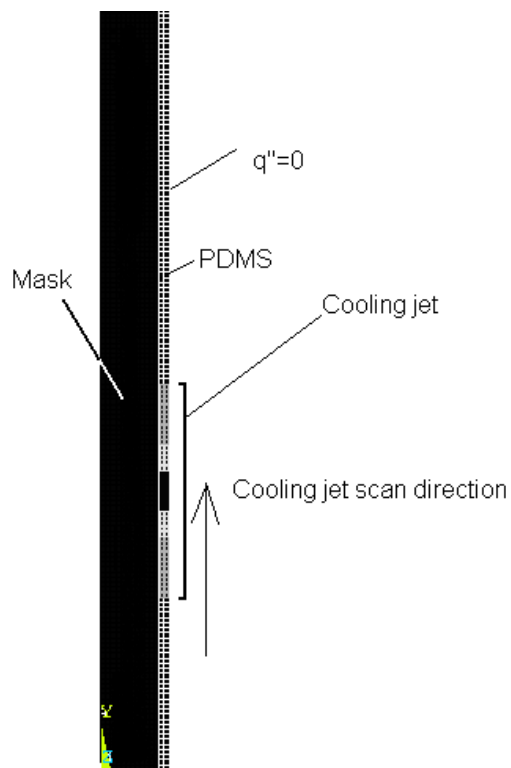


Figure 5.8 Schematic of the moving rectangular heat sink and the meshed half model exploiting symmetry.

Figure 5.9 shows the temperature distribution along the direction of motion (X -axis) through the center of the rectangular jet (centerline of the mask). The trends are similar to those seen in Fig. 5.7 for the unmasked case.

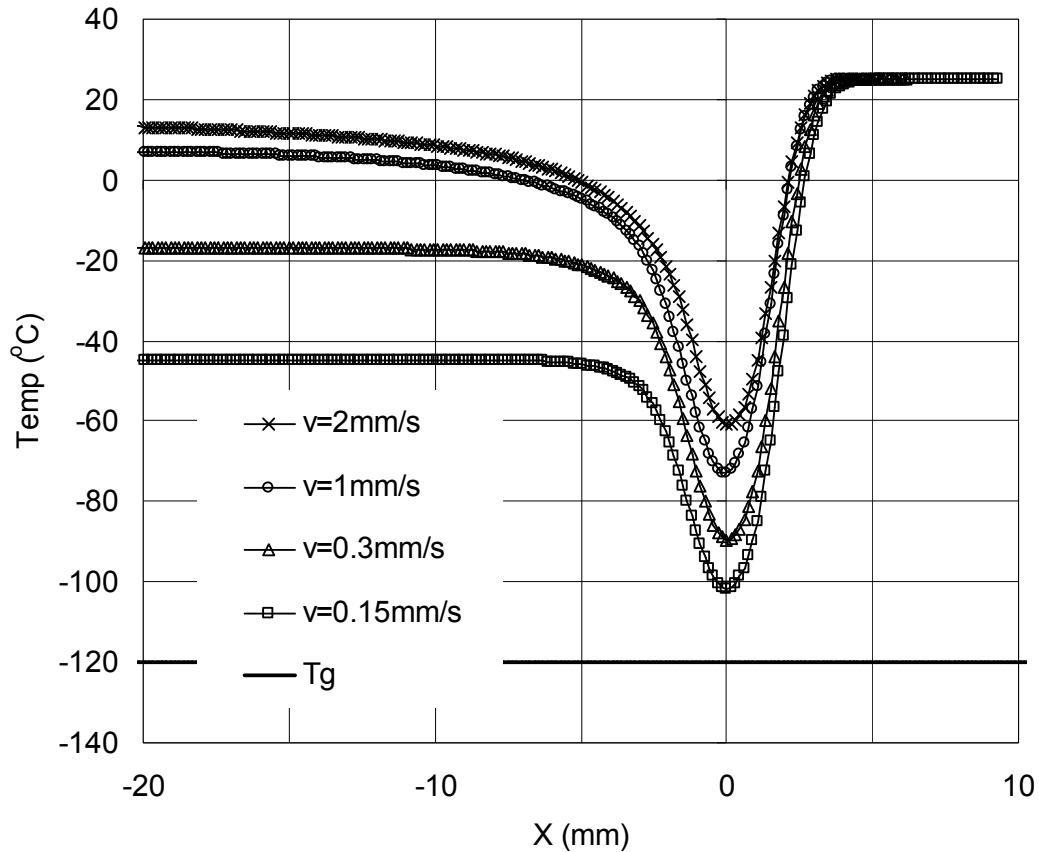


Figure 5.9 FE predicted temperature distributions in masked PDMS samples at the surface along the direction of motion (X -axis) and through the center of the mask opening ($Y=0$), for different scan speeds. The Gaussian convective heat transfer coefficient distribution was used. $X=0$ represents the center of the moving jet.

Comparison of Fig. 5.7 and 5.9 shows that, as expected, the circular cooling jet footprint over an unmasked target would produce lower temperatures at a given location than would the same jet on a masked sample simply because of the reduced lateral heat

transfer occurring under the masks. For example, at a scan speed of 1 mm/s, the cooling jet with a 6 mm diameter circular footprint over an unmasked PDMS target would create a temperature of -60 °C over a distance of 3.15 mm, compared with approximately 1.8 mm for the rectangular heat sink.

5.3 Surface Evolution in CAJM

5.3.1 *Case I: Model without Thermal Strain*

The surface evolution model, originally developed for brittle materials, relates the instantaneous surface slope to the local erosion rate through the normal velocity component [21, 110]. In previous papers, the model was modified and surface evolution equations were obtained that quite accurately predict the machined profile evolution in masked and unmasked micro-channels in both ductile and brittle erosive systems [11, 12, 100, 111]. For example, in Ref. [11] it was demonstrated that the model predictions of profile shape and machined channel depth were in very good agreement (less than 10% error) with the predicted results for various ductile polymers.

It has also previously been observed that channels machined in cryogenically cooled PDMS have steeper side walls and a flatter central region (Fig. 4.13) than channels of similar depth and width machined in a brittle material such as glass [100]. Such a channel shape, also seen in the AJM of ductile polymers such as PMMA [11] and

polycarbonate [12] at room temperature, is characteristic of ductile erosive systems. Therefore, the cooled PDMS in the present work was also assumed to erode in a ductile manner, and the appropriate two-dimensional surface evolution model is [11]:

$$Z_{,t}^* = \left(\gamma^*(Y^*) \sqrt{1 + Z_{,Y^*}^{*2}} \right) g(\alpha) \quad (5.6)$$

where $\gamma^*(Y^*)$ is the ‘erosive efficacy’, a non-dimensional, normalized polynomial function obtained from the fit of the first-pass erosion profile, which describes the net erosive effect of the velocity and particle mass flux distributions through the mask opening.

$Z^* = \frac{Z}{W}$, $Y^* = \frac{Y}{W}$, $t^* = \frac{t}{K_t}$, are the non-dimensional depth, channel width (Fig. 5.10)

and time, respectively. $Z_{,t}^*$ and $Z_{,Y^*}^*$ are the partial derivatives of the depth Z with respect to the coordinate Y , and time t , respectively. A time constant (K_t) was defined as the time required to propagate the surface at $X=0$ over a characteristic length (L) such that

$$K_t = \frac{L\rho_s}{C[v(0)]^k \phi(0)} \quad [110] \text{ where } \rho_s \text{ is the density of the substrate, } C \text{ is constant, } k \text{ is the}$$

velocity exponent, and $v(0)$ and $\phi(0)$ are the velocity and the particle flux at the center of the erosive jet.

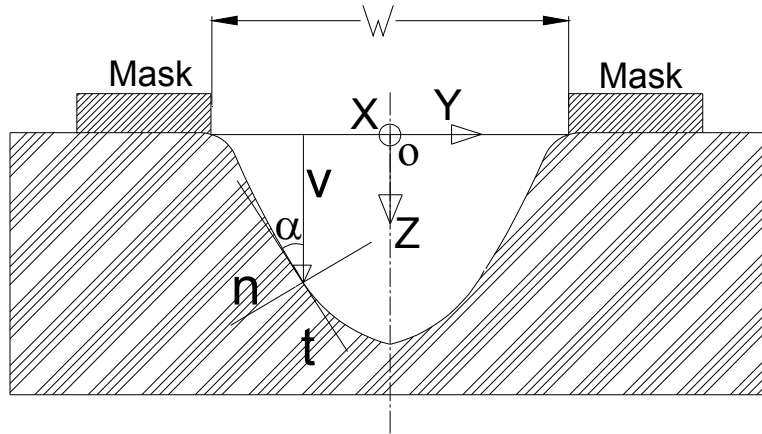


Figure 5.10 Coordinates for channel cross-sectional profiles. α is the angle between the Z-component of the particle velocity vector, v , and the tangent to the channel surface in the Z-Y plane.

The characteristic length for masked channels was taken to be the mask opening width W . The function $\gamma^*(Y^*)$ was normalized by dividing it by its value at $Y=0$ (channel midpoint). The function $g(\alpha)$ describes the dependence of erosion rate on impact angle, and for ductile erosion it was shown in [11, 12] that the relationship developed by Oka et al. [27, 34, 39] is appropriate:

$$g(\alpha) = (\sin \alpha)^{n_1} \left(\frac{k_2 - \sin \alpha}{k_2 - 1} \right)^{n_2} \quad (5.7)$$

where the constants n_1 , n_2 and k_2 must be determined experimentally from a fit to the measured normalized erosion rate of PDMS. In this work, $n_1=2.31$, $n_2=1$ and $k_2=10$ were estimated from previous measurements on PDMS under cryogenic conditions, i.e. $T= -150^\circ\text{C}$ (Section 4.1). Although Eq. (5.6) accurately predicts erosion and the shape of machined channels in isothermal applications, it does not account for the possible effects of thermal distortion that will occur in CAJM. Therefore, the objective of the modeling

described in this section was to investigate the influence of thermal distortion in the PDMS target on the accuracy of the predicted shape and size of machined channels.

It is appropriate to use the first-pass profile obtained at room temperature to determine $\gamma^*(Y^*)$ when the micro-machining is carried out at room temperature. However, in the case of CAJM the surface being machined is thermally strained due to the cryogenic jet, and thus the instantaneous profile during machining is different from the final profile at room temperature. Figure 5.11 compares the measured and predicted CAJM micro-channel profiles at room temperature machined under the conditions described in Section 5.1 using the first pass profile obtained at room temperature (Case I) to obtain $\gamma^*(Y^*)$ in Eq. (5.6). There is only fair agreement between the predicted and measured profiles, because $\gamma^*(Y^*)$ in this case was not derived from a first-pass profile at cryogenic temperatures, but rather was measured at room temperature. Over most of the cross-section, the model underestimated the depth of erosion. As seen in the next Section the depth underestimation was attributable to the neglect of thermal distortion in the target.

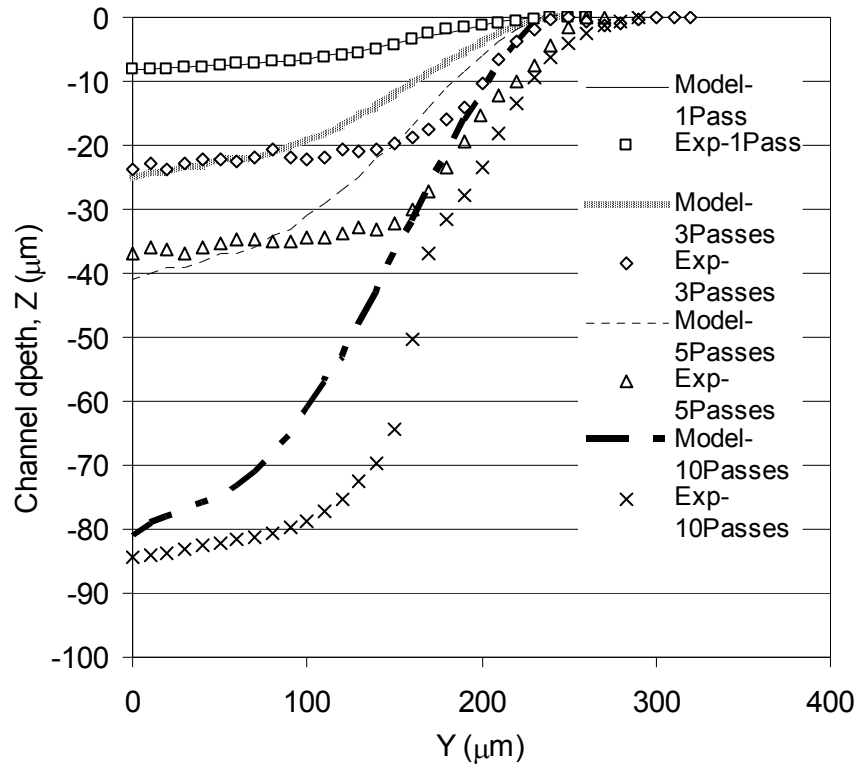


Figure 5.11 Case I: Measured and predicted micro-channel profiles for CAJM of PDMS. Predictions based on the measured first pass profile at room temperature to obtain $\gamma'(Y^*)$. CAJM conditions: slot nozzle (0.3 mm x 3.8 mm), 0.5 mm/s scan speed.

5.3.2 Case II: Model Including Thermal Strain

The deformation induced by thermal strains while performing CAJM was modeled using a coupled thermal/structural finite element (FE) analysis (ANSYS[®] 11). Thermal plane 77, 8-node quadrilateral solid elements were used for the thermal analysis, and plane 183 elements for the structural analysis (Fig. 5.12). Since the PDMS sample was clamped tightly by the steel masks bounding the channel on the eroded surface, the

model was fully constrained along the bottom and the sides; i.e. all displacements were set to zero on these surfaces.

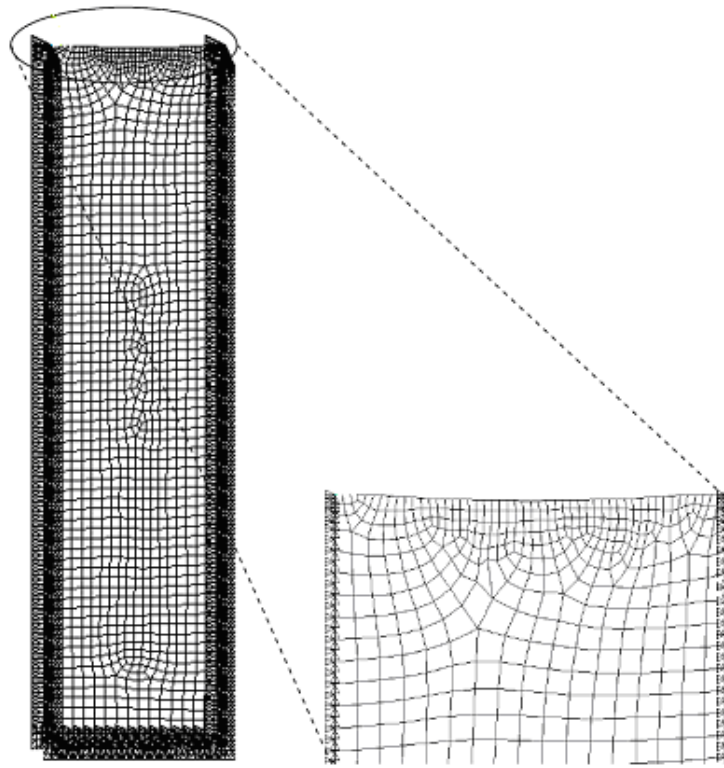


Figure 5.12 Two-dimensional finite element mesh of the cold PDMS profile between the masks after the first pass under the LN₂ cooled jet. Model width was 500 μ m and height was 4 mm.

The first-pass profile machined with the cold jet, but measured at room temperature, was reproduced in the FE model (Fig. 5.12). This surface profile was then distorted to the shape it had during the actual machining by applying a temperature of -150°C to the machined face and 25 °C to the back of the sample. Because the mechanical properties of PMDS at room and cryogenic temperatures were not accurately known, the sensitivity of the results to these properties was assessed by running the model at two temperatures. Room temperature properties were: thermal conductivity

$\kappa=0.15 \text{ Wm}^{-1}\text{K}^{-1}$, Young's modulus $E=615 \text{ kPa}$, and Poisson ratio $\nu=0.49$ [97]. Under cryogenic conditions, the value of Young's modulus for styrene-butadiene rubber (a material with similar E and ν to PDMS) is twice that at room temperature and the Poisson ratio should decrease [112-114]. Therefore, the cryogenic values for PDMS were estimated to be $E=1,230 \text{ kPa}$ and $\nu=0.40$. The coefficient of linear thermal expansion (α_l) was measured on the PDMS sample before and immediately after immersion in LN_2 , yielding an average value of $3.96 \times 10^{-4} \text{ K}^{-1}$ (4 measurements, standard deviation= $2.15 \times 10^{-5} \text{ K}^{-1}$), which was fairly close to the literature value $3.1 \times 10^{-4} \text{ K}^{-1}$ [115].

A comparison of the first-pass profiles reproduced in the FE model using these two sets of E and ν showed insignificant differences (maximum difference = $0.004 \text{ }\mu\text{m}$) in their profiles, indicating that the thermal distortion, and thus the predicted profiles were relatively insensitive to the variations of these properties with temperature over realistic ranges used in CAJM. The distorted (low temperature) profile was then used to fit to $\gamma^*(Y^*)$ and the model given by Eq. (5.6) was solved to obtain the evolving surface profiles after subsequent machining passes with the LN_2 cooled abrasive jet. To obtain the final room-temperature channel profile shape after multiple low-temperature passes, the FE model was finally run with all surfaces set to $25 \text{ }^\circ\text{C}$. Figure 5.13 compares these Case II channel profile predictions with the measured profiles.

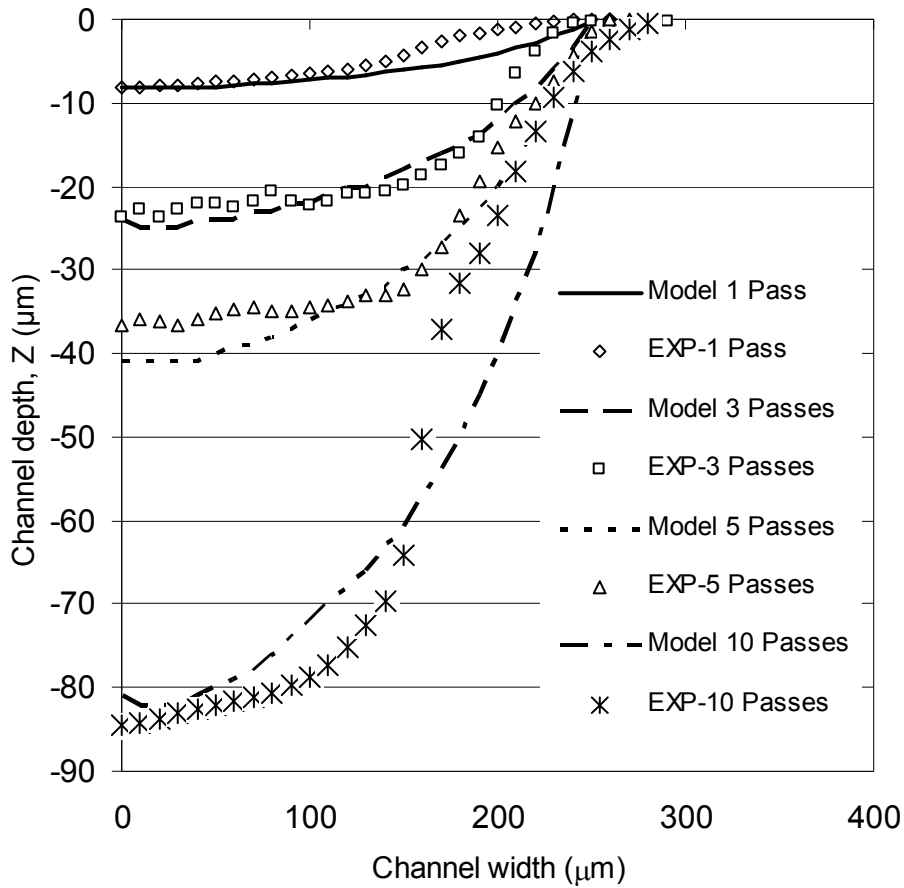


Figure 5.13 Case II: Measured and predicted surface profiles solved using the cold profile of the first pass $\gamma^*(Y^*)$. $E=615$ kPa, $\nu=0.49$, CAJM conditions: slot nozzle (0.3 mm x 3.8 mm), 0.5 mm/s scan speed.

Comparing Figs. 5.11 and 5.13, a significantly better agreement between the model predictions and the measured profiles was seen when these two thermal corrections were made (Fig. 5.13); namely, the first-pass profile (measured at room temperature) was adjusted to its cold shape, and the predicted final cold profiles were distorted to mimic their warming back to room temperature where they were measured. Table 5.2 shows that a better fit to the data was obtained for case II; i.e. when the thermal

effects were taken into account, the root-mean-square difference between the model and the experimental data points was smaller.

Table 5-2 Comparison of root-mean-square errors of the predicted channel profiles for Case I (Fig. 5.11, no thermal strain) and Case II (Fig. 5.13, thermal strain) models.

# of passes	Model (Case I)	Model (Case II)
	Root Mean Square Error (μm)	Root Mean Square Error (μm)
3	4.7	2.0
5	7.4	3.3
10	14.1	9.2

Table 5.3 compares predictions of the channel depth for both cases with the experimentally measured values at the center of the channel ($Y=0$), and approximately half the distance to the mask edge ($Y=150 \mu\text{m}$). Especially at $Y=150 \mu\text{m}$, the Case II model provides a much better prediction of the depth than the Case I model, which underestimates the depth over most of the cross-section.

Table 5-3 Comparison of channel depths (Z) predicted ignoring thermal strain (Case I, Fig. 5.11), and considering thermal strain (Case II, Fig. 5.13) with experimentally measured depths at channel center (Y=0) and at Y=150 μm .

Y (μm)	Exp.			Model (Case I)			Model (Case II)		
	Channel depth (Z - μm)			Channel depth (Z - μm)			Channel depth (Z - μm)		
	Number of passes			Number of passes			Number of passes		
	3	5	10	3	5	10	3	5	10
0	-24	-37	-84	-25	-41	-81	-24	-41	-81
150	-20	-32	-64	-12	-20	-37	-18	-30	-61

5.3.3 CAJM of Other Features

Section 5.3.2 described the effects of thermal distortion in the micro-machining of masked channels in which the target was firmly fixed in the masking device and only exposed to the jet through the 500 μm mask opening. However, in the case of machining an arbitrary shape, for example, a planar area as described in [116], the substrate is unmasked. Therefore, only the ends are constrained by clamps while other points in the sample can distort upward and laterally (Fig. 5.14). This Section examines the effects of thermal distortion in this situation.

In the past, two procedures have been developed to perform such machining: (i) the oscillating abrasive jet method, which is best for machining to a single depth [117], and (ii) the multiple pass method, which is more general and can produce eroded areas having arbitrarily varying depths [116]. In the second method, the final eroded surface is

the result of a number of overlapping nozzle passes, each of them having a unique stand-off distance, offset from the previous pass, and scan speed [116]. To predict the surface evolution due to these overlapping passes, the machined surface profile from the previous pass is used as the initial geometry in the model for the subsequent pass. In the case of CAJM, however, the initial surface profile measured at room temperature must be converted to the thermally deformed surface profile, to be used as initial surface condition for the subsequent pass at low temperature. Then, in a procedure similar to that adopted in Section 5.3.2, the low-temperature final shape must be distorted back to its condition at room temperature.

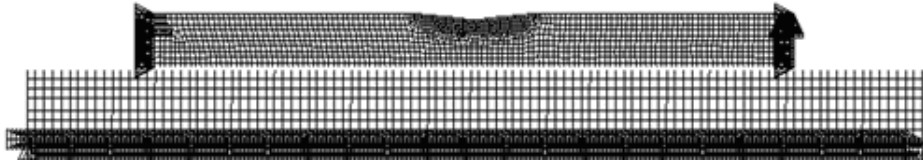


Figure 5.14 Mesh of a PDMS sample 5 cm long x 4 mm thick constrained at the ends.

The thermal deformation of the substrate subjected to CAJM for one pass was simulated using ANSYS[®] 11. The same thermal boundaries as described in Section 5.3.2 were used. Sliding between the PDMS and the supporting steel plate was allowed with zero friction coefficient. The mechanical properties of the PDMS at room temperature were used as described in Section 5.3.2.

In Fig. 5.15, the solid line shows the surface profile measured at room temperature after 1 micro-machining pass under the cold jet. The same profile at the low temperature created by the cryogenic jet is shown by the dashed line, and it is this profile that should be used to determine the micro-machining conditions (stand-off distance, scan speed, nozzle offset from the origin) for the subsequent passes when machining arbitrary shapes using multiple CAJM passes using the methodology presented in [116].

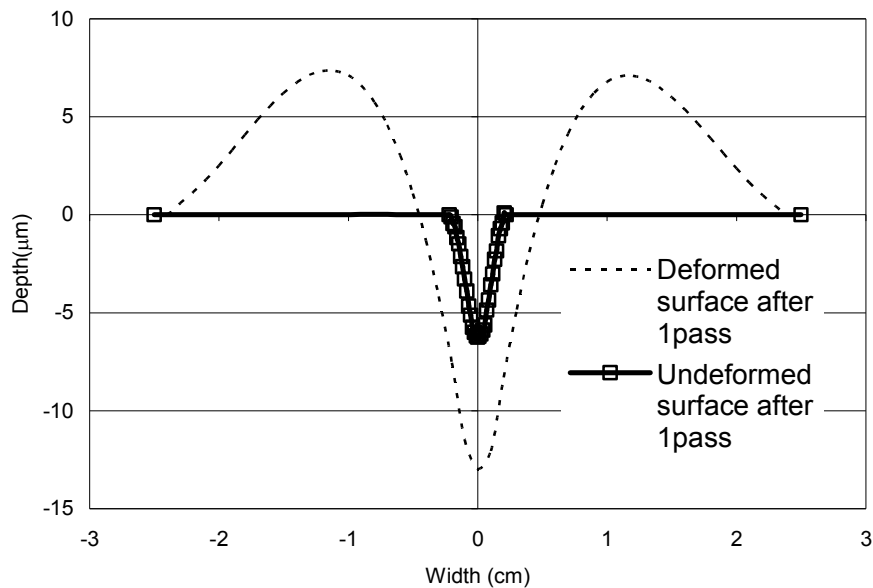


Figure 5.15 Surface profiles of PDMS after one cryogenic machining pass at two temperatures: Solid line shows profile measured at room temperature. Dashed line shows the predicted shape of the same profile after having been thermally deformed by cooling to -150 °C.

5.4 Chapter Summary

The most important findings of this chapter can be summarized as follows:

- (a) For the utilized experimental setup, the time to cool a chip removed by a single particle was 0.7 ms which is much shorter than the estimated average time between impacts ($t_i=7.7$ ms). The comparison shows that thermal front advanced much faster than the material removal rate, enabling the cooling of a PDMS substrate during the CAJM of holes to be modeled analytically assuming a stationary heat transfer boundary.
- (b) The temperature at the center of the jet obtained using FEA compared reasonably well with the measured temperatures at the center of the channel with an approximately 20% error at typical scan speeds used in AJM.
- (c) The FE model illustrated the asymmetric nature of the cooling. Much more cooling occurred towards the trailing edge and there was a large temperature gradient in the direction of the leading edge. As expected, the target temperature decreased with decreasing scan speed.
- (d) The accuracy of the prediction of evolving surface profiles can be improved significantly if a finite element model is used to distort the first-pass profile, measured at room temperature, to its shape at the low-temperatures seen in CAJM and this profile is used to predict evolving surface profiles.

6 Conditions Leading to Embedding of Angular and Spherical Particles during the Solid Particle Erosion of Polymers

The literature review of Section 2.5 and results of Chapter 4 showed that embedding of erodent particles is observed during abrasive jet micro-machining (AJM) of polymers and elastomers such as PDMS (Section 4.3.1.2), and that embedded particles may shield the surface from subsequent impacts resulting in a reduced erosion rate. The performance of AJM fabricated devices such as micro-fluidic chips could be affected due to the presence of embedded particles. While particle embedment has been identified in a variety of solid particle erosion processes, the criteria leading to embedment have not yet been established. In this Chapter, conditions under which particle embedding occurs were examined for both angular and spherical particles.

6.1 Experiments

6.1.1 Erodent and Target Materials

Two types of angular garnet particles were used: 136 μm nominal diameter (Mohwak Garnet Inc., Wahnapiatae, ON, Canada), and 103 μm nominal diameter, obtained by sieving the 136 μm particles using an ASTM standard procedure [118]. Three target materials were used: 1.6 mm thick PMMA sheet (acrylic FF sheet, CYRO

Industries, Rockaway, NJ, USA), 3 mm thick LDPE sheet, and 3 mm thick ABS sheet (both from McMaster-Carr, 200 Aurora Industrial Pkwy., Aurora, OH, USA).

The shapes of the garnet particles were characterized in three ways: (i) An optical microscope was used to measure the dimensions of particles adhering to an adhesive tape in two perpendicular planes; when viewed from above and from the side. The ratio of the average dimensions of 61 measurements taken in these two planes was found to be 0.86. (ii) Stereo scanning electron microscopy (MeX™ software, Alicona Imaging GmbH) was used to reconstruct the 3D geometry of the particles (Fig. 6.1a). (iii) SEM images of the particles were obtained at an inclination of 75° to the mounting plane (Fig. 6.1b).

Figure 6.1 shows that the garnet particles were blocky in shape, i.e. had roughly the same dimensions in all directions and, therefore, could be represented by a two-dimensional rhomboid shape (Section 6.2). It is noted that the scale on Fig. 6.1b is slightly distorted because the image was taken with the holder inclined.

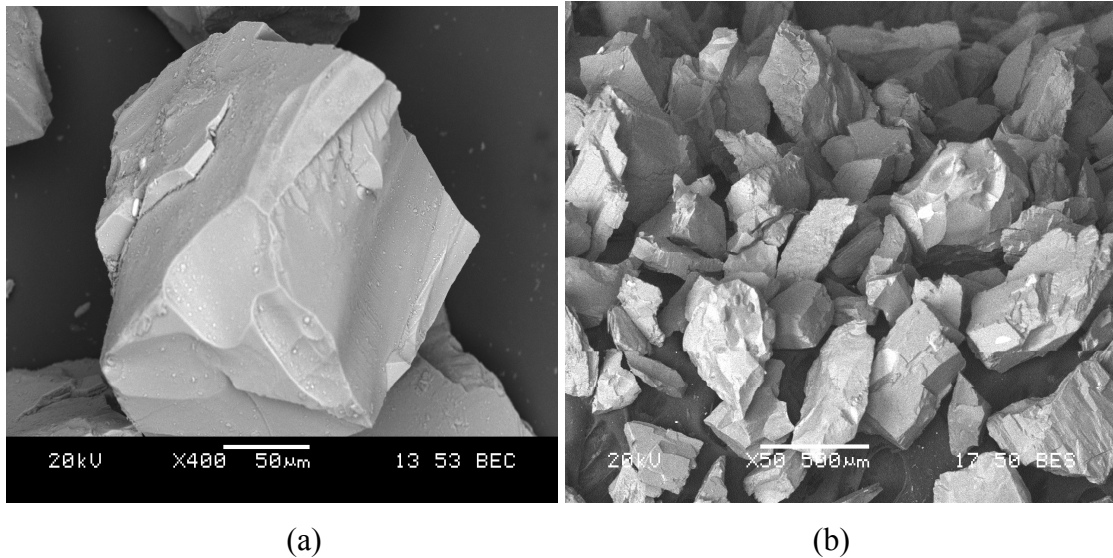


Figure 6.1 Images of 136 μm garnet particles using: (a) 3D SEM stereo reconstruction, (b) SEM viewed at 75° from the plane of the holder.

In addition to the above experiments, aspect ratios (the ratio of the shortest axis to the longest axis) of A_2O_3 nominally 100 μm and 150 μm and garnet 136 μm and 103 μm were determined using both the optical particle analyser and shadowgraphy. The results of the shadowgraphic measurements are given in Section 6.2.1. The rest of the results are given in Appendix G.

6.1.2 Particle Impact Experiments

The experiments were performed with a micro-abrasive blaster (Accuflo, Comco Inc., Burbank, CA, USA) with a specially built mixing device to prevent particle bed compaction and enhance the consistency of the mass flow rate [79]. Discrete, non-overlapping impact sites were obtained by directing 0.1 s bursts of particles at the target materials using a solenoid-actuated shutter with an electronic timer in front of the 1.5 mm

inner diameter round nozzle. The air pressure was 200 kPa, the stand-off distance was 20 mm, and the impact angles were 90°, 60° and 30° ($\pm 1^\circ$) from the target surface. The average mass flow rates of the 136 μm and 103 μm nominal diameter garnet particles were 2.74 g/min (3 measurements, standard deviation 0.04 g/min) and 3.41 g/min (3 measurements, standard deviation 0.17 g/min).

The distributions of the particle velocity, and the particle size and shape (area and aspect ratio) were measured (Section 3.4) within the jets using a laser shadowgraphy system (LaVision GmbH, Goettingen, Germany) described in detail in [119]. The shadowgraphy measured average aspect ratio (0.66) was in good agreement (12% difference) with the average aspect ratio measured using the optical microscope (0.75). It is noted that these aspect ratios were determined from dimensions obtained in the same plane. The measured aspect ratios showed that garnet particles were the blockiest among the considered particles (i.e. Al_2O_3). The measured average velocities at the center of the jet for the 136 and 103 μm particles at the 20 mm standoff distance were 62 m/s and 91 m/s, which agreed very well with the corresponding values of 61 m/s and 84 m/s obtained using the mathematical model of Li et al. [120], with the modification introduced by Dehnadfar et al. [119].

The average number of particles that were embedded during the 0.1 s exposure under the various impact conditions were counted in three samples of each polymer (LDPE, ABS, and PMMA). The examined impact area was 5.4 mm^2 centered at the axis

of the jet where the velocity was well-defined (total blast area was 8 mm^2). Embedded particles were identified and counted using the SEM/EDX technique (Figs. 6.2(a) and 6.2(b)) described in (Section 7.1.4) applied to 70 sub-areas each having dimensions $320 \times 240 \text{ }\mu\text{m}$.

Figures 6.2(c) and 6.2(d) show examples of particles embedded in ABS and PMMA after blasting at a 90° impact angle. The total number of particles that struck the central 5.4 mm^2 impact area was estimated from the known particle mass flux Weibull distribution for this nozzle which had a focus coefficient, $\beta=10.2$ [111, 121]. Assuming spherical particles with average diameter and density $\rho=4,000 \text{ kgm}^{-3}$, the number that struck the measured area was 1,570 of the $136 \text{ }\mu\text{m}$ particles, and 2,760 of the $103 \text{ }\mu\text{m}$ particles. A very similar estimate was obtained by assuming a distribution of spherical particles that matched the measured size distributions of these two media.

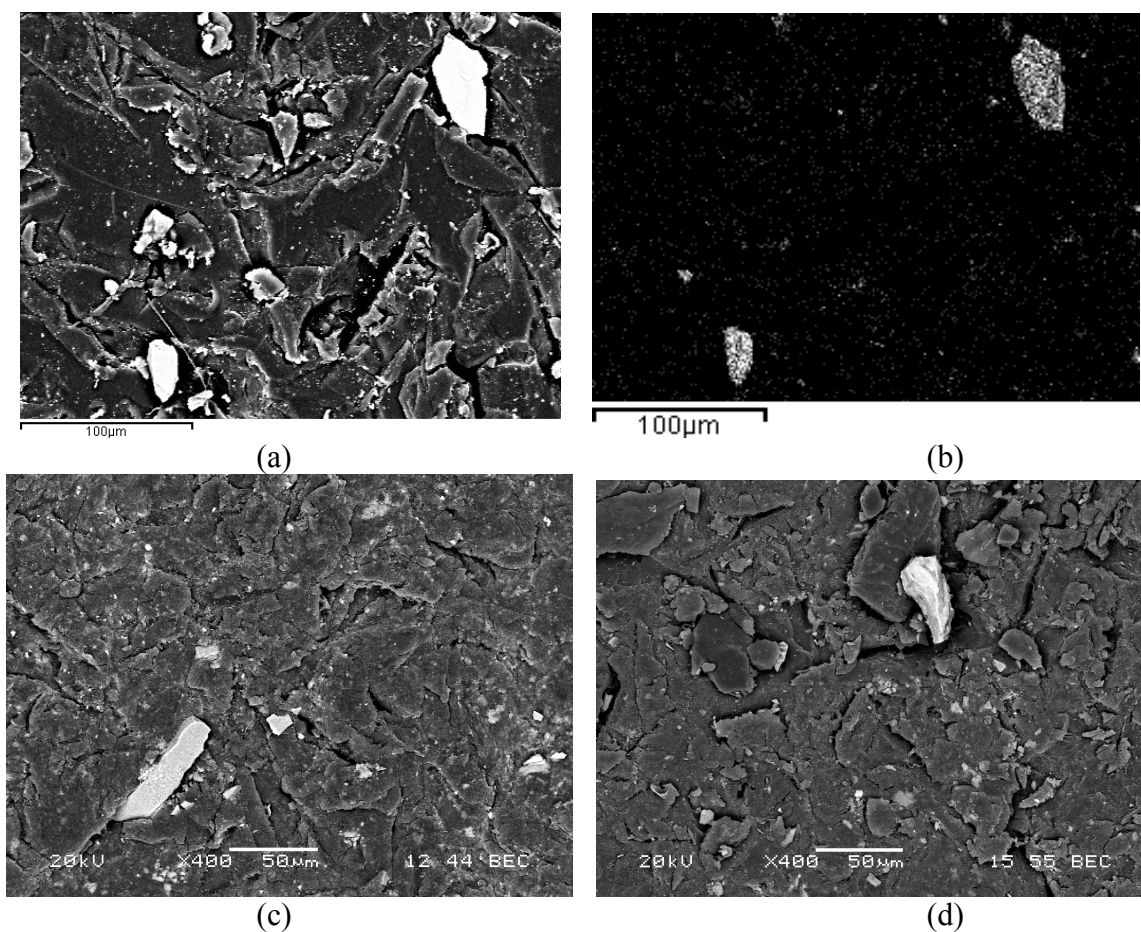


Figure 6.2 SEM micrographs of embedded particles incident to surface at 90° in: (a) LDPE, (c) ABS, and (d) PMMA. (b) shows EDX map of Fe confirming presence of embedded particles in LDPE.

6.1.3 Dynamic Hardness Measurements

The dynamic hardness of the three target materials was measured by launching steel spherical particles (50 μm nominal diameter chronital, Vulkan-INOX, Germany) and measuring the resulting crater dimensions. The average diameter of 1,230 particles was measured as 70 μm (± 18 standard deviation) using an optical particle size analyzer

described in Section 3.4. The same experimental procedure described in Section 6.1.2 was used, except that all particles were blocked except those passing through a 1 mm diameter hole in a steel plate centered on the jet axis 10 mm from the nozzle. The setup ensured that only particles near the center of the jet struck the surface so that a computed average center-line jet velocity of 62 m/s could be used in the calculation of the dynamic hardness [120]. The crater diameters at 10 different sites were measured with an optical microscope for each polymer, and the average value (Table 6.1) was used to calculate the dynamic hardness (p_d) as [122-124]:

$$p_d = \frac{0.5mv_j^2}{V} \quad (6.1)$$

where m is the mass of the particle (v_j) is the average jet centerline velocity and V is the volume of the crater given by

$$V = \left(\frac{\pi}{6}\right) \left(R - \sqrt{R^2 - r^2}\right) \left(3r^2 + \left(R - \sqrt{R^2 - r^2}\right)^2\right) \quad (6.2)$$

where R is the particle radius and r is the radius of the impact crater.

Table 6-1 Dynamic hardness values of target polymers

Polymer	Measured average crater diameter (μm)	Standard deviation of 10 measurements (μm)	Dynamic Hardness (MPa)
PMMA	36.5	5.8	970
ABS	41.7	4.8	550
LDPE	61.3	5.6	89.5

6.2 Models for Particle Embedding

6.2.1 *Model for Embedding of Angular Particles*

The rigid-plastic impact model developed by Papini and Spelt [68, 69] was used to determine the trajectories of particles as they ploughed craters into the target, and thus gain insight into the conditions under which particle embedding occurred. The model assumes a non-deforming particle and a fully-plastic target material which resists the indentation with a contact force equal to the constant dynamic hardness multiplied by the instantaneous contact area. The elastic component of the target response is assumed to be negligible. The resulting equations of motion of the particles as they plough or cut through the target must be integrated numerically in time steps because the contact area, and thus the magnitude and direction of the contact force, changes throughout the impact. As shown in Fig. 6.1, the particles were blocky, rather than flaky so that regardless of orientation, their impacts are likely to occur on an edge rather than on a flat side. Therefore, the garnet particles were approximated as a collection of idealized rhomboid shaped particles (Fig. 6.3) having the same aspect ratio, area and velocity distributions as the actual particles. The implementation of the rigid-plastic model in a MathCad (PTC, Needham, MA, USA) computer program was described in detail in [69], where it was used to predict the sizes and shapes of the craters formed by indenting particles, as well as the trajectories of the particles. The required input parameters were: particle

angularity (A), incident angle (α), orientation angle (θ), side length (h) and incident velocity (V_i), as shown in Fig. 6.3 [68, 69].

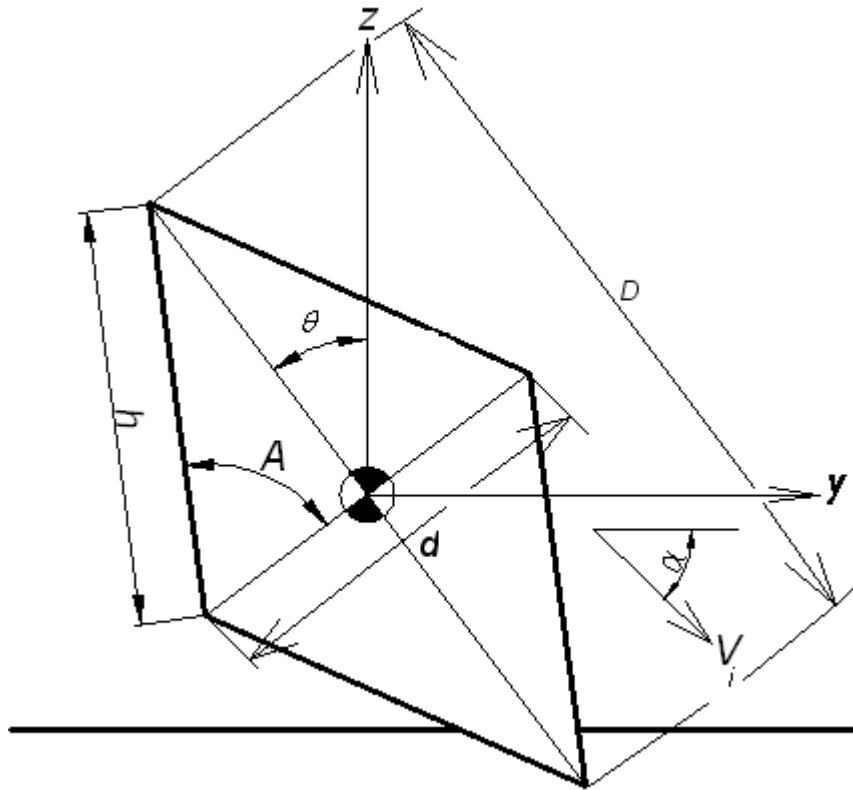


Figure 6.3 Geometry and orientation of indenting particles: θ - initial particle orientation; α - impact angle; V_i - initial velocity; A - particle angularity; h - particle side length.

Figure 6.4 shows the measured log-normal particle size distributions (equivalent circular diameter) of the 136 μm and 103 μm garnet particles while Fig. 6.5 shows the measured log-normal aspect ratio (d/D) distributions. The data were from the shadowgraphic measurements of 25,460 136 μm particles and 39,990 103 μm particles. The average particle diameters were 136 μm (standard deviation $\pm 76 \mu\text{m}$) and 103 μm (standard deviation ± 31), respectively. The average angularities of the two sizes of particles were

very similar (Fig. 6.5): $A_{avg}=33^\circ$ for 136 μm garnet particles and $A_{avg}=34^\circ$ for the 103 μm garnet particles. Figure 6.6 shows the velocity distributions of the 136 μm and 103 μm garnet particles. Fig. 6.7 illustrates the approximation of the particles as rhomboids as they exit the nozzle during the shadowgraphic measurements.

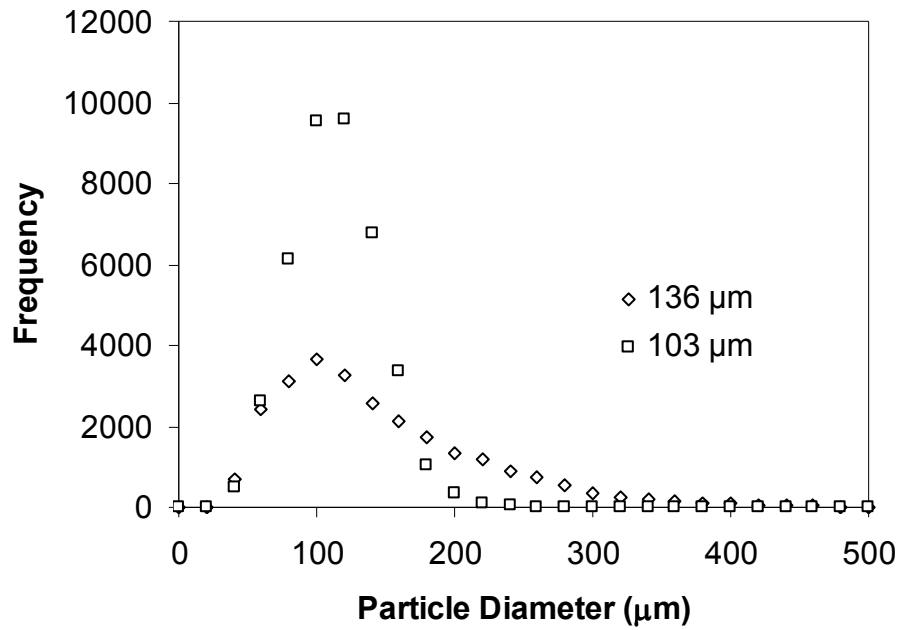


Figure 6.4 Shadowgraphy measurements of particle size distribution (equivalent diameter) for 136 μm and 103 μm nominal size garnet particles.

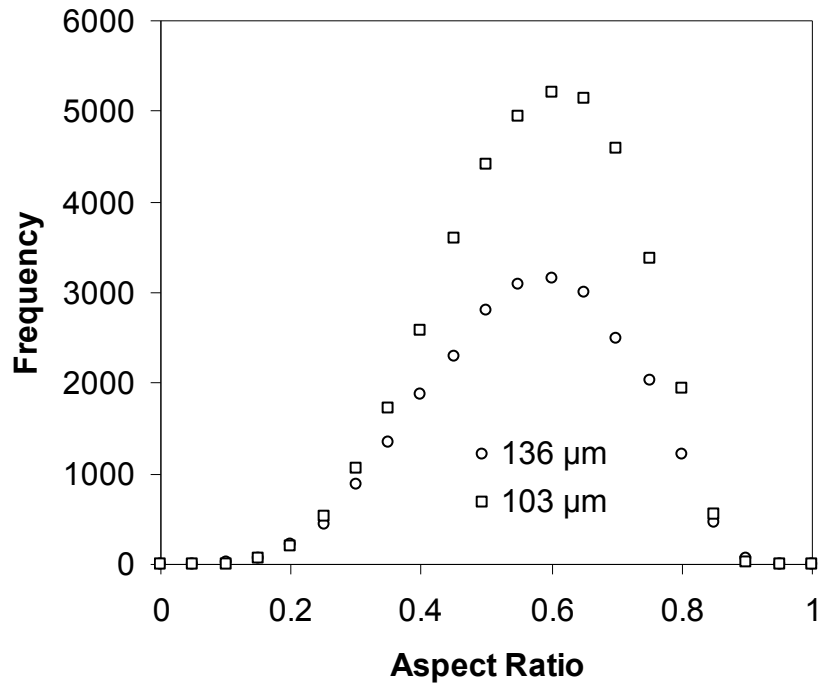


Figure 6.5 Shadowgraphy measurements of aspect ratio (d/D , Fig. 6.3) of 136 μm and 103 μm nominal size garnet particles.

The quantities, d and D , were extracted from the measured particle aspect ratios and circular areas, and the model parameters h and A were calculated as:

$$h = \sqrt{(0.5D)^2 + (0.5d)^2} \quad \text{and} \quad A = \tan^{-1}\left(\frac{D}{d}\right).$$

The program, written in Matlab R2010 (Mathworks), assigned a random orientation (θ) in the range -90° - 90° to each particle from the shadowgraphic data sets for the 136 μm and 103 μm particles. These data were then arranged in a spreadsheet with columns containing the values of A , h , θ and v for each measured particle, from which the launch algorithm selected rows randomly to represent particles that would strike the surface. These values (A , h , θ and v) were then used as inputs in the rigid plastic mathcad model developed by Papini and Spelt [69].

The particle thickness was arbitrarily assumed to be 100 μm in all cases, since the model is two-dimensional with particle mass, moment of inertia, and the volume of the crater expressed on a per-unit-thickness basis [69]. Details of the Matlab program and examples of constructed rhomboid particles are given in the Appendix I.

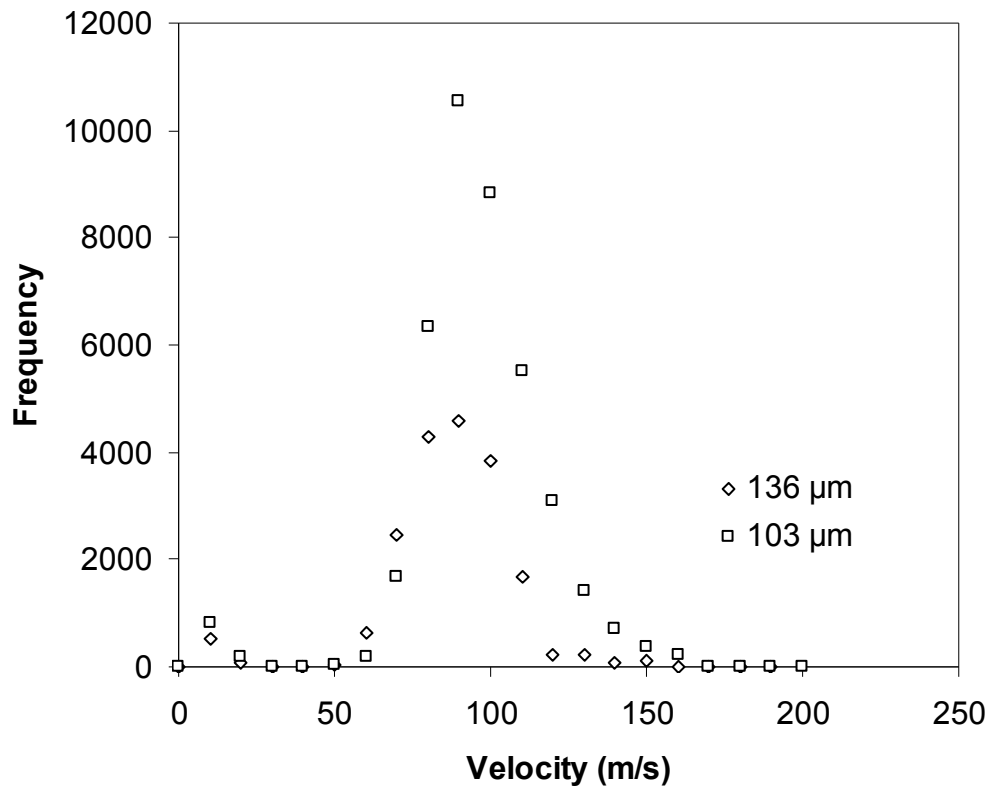


Figure 6.6 Shadowgraphy measurements of velocity distribution of 136 μm 103 μm nominal size garnet particles.

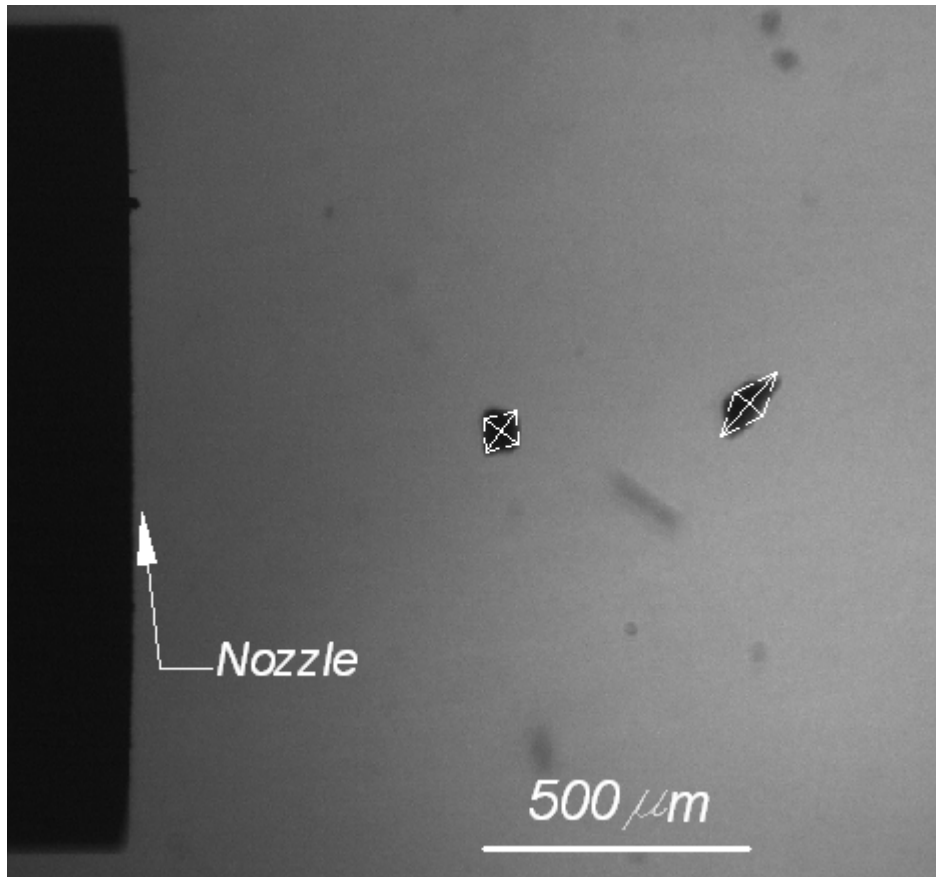


Figure 6.7 Particles in flight as they exit the nozzle during shadowgraphic measurement.

During the modeling of particle-target interaction, the time step required for model convergence was determined by decreasing it until the difference between successive runs of the model was around 1%. Depending on the input parameters used (h and A) and the type of target material, the required time steps varied between $0.001 \mu\text{s}$ and $0.003 \mu\text{s}$. Similar steps were followed in [69].

6.2.2 Angular Particle Embedding Criteria-Analysis

It was hypothesized that angular particles would embed if two conditions were met during impact:

- (I) Particles do not lose contiguous contact with the target along both faces at any point during the incident portion of the impact (Fig. 6.8). A loss of contact between the particle and the target would greatly decrease the elastic clamping force that serves to retain a particle. The model of Section 6.2.1 was used to assess this criterion for a given impact. The coefficient of friction between the particle and the target does not influence the probability of a particle meeting condition I.
- (II) The elastic rebound force generated by the normal clamping pressure on the particle faces is smaller than the frictional force that tends to retain the particle (Fig. 6.8).

As will be shown below, Criterion II implies the existence of critical coefficient of static friction for a given particle-target system below which angular particles embed.

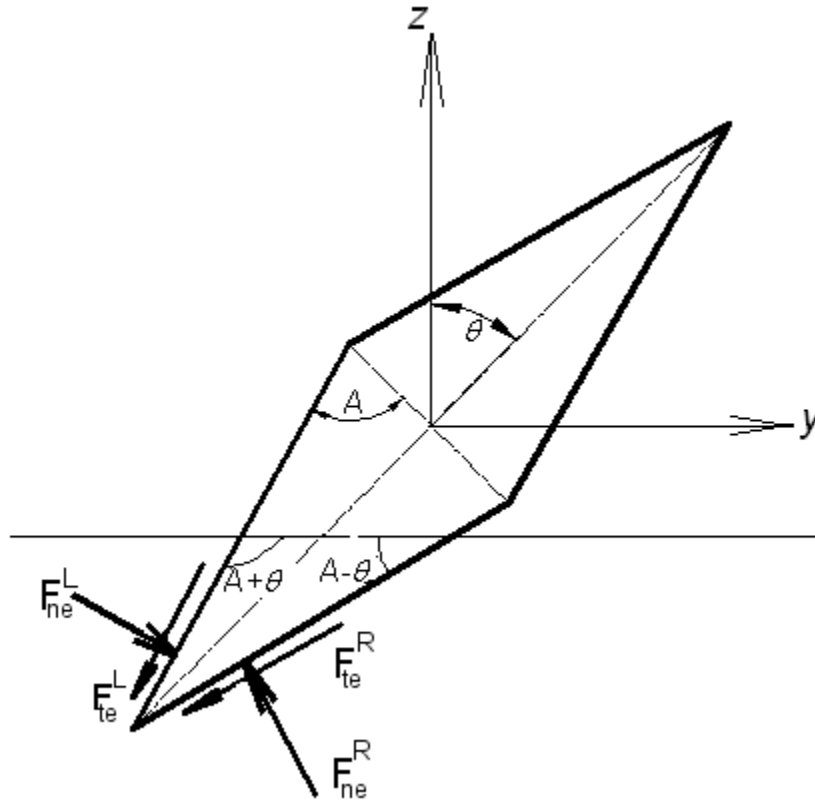


Figure 6.8 Forces acting on the left and right sides of an angular particle in full contact along both faces when it begins the rebound phase of contact. F_{ne}^L and F_{ne}^R are the elastic normal forces, F_{te}^L and F_{te}^R are the tangential elastic forces.

Equilibrium of the forces when the particle is essentially at rest and just beginning to rebound implies (Fig.6.8)

$$\sum F_y = 0 = F_{ne}^L \sin(\pi - A - \theta) - F_{te}^L \cos(\pi - A - \theta) - F_{ne}^R \sin(A - \theta) - F_{te}^R \cos(A - \theta) = 0 \quad (6.3)$$

$$\sum F_z = 0 = -F_{ne}^L \cos(\pi - A - \theta) - F_{te}^L \sin(\pi - A - \theta) - F_{te}^R \sin(A - \theta) + F_{ne}^R \sin(A - \theta) = 0 \quad (6.4)$$

Combining Eq. (6.3) and (6.4) shows that equilibrium requires that the ratio of tangential to normal elastic force (coefficient of friction required for equilibrium) is related to the particle angularity by:

$$\frac{F_{te}}{F_{ne}} = \frac{1}{\tan(A)} \quad (6.5)$$

Therefore, if the actual coefficient of static friction between the particle and the target (μ) is larger than that of Eq. (6.5), the particle will embed, and if it is less the particle will not be retained by the surrounding target material, but will be squeezed out by the elastic forces acting on its faces. Highly angular particles ($A \rightarrow 90^\circ$) can thus become embedded in materials with a smaller μ than particles that are more blocky in shape. Equation (6.5) shows that while the direction of the elastic forces may vary depending on the crater shapes formed by impacting particles launched at different impact angles, velocities and orientations, provided that criterion (I) is met, the tangential to normal elastic force ratio depends only on the particle angularity A (i.e. its sharpness). The higher the angularity (i.e. the sharper the particle), the lower the tangential to normal elastic force ratio, and thus the more likely that the particle remains embedded. The value of $\frac{F_{te}}{F_{ne}}$ can therefore be used together with experimental results to determine the embedding conditions; i.e. a particle would embed if $\frac{F_{te}}{F_{ne}} < \mu$. For impacts other than 90° , it is possible that a particle sticks on one side and slides on the other side; i.e. $\frac{F_{te}}{F_{ne}}$ may be less than μ on one side but not the other. In this case it was assumed that embedding would not occur if sliding was predicted on either of the sides.

6.2.3 Angular Particles Embedding Criteria: Comparison with Experimental Results

The embedding criteria presented in Section 6.2.2 were evaluated using experimental data for five particle-target systems: 136 μm garnet particles against three target materials: LDPE, a relatively soft target; PMMA, a relatively hard target; and ABS, a relatively tough target. The tests were repeated with 103 μm garnet particles for the LDPE and PMMA targets. The model was run for 1,570 particles, which was the number of 136 μm particles that impacted the examined target area in the experiments.

First, the rigid-plastic model from Section 6.2.1 was run to determine which of the modeled particles impacting at 90° fulfilled criterion I; i.e. maintained contiguous contact during the impact. In all cases, this number was greater than the number of embedded particles that were counted in the experiments. For example, the model predicted that 391 of the 1,570 launched 136 μm particles satisfied criterion I in PMMA at 90° (fraction embedding, $P=25\%$), whereas the measured P was 8.7%. This result suggested that the first embedding criterion (contiguous contact during impact) was necessary but not sufficient. Criterion II was then applied to the subset of model particles determined by criterion I to determine the coefficient of static friction (μ) required for the model to predict the observed fraction of embedded particles. The coefficient of static friction was obtained by adjusting the value of μ until the number of model particles satisfying

$\frac{F_{te}}{F_{ne}} < \mu$ equalled the measured number at $\alpha=90^\circ$ establishing the value of the coefficient

of static friction (μ) for the particle-target system. Once μ was established using the experimental data at 90° , it was assumed that μ was a property of the particle-target system, so that it could be then used in conjunction with criterion I to predict the number of embedded particles at other angles of attack. For example, for the $136\ \mu\text{m}$ garnet-PMMA system at 90° , the coefficient of friction was found to be $\mu=0.71$. Using this μ for $136\ \mu\text{m}$ garnet particles in PMMA, Table 2 shows that the fraction of predicted embedded particles meeting both criterion I and II at 60° and 30° in PMMA was in excellent agreement with the measured results ($\leq 0.2\%$ difference). For the $103\ \mu\text{m}$ garnet-LDPE system, the best fit to the 90° data gave $\mu=0.66$. Table 2 shows that with this μ the predicted fraction of embedded particles was also in good agreement with the measured results (maximum difference of 0.2% at 60°).

The effect of changing the particle size on the value of μ was examined using the impact data for the $103\ \mu\text{m}$ garnet particles on PMMA and LDPE targets. As expected, the determined μ values did not depend on particle size; less than 1.5% difference in μ for the two particle sizes against either the PMMA or LDPE.

As discussed previously, some data suggest that embedding is a function of particle size [63, 73]. To investigate the effect of particle size, the size distributions of the particles that were predicted to embed by the model were obtained for the $136\ \mu\text{m}$ garnet/PMMA system at 90° , 60° and 30° impact angles. In all cases, the size distributions of the model embedded particles obtained were similar to those of the

abrasive stream (Fig. 6.4) indicating that particle embedding was not a function of the particle size for the investigated particle/target systems. However, it is noted that the model and the present experiments involved discrete impacts without the possibility of subsequent impacts against already embedded particles. The apparent increase in particle embedding with increasing size observed in [63] may have been caused by the fragmentation of large embedded particles on subsequent impact or upon initial impact as suggested in [33].

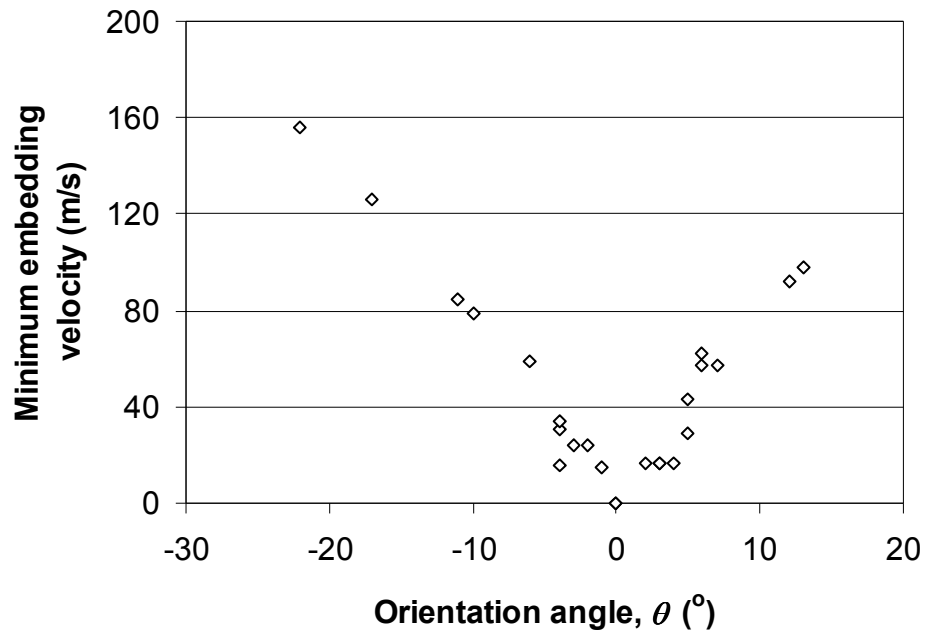
The uncertainty in the fraction of particles that became embedded (P) can be estimated using the binomial distribution [125]. For example, for PMMA at 60° the 95% confidence interval in the measured $P=0.081$ was ± 0.013 for $N=1,570$ launched particles (i.e. $\pm 16\%$). For the $103\ \mu\text{m}$ particles against LDPE at 60° , the model was run with $N=1,570$ particles resulting in an uncertainty of ± 0.015 on the fraction of embedding, $P=0.099$ (i.e. $\pm 15\%$).

Table 6-2 Comparison of the predicted fraction of embedded particles (Model P) with the experimentally measured results (Expt P). μ - coefficient of static friction value determined using comparison with experimental data at 90° then used to model P at 60° and 30° ; A - particle angularity; Diff - difference between experimentally measured and predicted fraction of embedded particles.

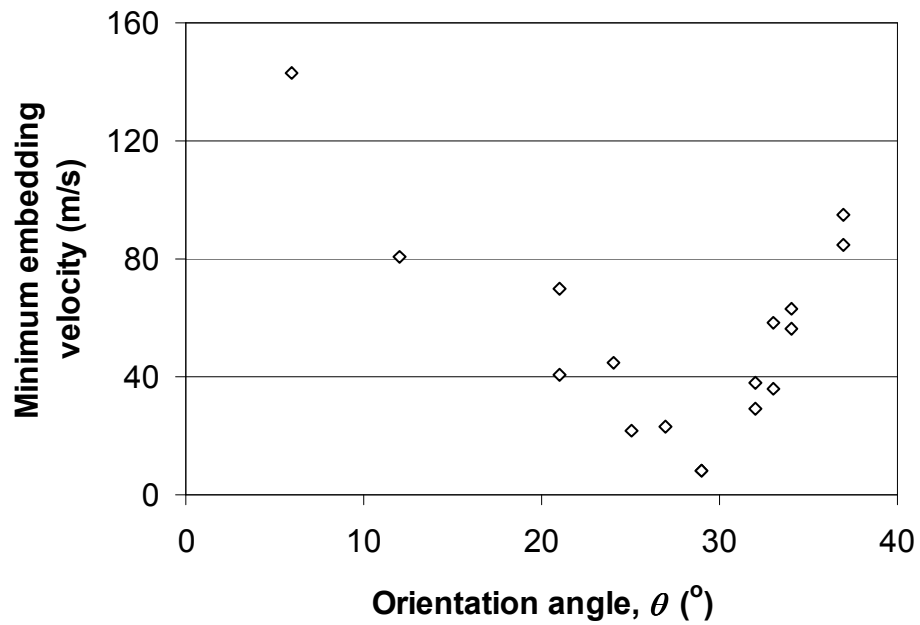
Particle size	Target Material	$\alpha=90^\circ$		$\alpha=60^\circ$				$\alpha=30^\circ$			
		Expt		Model P	Expt		Diff	Model P	Expt		Diff
		A ($^\circ$)	μ		Expt P	A ($^\circ$)			Expt P	A ($^\circ$)	
136 μm	PMMA	55	0.71	8.3%	8.1%	56	0.2%	4.1%	4.0%	55	0.1%
	LDPE	56	0.67	8.8%	8.7%	57	0.1%	4.5%	4.3%	57	0.2%
	ABS	54	0.72	7.3%	7.1%	55	0.2%	4.1%	4.0%	55	0.1%
103 μm	PMMA	54	0.72	9.4%	9.2%	55	0.2%	5.7%	5.6%	55	0.1%
	LDPE	56	0.66	9.9%	10%	56	0.1%	6.0%	6.0%	56	0.0%

From these results, it is possible to draw the following conclusions: (1) Provided that contiguous contact is maintained during impact, for a given particle-target system, if the static coefficient of friction is inferred at a given impact angle, then it is possible to estimate the number of embedded particles at other impact angles with good accuracy; (2) These values of the static coefficient of friction remain approximately the same for a given particle-target system, regardless of particle size and impact angle.

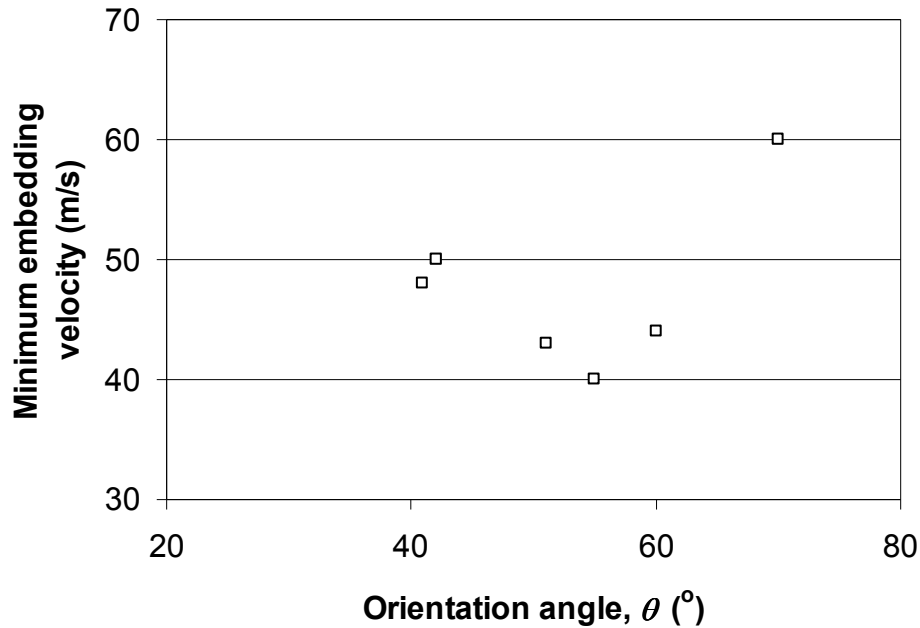
It is possible for a particle to embed with an arbitrary orientation arriving at any impact angle as long as it has sufficient velocity (kinetic energy). However, there is a minimum incident velocity below which embedding does not occur. Also, there is preferred incident orientation for the particle to embed. Figure 6.9 shows the minimum incident velocities and corresponding orientations that caused embedding in PMMA at the different impact angles. In creating Fig. 6.9, the rigid-plastic model was run for a given impact angle with random particle sizes (h), angularities (A) and orientations (θ), and only those particles which satisfied both embedding criteria were recorded.



(a) $\alpha = 90^\circ$



(b) $\alpha = 60^\circ$



(c) $\alpha=30^\circ$

Figure 6.9 Minimum velocities that caused embedding in PMMA as a function of the particle orientation, θ , (Fig. 6. 8) at different impact angles (α) using 136 μm garnet particles.

It is seen that the minimum velocities that cause embedding occurred when the incident velocity vector was aligned with the major axis of the particle; i.e. when $\theta \approx 90^\circ - \alpha$ (Fig. 6.3). The result is intuitively obvious and is consistent with the reasoning of Papini and Spelt [69], who found that the transition from forward to backward rotation upon impact occurred under these conditions; i.e. that most of the incident kinetic energy results in particle penetration, rather than being consumed in rotating the particle upon rebound [69].

Figure 6.9a shows that the predicted minimum embedding velocity is zero for $\alpha=90^\circ$ if particles arrive with their major axis normal to the surface ($\theta=0^\circ$) due to the

fully plastic assumption of the model of Section 6.2.1 which neglects the possibility of purely elastic target deformation for very low speed particles. Nevertheless, the possibility of particle embedding even at very low impact velocities cannot be completely excluded. For example, Sari [74] observed the embedment of fractured aluminum oxide particles in polyphenylene sulfide (PPS) composite following impact of angular Al_2O_3 particles (150 μm - 212 μm) at only 1.57 m/s.

6.2.4 Model for Embedding of Spherical Particles

Walley and Field [33] presented experimental data for the impact of 4 mm spherical steel particles on a polyethylene target. To determine the trajectories of particles as they ploughed craters into the targets, and thus gain insight into possible embedding mechanisms, the rigid-plastic model similar to that developed in Section 6.2.1, but for spherical particles [126-128], was used to analyze the experimental results of [33] at oblique impact angles. The target material and particle properties are given in Table 6.3.

Table 6-3 Particle and target material properties. Subscripts 1 and 2 are for target and particle, respectively. * Values obtained from [33]. ** Values obtained from [129].

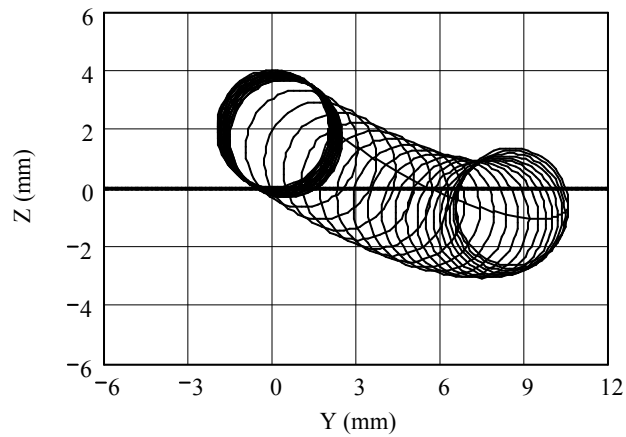
	Target	Particle
Elastic modulus, E_1, E_2 (GPa)	0.3 ^{**}	210
Yield strength, σ_{y1} (MPa)	45 [*]	700
Poisson ratio, ν_1, ν_2	0.4 ^{**}	0.3
Mass, m_2 (mg)		258 [*]
Diameter of particle (mm)		4 [*]

6.2.5 Spherical Particle Embedding Criteria-Comparison with Experimental Results

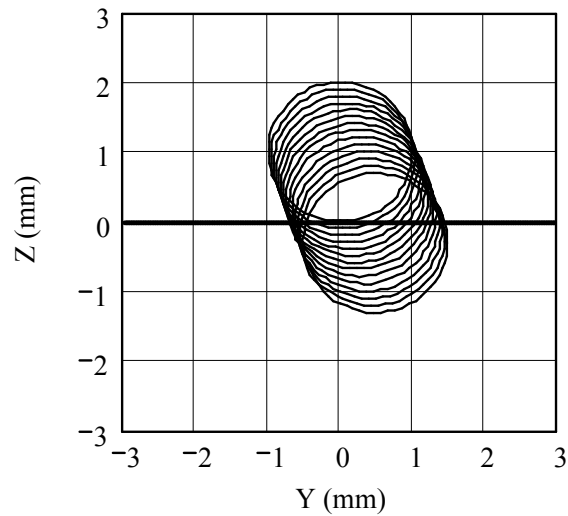
It was hypothesized that a spherical particle would embed only if it penetrates the substrate to a depth more than its radius so that sufficient material is displaced to envelope the particle preventing its ejection by elastic forces. The hypothesis is consistent with the hypothesis of Walley and Field [33], who constructed a “deformation map” of the different types of craters that were observed and found that if the incident velocity was sufficiently high, sufficient material was displaced to surround the sphere and prevent its rebound by elastic forces. The rigid-plastic model of Section 6.2.4 was run with the same experimental conditions used in [33]. For example, Fig. 6.10a shows the results for 4 mm steel sphere impacting a polyethylene target at a 35° impact angle and 288 m/s. Although the model does not show the formation of lips, when it comes to rest the particle has penetrated to a depth greater than its radius, making it possible for the surrounding target material to envelope the particle and prevent its rebound. It is noted that the angular particles analyzed in Section 6.2.2 embed on impact without ploughing along the surface; therefore, the embedding criterion for angular particles depended only on the static coefficient of friction, whereas with spherical particles, the dynamic coefficient of friction plays a role in the sliding of the particle. Figure 6.10b shows the model results for another case that was reported to embed [33]; i.e. a 2 mm diameter steel sphere with incident velocity 260 m/s at 70°. The particle was predicted to come to rest 1.3 mm below the surface, a distance that is larger than its radius. The model also predicted quite well the distance traveled by the ploughing particle (Fig. 10a) at 35°

impact. For example, in Fig. 10a the 4 mm particle is seen to travel horizontally approximately 7 mm, as measured by Walley and Field [33]. The measured value equalled the predicted ploughing distance when the dynamic coefficient of friction 0.2 was assumed, which is very close to the coefficient of friction that has been reported to be in the range of 0.21-0.23 for steel on HDPE [130].

Figure 6.11 compares the experimental incident velocities used in [33] which resulted in embedding of 4 mm diameter steel spheres into polyethylene, and the incident velocities predicted by the model (dynamic coefficient of friction 0.2) to satisfy the embedding criterion. The rigid-plastic model predictions were in good agreement with the experimental results up to 65° impact angle ($\leq 20\%$ difference). At 70° the difference was 30%, and it continued to grow at higher impact angles, probably because of the growing influence of rebound forces due to elastic target deformation, which the rigid-plastic model ignored.



(a)



(b)

Figure 6.10 (a) Predicted trajectory of steel sphere impacting a polyethylene target at (a) 35° impact angle and 288 m/s velocity, 4 mm particle diameter; (b) at 70° impact angle and 260 m/s incident velocity, 2 mm particle diameter. The target surface is at $Z=0$, and the trajectory is modeled from first contact to the point at which the particle comes to rest.

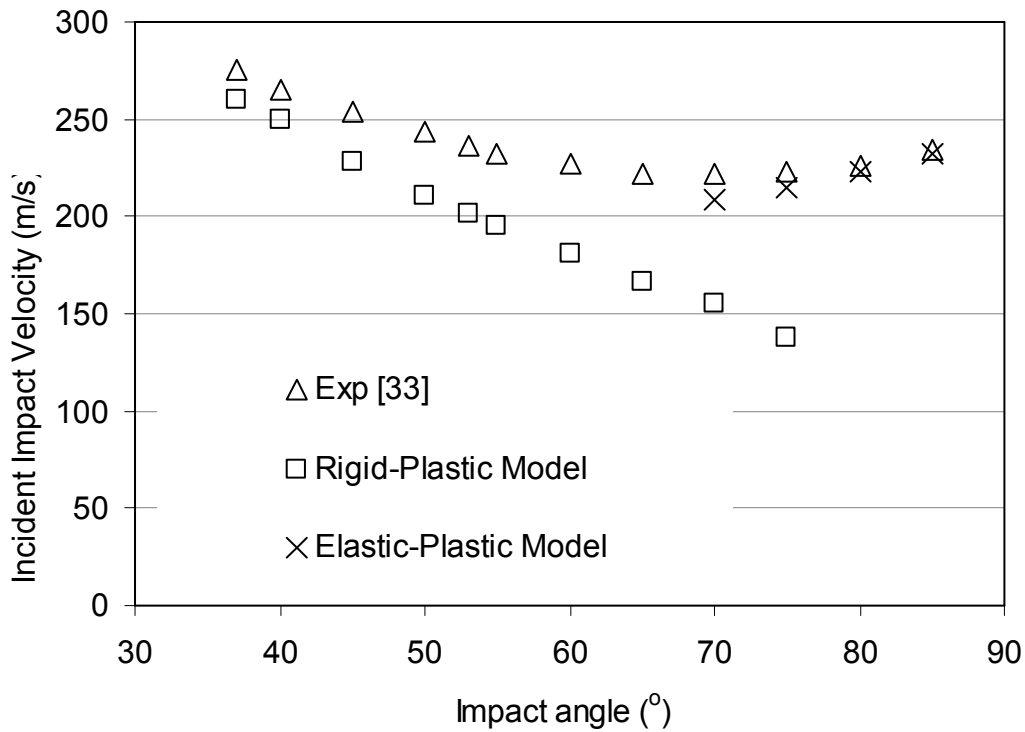


Figure 6.11 Comparison of model and experimental [33] results for embedding of 4 mm diameter steel spheres in polyethylene. Δ : measured incident velocities that resulted in embedding [33]; \square : predicted incident velocities that resulted in embedding with rigid plastic model; \times : predicted incident velocities that resulted in embedding, elastic-plastic model.

For impact angles between 70° and 90° , an existing elastic-plastic model, originally developed for the normal impact of two spherical particles [131] was modified to simulate the impact of a sphere on semi-infinite elastic-plastic plane. The elastic phase of the contact was modeled using Hertz contact theory [132]. At the onset of yield below the contact surface, an elastic region was assumed to surround the plastically deformed inner region [131]. The maximum impact force was obtained by summing the reaction forces in the elastic and plastically-deformed regions when the particle had come to rest [132], and this was taken to be the force at the beginning of the rebound phase. The model assumed that friction effects were negligible [133]. The equations of motion for

the three phases were solved to obtain the time-indentation relationship, and the crater depth after elastic spring-back.

These final crater depths were compared with the experimental results of Walley and Field [33], using the normal components of the impact velocities (Fig. 6.12). For the four tested impact angles (70° , 75° , 80° and 85°) the predicted indentation depths were greater than the 2 mm radius of the sphere suggesting correctly that the particles would embed. At 65° impact angle, the depth predicted by the elastic-plastic model was 1.93 mm, meaning that embedding was not predicted even though it was observed in [33]. The result confirmed that the rigid-plastic model was applicable for spherical particles between 35° and 65° , while the elastic-plastic model worked from 70° to 85° .

Walley and Field [33] reported that at 90° steel spheres often penetrated the polyethylene to a depth almost equal to their diameter, but never embedded. Figure 6.12 shows that the elastic-plastic model predicted the crater depths for 90° impacts of 4 mm steel spheres quite well, with a maximum error of about 12%. Embedding did not occur regardless of penetration depth. The most likely reason for spherical particles not embedding at 90° is that the elastic rebound force is always sufficiently high to overcome the frictional forces tending to retain the particle. Therefore, the proposed spherical particle embedding criterion of penetration greater than the radius is irrelevant for 90° impacts.

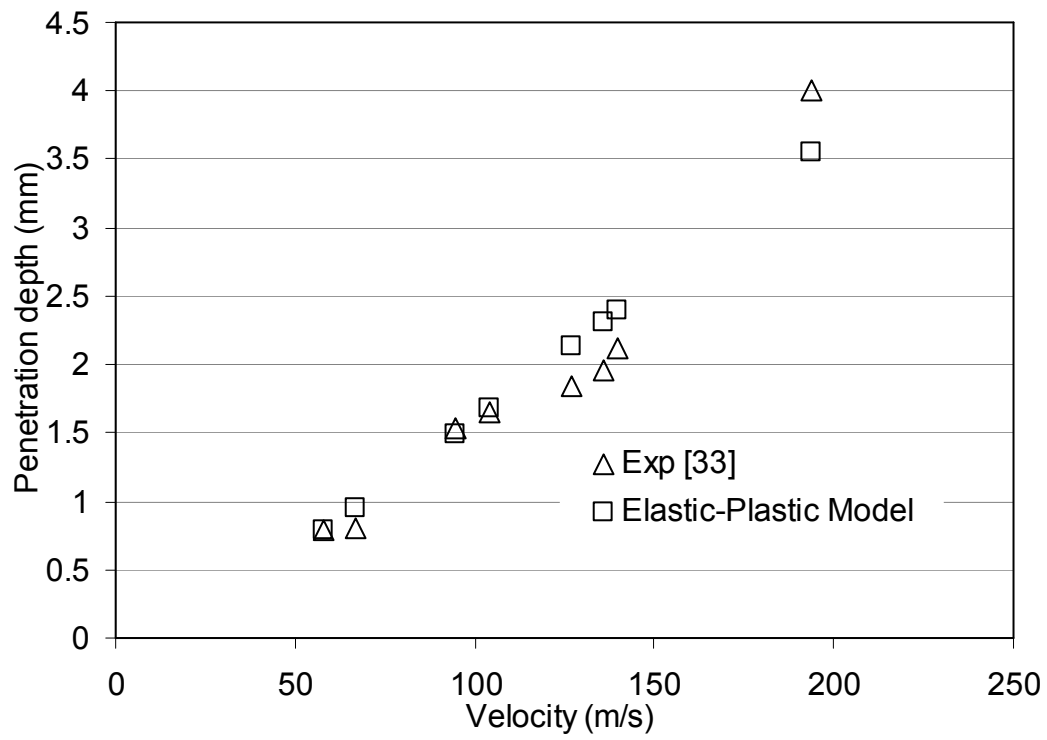


Figure 6.12 Comparison of predicted (elastic-plastic model) and measured [33] indentation depths at 90°.

6.3 Chapter Summary

The most important findings of this chapter can be summarized as follows:

- a) The model predicted that angular particles embed if two criteria are met: (a) particles should maintain contiguous contact with the target along both faces throughout the impact, and (b) the elastic rebound force generated by the normal clamping pressure on the particle faces must be less than the frictional force that tends to retain the particle. This second criterion implies that the likelihood of embedding is proportional to the static coefficient of friction between the particle and the target.
- b) For angular particles, it was found that the predicted static coefficient of friction was independent of particle size and impact angle for a given particle and target system. It was also found that for the investigated particle/target systems particle embedding did not depend on the particle size.
- c) For angular particles, embedding is predicted to occur most readily (i.e. with least incident velocity) when the velocity vector is aligned with the major axis of the rhomboid-shaped particle.
- d) Spherical particles impacting at incidence angles up to 85° are likely to embed if they penetrate the substrate to a depth more than their radius. It is believed that deep penetration allows the displaced material to envelope the spherical particle and prevent ejection by elastic forces.
- e) At 90° the elastic rebound force is sufficiently high to overcome the frictional forces tending to retain the particle. Therefore, it is most unlikely for embedding to occur at this impact angle.

7 Reduction of Particle Embedding in Solid Particle Erosion of Polymers

In Chapter 4, embedding was evaluated in a relative sense, and no absolute quantification was made. In this chapter, the fractional area coverage of embedded particles was quantified in PDMS, PTFE and ABS after machining under room and cryogenic temperature conditions and in PMMA after room temperature machining. Several methods for the removal of aluminum oxide particles embedded in ABS, PTFE, PMDS and PMMA as a result of AJM were studied. Their effectiveness in reducing particle embedment was quantified using scanning electron microscopy (SEM) with energy dispersive x-ray spectroscopy (EDX). Much of this chapter has been published in [134, 135].

7.1 Experiments

7.1.1 *Materials*

Particle embedding was investigated on the following target materials:

- (1) 1.6 mm thick PMMA sheet (Acrylic FF sheet, CYRO Industries, Rockaway, NJ, USA).
- (2) 2 mm thick PDMS samples (Sylgard[®] 184 Silicone elastomer, Ellsworth Adhesives, Germantown, WI, USA) which were cured in a vacuum oven for 4 h at 75 °C.

(3) 3 mm thick ABS sheet (McMaster-Carr, 200 Aurora Industrial Pkwy., Aurora, OH, USA).

(4) 2 mm thick PTFE sheet (McMaster-Carr, 200 Aurora Industrial Pkwy., Aurora, OH, USA).

7.1.2 Machining Experiments

The experimental setup and conditions described in Section 3.1 were used in all machining experiments. The embedding experiments were performed with nominally 25 μm Al_2O_3 as described in Section 4.2. The stand-off distance (h) between the abrasive nozzle tip and the target was held constant at 20 mm, perpendicular to the target in all cases. Use of a 200 kPa blasting pressure and a 760 μm inner diameter round nozzle resulted in an average particle velocity in the range of 100 - 110 m/s [79].

Two different types of experiments were performed in order to investigate particle embedding:

(a) Single and multi-pass unmasked channels were machined at 90° impact angle using a 0.5 mm/s scan speed in PMMA, ABS, PTFE and PDMS using 25 μm Al_2O_3 . The particle mass flow rate was measured to be 2.83 g/min (standard deviation of 0.12 g/min) by weighing (mass balance with accuracy of 0.1 mg) the amount of powder blasted into sealed container with a particulate filter for 2 min prior to each machining experiment. Cryogenic AJM was carried out in ABS,

PTFE and PDMS in order to quantify the fractional area coverage of embedded particles. The experimental setup described in Section 4.1 and the experimental conditions described in Section 4.2 were used for these CAJM experiments.

(b) While scanning at a constant velocity in one direction, the PMMA samples were simultaneously oscillated at 5 Hz in the direction perpendicular to the scan direction to create a 10 mm wide band of preconditioned surface with an approximately uniform coverage of embedded particles. The number of embedded particles was controlled by varying the scan speed between 0.5 mm/s and 3 mm/s. Unmasked channels were then machined into the preconditioned samples using a constant scan speed of 0.5 mm/s in order to determine the effect that the varying degrees of particle embedding had on the material removal rate (Section 7.2.1b).

7.1.3 Methodologies for Removal of Embedded Particles

The following techniques were evaluated for the removal of embedded particles:

- (i) The nozzle was re-aligned with the centerline of the channel in PMMA, ABS, PDMS and PTFE samples from (a) in Section 7.1.2, and blasted using 50 μm spherical glass beads at a scan speed of 0.5 mm/s at impact angles of 45° and 90° for two passes at each angle. The scanning speed was chosen to obtain sufficient coverage of the surface, while limiting the machining done by the glass beads. Since

embedded particles remained, the other particle removal procedures listed in (ii-vi) below were also used on samples that had been blasted with the glass beads at 45°.

- (ii) Three of the PMMA samples that were blasted with glass beads at 45° in (i) were ultrasonically (Fisher Scientific FS30, Pittsburgh, PA, USA) cleaned in distilled water for 15 min.
- (iii) Three of the PMMA samples that were blasted with glass beads at 45° in (i) were immersed in NaOH and ultrasonically cleaned for 15 min.
- (iv) PVC electrical insulation adhesive tape was pressed onto the machined surfaces of three of the PMMA and three of the ABS samples that were blasted with glass beads at 45° in (i). The tape was removed after 2 h in an attempt to pull out the embedded particles.
- (v) Freezing method: Three samples each of the PMMA, ABS, PTFE and PDMS that were blasted with glass beads at 45° in (i) were dipped in distilled water mixed with detergent to aid wetting. The samples were then frozen for 5 min by immersing them in liquid nitrogen (LN₂), after which the samples were allowed to warm to room temperature, rinsed in distilled water and left to dry. The mechanism of embedded particle removal was believed to be the difference in thermal shrinkage of the machined substrate and the expansion of the freezing residual water.

- (vi) A further 3 samples each of PMMA, ABS, PTFE and PMDS that were blasted with glass beads at 45° in (i) were subject to a procedure identical to that used in (v), except that wetting was with an NaOH solution mixed with detergent prior to freezing. The goal was to enhance the water wetting of embedded Al₂O₃ particles by etching.

7.1.4 Surface Evaluation Methods

Particle embedding was quantified using SEM and energy dispersive x-ray analysis (EDX) after each treatment described in Section 7.1.3. The use of EDX improved the accuracy of particle detection since it became difficult to visually distinguish particles from roughness features as machining progressed.

Figure 7.1a shows a typical EDX map of a sample blasted with Al₂O₃ showing the Al as white areas. Using digital image analysis software (ImageJ, rsbweb.nih.gov/ij/), the image was first reversed, and then filtered to remove noise using a median filter with 2 pixel radius. Finally, edge detection and area filling were used to identify the embedded particle area coverage as shown in Fig. 7.1b.

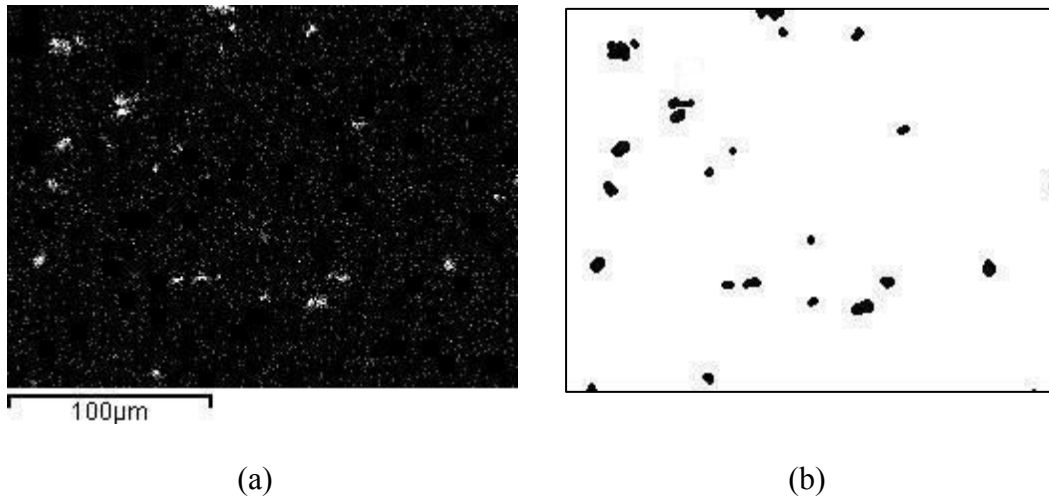


Figure 7.1(a) EDX mapping of Al in PMMA; white areas represent aluminum, and (b) final area coverage of aluminum oxide obtained from image processing.

In these images, a 1 pixel x 1 pixel area represented $1 \mu\text{m}^2$, and a lower particle detection threshold of $10 \mu\text{m}^2$ was used. For a given sample, five $250 \times 200 \mu\text{m}$ areas were selected randomly from the center of the machined area to evaluate the embedded particle area coverage.

The difficulty in quantifying the number of embedded particles using SEM images alone is illustrated in Fig. 7.2 for PDMS blasted as described in Section 7.1.2. The images of the embedded particles in this case were taken at an oblique angle and were amongst the clearest observed on any of the targets. Although they represent the most accurate visual identification using SEM alone, the size of the particles and the area coverage was difficult to measure using image analysis because of the shadowing behind each particle. In this case the area coverage was estimated by counting the particles and assuming a nominal particle diameter of $25 \mu\text{m}$. In this way, the fractional area coverage

was estimated to be approximately 15%, which was about 10% less than the measurement made using EDX.

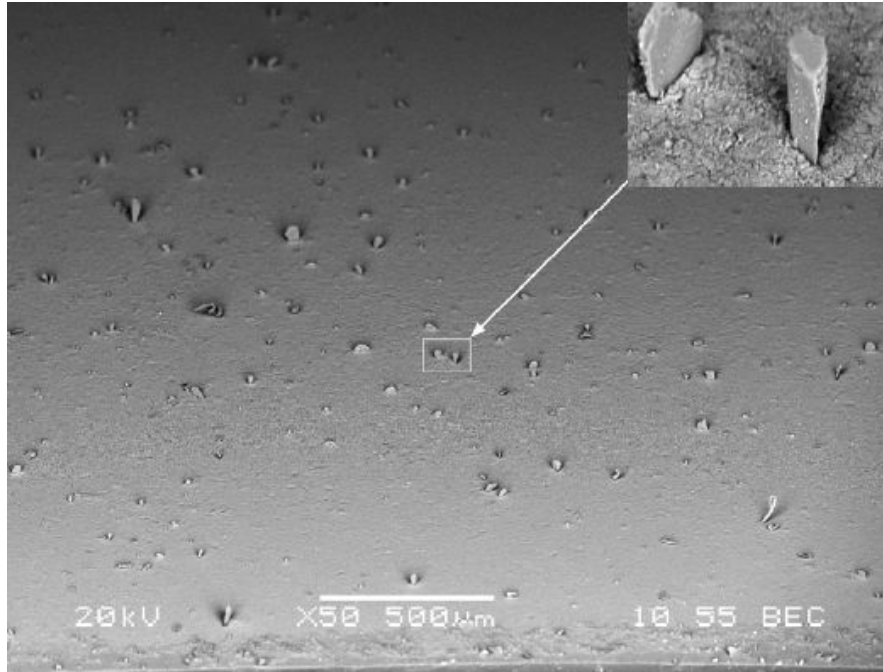


Figure 7.2 SEM of embedded particles in PDMS. Blasting conditions as described in Section 7.1.2(a).

To determine whether alumina particles were actually embedded in the substrate, rather than simply adhering to the surface due to electrostatic charge, several unmasked channels that had been machined in ABS using four passes of the jet were treated with a static charge remover (Kodak Static Eliminator, Model A2K, Eastman Kodak Company, Rochester, New York, USA) and then blown with compressed air. This procedure did not produce any measurable change in the numbers of particles on the surface and it was concluded that adhesion due to static charging was insignificant.

7.2 Results and Discussion

7.2.1 Particle Embedding in PMMA

(a) Removal of Embedded Particles

It was hypothesized that it might be possible to remove embedded particles from PMMA by striking them with other types of incoming particles that would themselves not embed. Spherical glass beads (50 μm diameter) were suitable for this purpose since SEM images confirmed that they had a low tendency to embed.

Table 1 shows the fractional area coverage by embedded Al_2O_3 particles in unmasked channels that had been machined in PMMA using one to four passes as described in Section 7.1.2(a), and then blasted with glass beads as described in Section 7.1.3(i). The particle dose per pass for a scan speed of 0.5 mm/s was calculated to be 17 mg/mm^2 , which results in approximately 0.8 mg for the area analyzed (i.e. $250 \times 200 \mu\text{m}^2$), corresponding to approximately 250 Al_2O_3 particles of 25 μm diameter (density of $3,900 \text{ kg}/\text{m}^3$). The measured fractional area coverage of embedded particles was 3.2% (Table 7.1) after one pass of the nozzle, implying that approximately 8 of the particles out of 250 became embedded.

Table 7-1 Fractional area coverage of Al₂O₃ particles (\pm the standard deviation of 5 measurements) after 1-4 passes of the nozzle in PMMA before and after post blasting with glass beads. Removal efficiency defined as: $100 \times (\text{area coverage before glass bead blasting} - \text{area coverage after glass bead blasting}) / (\text{area coverage before glass bead blasting})$.

Cleaning procedure		No of passes			
		1	2	3	4
No cleaning	Fractional area coverage (%)	3.2 \pm 0.18	2.5 \pm 0.16	4 \pm 0.26	4 \pm 0.10
After blasting with glass beads at 90°, 7.1.3 (i)	Fractional area coverage (%)	1.2 \pm 0.12	1.1 \pm 0.15	1.7 \pm 0.11	1.6 \pm 0.14
	Removal efficiency (%)	62.5	56	57.5	60
	Statistically significant at 95% level of confidence	Yes	Yes	Yes	Yes
After blasting with glass beads at 45°, 7.1.3 (i)	Fractional area coverage (%)	0.5 \pm 0.02	0.5 \pm 0.09	1 \pm 0.05	1.1 \pm 0.14
	Removal efficiency (%)	84	80	75	72.5
	Statistically significant at 95% level of confidence	Yes	Yes	Yes	Yes

In general, the amount of embedding of Al₂O₃ before the glass bead treatment was found to increase with increasing number of passes, but there was considerable scatter. For 3 and 4 passes the area coverage remained the same at 4%, suggesting that equilibrium had been reached. The result is in agreement with the observations of Zu et al. [70], who found that a composite layer of silica particles embedded in aluminum reached a dynamic equilibrium when the rate of removal was equal to the rate of further erodent embedding. The formation of such a composite layer during solid particle erosion has also been reported by Shewmon and Sundararajan [136] for both alloys and pure metals. The creation of a composite layer in ABS was observed in the present experiments as discussed in Section 7.2.2.

Blasting with glass beads reduced the amount of embedded Al_2O_3 particles, particularly at 45° ; however it did not remove them completely. The decreases in the fractional area coverage of embedded Al_2O_3 particles after blasting with glass beads at 45° and 90° shown in Table 7.1 were found to be statistically significant with a 95% confidence level.

SEM observations showed that some glass beads remained on the PMMA surface after the blasting at 45° and 90° , but that most were not deeply embedded. The average fractional area covered by glass beads on five $250 \times 200 \mu\text{m}^2$ areas was less than 0.5% after the subsequent application of cleaning techniques described in Section 2.3(iv) and (vi). It was possible to remove all deposited glass bead particles using the ultrasonic cleaning technique described in Section 7.1.3(ii).

Ultrasonic cleaning after either immersion in water or NaOH (Section 7.1.3), methods (ii) and (iii)) was not effective in removing the embedded Al_2O_3 particles that were left on the PMMA after post AJM blasting with glass beads at 45° . The result is consistent with the results reported by Momber et al. [64] who found a significant amount of embedded aluminum oxide particles (8.4% area coverage) after ultrasonic cleaning of hot-rolled low-carbon steel (UH1) samples. After first being post-blasted with glass beads at 45° , further attempts were made to remove the remaining Al_2O_3 particles from four-pass machined PMMA channels using the cleaning procedures described in Section

7.1.3(iv – vi). Table 7.2 shows that the use of adhesive tape or freezing after immersion in NaOH with detergent yielded the best results.

Table 7-2 Fractional area coverage of Al₂O₃ particles (±the standard deviation of 5 measurements) after cleaning procedures described in Section 7.1.3 were applied to 4-pass machined PMMA samples. Removal efficiency = 100 x (area coverage after blasting with glass bead at 45° – area coverage after cleaning procedure)/(area coverage after blasting with glass bead at 45°).

Cleaning Procedure	Area Coverage
No cleaning procedure (%)	4±0.10
Glass bead blasting (GB) at 45°, 7.1.3(i) (%)	1.1±0.14
Removal efficiency (%)	72.5
Statistically significant at 95% level of confidence	Yes
Ultrasonic cleaning after GB blasting, 7.1.3(ii) (%)	1.05±0.05
Removal efficiency (%)	5
Statistically significant at 95% level of confidence	No
Freezing method 7.1.3(vi) after GB blasting (%)	0.2±0.03
Removal efficiency (%)	82
Statistically significant at 95% level of confidence	Yes
Freezing method 7.1.3(v) after GB blasting (%)	0.4±0.06
Removal efficiency (%)	64
Statistically significant at 95% level of confidence	Yes
PVC Tape 7.1.3(iv) after GB blasting (%)	0.2±0.05
Removal efficiency (%)	82
Statistically significant at 95% level of confidence	Yes

(b) Shielding of Surface by Embedded Particles

As mentioned previously, it has been reported that particle embedding can reduce the erosion rate [12, 70, 136]. In order to determine whether embedded Al₂O₃ particles shielded the PMMA surface from erosion by subsequent passes, samples were preconditioned as described in Section 7.1.2(b) in order to obtain different degrees of

uniformly distributed particle embedding. The preconditioning scan speeds and the resulting area coverage of Al_2O_3 particles are given in Table 7.3. Unmasked single pass channels of 20 mm length were then machined into the preconditioned samples using 25 μm Al_2O_3 particles at a scan speed of 0.5 mm/s. Channel cross-sectional areas were determined using an optical profilometer described in Section 3.4. Table 7.3 shows that the cross-sectional areas of these channels decreased as the initial particle embedding area coverage increased, confirming that particle embedding did indeed shield the substrate from the incoming particles. The result in agreement with the suggestion of Lathabai et al. [14] and Zhou and Bahadur [72] that embedded particles may confer a shielding effect.

Table 7-3 Average channel cross-sectional area (\pm the standard deviation of measurements of 3 sections) of PMMA target material removed when machining unmasked channels at 0.5 mm/s before and after preconditioning with embedding particles as described in Section 7. 1. 2(b). From each sample, 5 representative 0.25 x 0.2 mm areas were used to calculate the average (plus or minus the standard deviation) fractional area covered by Al_2O_3 particles after preconditioning.

	Preconditioning Scan Speed			
	0.5 mm/s	1 mm/s	2 mm/s	3 mm/s
Particle preconditioning dose (mg/mm^2)	3.38	1.69	0.844	0.564
% area covered by Al_2O_3 after preconditioning	2.57 \pm 0.42	1.5 \pm 0.26	0.67 \pm 0.32	0.23 \pm 0.06
Cross-sectional area of preconditioned channel after machining (μm^2)	18,125 \pm 101	19,500 \pm 514	20,625 \pm 131	21,000 \pm 99
Cross-sectional area of channel after machining without preconditioning (μm^2)	25,125 \pm 543			

7.2.2 Particle Embedding in PDMS, PTFE and ABS with Cryogenic AJM

Previous work has shown that AJM can be used to machine PDMS if liquid nitrogen (LN₂) is used to achieve sufficient cooling of the elastomer (Chapter 4) while it is being machined. The use of LN₂ also substantially decreased the amount of particle embedding, both in PDMS and in the non-elastomeric polymers ABS and PTFE (Chapter 4). LN₂ was not used for the machining of PMMA since particle embedding under ambient temperature was relatively small in this case (4% after 4-pass channel machining) and erosion enhancement was not observed when LN₂ was used. As mentioned previously, in Chapter 4, embedding was evaluated in a relative sense, and no absolute quantification was made. In the current work, micro-machined samples of these materials were prepared as described in Section 7.1.2(a) and were analyzed as described in Section 7.1.4. Table 7.4 shows the percentage of the total area covered by Al₂O₃ particles for ABS, PDMS and PTFE for channels machined with and without the use of LN₂.

Table 7-4 Percentage area covered by embedded Al₂O₃ particles (\pm the standard deviation of 5 measurements) after AJM with and without the use of LN₂.

	No LN ₂ (%)	With LN ₂ (%)
ABS	16 \pm 0.11	10 \pm 0.20
PDMS	25 \pm 0.13	1.6 \pm 0.26
PTFE	19 \pm 0.53	0.8 \pm 0.20

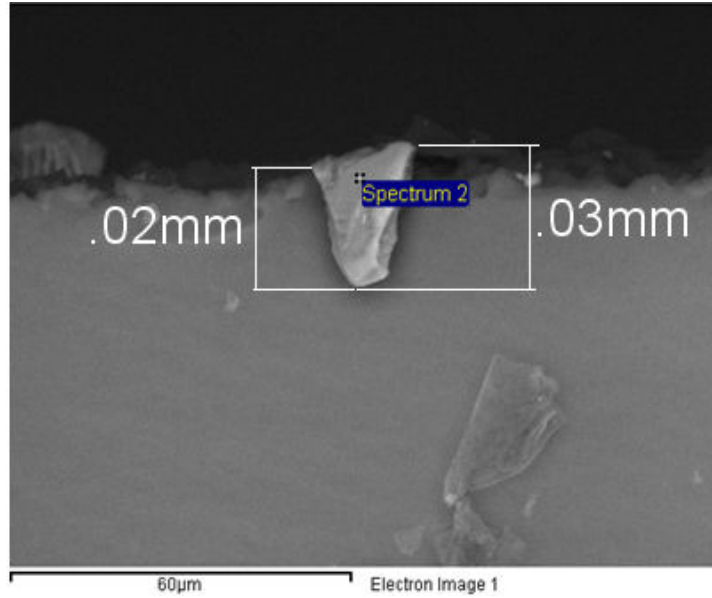
The use of LN₂ reduced the amount of embedded particles in the three materials significantly, with a confidence level of 99%. The samples that had been machined using LN₂ were then subjected to the cleaning procedures described in Section 2.3(i)-(vi) to attempt particle removal.

Table 7-5 Percentage area covered by Al₂O₃ in ABS, PDMS and PTFE before and after cleaning the samples that had been machined using LN₂. Glass bead blasting (GB) at 45° -7.1.3(i); GB at 45° followed by application of PVC adhesive tape – 7.1.3(iv); GB at 45° followed by distilled H₂O wetting and freezing – 7.1.3(v); GB at 45° followed by NaOH wetting and freezing – 7.1.3(vi).

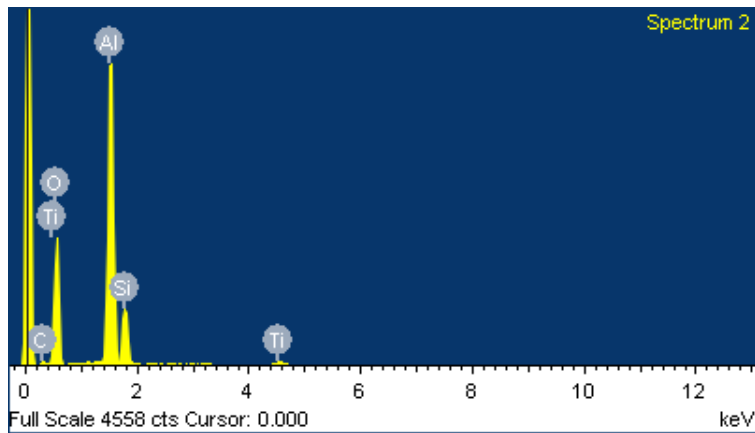
Cleaning Procedure	Area Coverage		
	ABS	PDMS	PTFE
After machining with LN ₂ , before cleaning (%)	10±0.20	1.6 ±0.26	0.8 ±0.20
After blasting with GB at 45° (%), 2.3(i)	7.1 ±0.65	1.4 ±0.07	0.4 ±0.1
Removal efficiency	29%	12%	50%
Statistically significant at 95% level of confidence	Yes	No	Yes
Freezing method 2.3(vi) after GB blasting (%)	4.3 ±0.18	0.4 ±0.02	0.1 ±0.01
Removal efficiency	39%	71%	75%
Statistically significant at 95% level of confidence	Yes	Yes	No
Freezing method 2.3(v) after GB blasting (%)	3.8±0.28	0.5 ±0.03	0.1 ±0.02
Removal efficiency	46%	64%	75%
Statistically significant at 95% level of confidence	Yes	Yes	No
PVC Tape 2.3(iv) after GB blasting (%)	5.7±0.21	N/A	N/A
Removal efficiency	20%	N/A	N/A
Statistically significant at 95% level of confidence	No	N/A	N/A

It is seen that post AJM blasting with glass beads at 45° (at room temperature) reduced particle embedding significantly in all materials except for PDMS. The reason for the decreased removal on PDMS may be that aluminum oxide particles were too deeply embedded to be dislodged (Fig. 7.3). Table 7.5 also shows that additional

embedded particles could be removed by using the cleaning procedures described in Section 7.1.3(iv)-(vi), after the post AJM glass bead blasting at 45°.



(a)



(b)

Figure 7.3 (a) Embedded Al_2O_3 particle in PDMS. Blasting conditions as described in Section 7.1.2(a) under cryogenic conditions, (b) energy dispersive X-ray analysis of PDMS sample blasted with alumina particles showing dominant Al peak due to embedding of Al_2O_3 particle.

The best result for PDMS and PTFE was achieved with the freezing methods of Section 7.1.3(v) and (vi). With these procedures, it was possible to reduce the area coverage of embedded particles to almost 0% in PTFE and to around 0.5 % in PDMS. However, in ABS, the same procedures resulted in approximately 4% area coverage of embedded particles. The reason for the 4% area coverage in ABS is not entirely clear; however, it might have been due to the formation of an approximately 20 μm thick composite surface layer of Al_2O_3 particles embedded in damaged ABS (Fig. 7.4), within which the Al_2O_3 particles were more deeply embedded. This mechanism is reminiscent of that proposed by daCosta and Vilar [137] who suggested that embedding could be promoted as a means of creating additional erosion resistance.

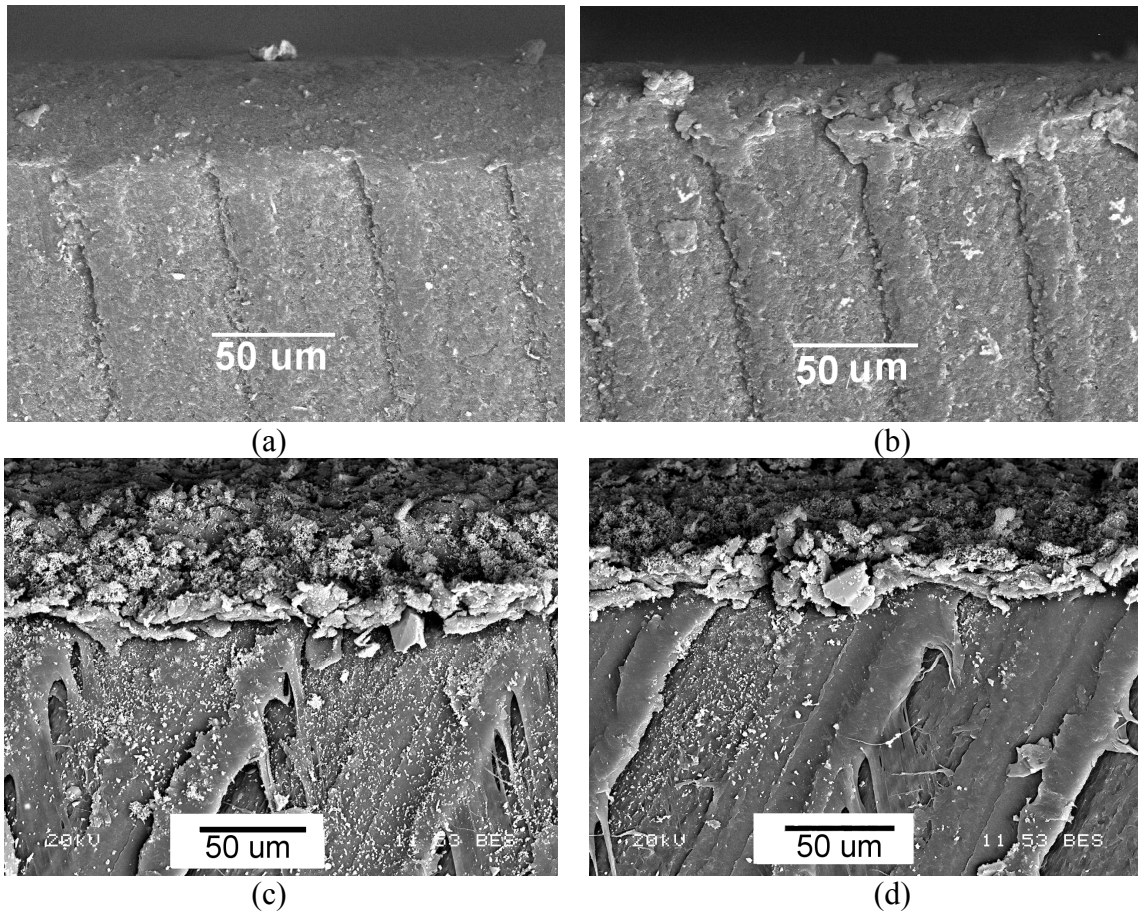


Figure 7.4 Development of composite layer in ABS during AJM. Cross-sections through the surface region after increasing numbers of passes of the scanning nozzle: (a) 1 pass, (b) 2 passes, (c) 3 passes, and (d) 4 passes. Blasting conditions as described in Section 7. 1. 2(a) under ambient temperature conditions.

As mentioned above, deeply buried Al_2O_3 particles in PDMS were not removed using spherical glass bead beads at room temperature. An attempt was made to clean the PDMS surface by blasting glass beads under cryogenic conditions using LN_2 at 45° and the conditions described in Section 7.1.3(i). The area covered by aluminum oxide particles was found to be $1.1\% \pm 0.23$, which was a slight decrease compared to the sample blasted with glass beads at 45° at room temperature ($1.4\% \pm 0.07$).

7.3 Chapter Summary

The most important findings of this chapter can be summarized as follows:

- a) Under cryogenic blasting conditions, the fractional area coverage by embedded particles was reduced to 10%, 0.8%, 1.6% from 16%, 19%, 25% for ABS, PTFE and PDMS, respectively.
- b) Blasting with glass beads removed a large fraction of embedded Al_2O_3 particles when applied at an impact angle of 45° . Following this glass bead blasting, the use of a liquid nitrogen freezing method further reduced the embedded particle area coverage in PMMA and PDMS to less than 0.5%, to almost 0% in PTFE, and to 4% in ABS.
- c) For PMMA, the application and removal of PVC tape after the glass bead blasting was also effective in removing embedded particles reducing the area coverage to less than 0.5%.
- d) Embedded particles shielded the substrate from incoming particles and thus reduced the erosion rate of PMMA. In ABS, a composite layer of particles and eroded polymer was observed to form rapidly, hindering any attempt at further reducing the amount of embedded particles.
- e) In practice, the glass bead blasting at 45° followed by the freezing method yields a significant reduction in embedded particles for all the studied polymers, although the combination of all the cleaning techniques yields the best results. However, it should also be noted that it is impossible to machine PDMS under ambient temperature conditions.

8 Conclusions and Future Work

To the author's knowledge, this thesis represents the first investigation of the use of CAJM for micro-machining elastomers and enhancing the machining rate in polymers. It is also the first work to establish the conditions that lead to embedding of angular and spherical particles in polymers. The other major findings are summarized below.

8.1 Summary of Useful Findings

8.1.1 *Novel Cryogenic AJM*

- a) Cryogenic cooling can be used to perform AJM on elastomers such as PDMS that are impossible to machine at room temperature at any impact angle, and to increase the erosion rate of certain polymers such as ABS and PTFE. It was also found that CAJM reduced the amount of particle embedding, at all angles of attack and for all the tested materials.
- b) For the developed CAJM setup, it was found that the thermal front advanced much faster than the material removal rate, enabling the cooling of a PDMS substrate during the CAJM of holes to be modeled analytically assuming a stationary heat transfer boundary.
- c) A finite element analysis was found to be appropriate for modelling the temperatures in the target PDMS during the CAJM of masked and unmasked channels by a cold abrasive jet scanned over the target surface. For the present

setup, the surface temperatures obtained using FE analysis could be used to estimate the temperature distribution inside the substrate at a depth equal to 0.02 μm , which was the approximate thickness of the chip of PDMS removed by an impacting aluminum oxide particle.

- d) The temperature at the center of the jet obtained using FEA compared reasonably well with the measured temperatures at the center of the channel with an approximately 20% error at typical scan speeds used in AJM. The model illustrated the asymmetric nature of the cooling with much more cooling occurring towards the trailing edge and large temperature gradient in the direction of the leading edge. As expected, the target temperature decreased with decreasing scan speed. The capability of machining PDMS at a temperature -67°C suggests the possibility of using medium other than LN_2 , such as dry ice, to effectively cool the PDMS substrate.
- e) The accuracy of the prediction of evolving surface profiles can be improved significantly if a finite element model is used to distort the first-pass profile, measured at room temperature, to its shape at the low-temperatures seen in CAJM, and this distorted profile is used to predict evolving surface profiles.

8.1.2 Particle Embedding Following Solid Particle Erosion

- f) Angular particles embed if two criteria are met: (a) particles should always have contiguous contact with the target at any point during the incident

portion of the impact and (b) the elastic rebound force generated by the normal clamping pressure on the particle faces is less than the frictional force that tends to retain the particle.

- g) For a given particle-target system, particles with the same angularities embed regardless of the particle size and impact angle. For angular particles, the minimum velocity that causes embedding occurs when the incident velocity vector is aligned with the major axis of the particle, indicating that this ($\theta \approx 90^\circ - \alpha$) is a preferred orientation for embedding to occur.
- h) Spherical particles impacting at incidence angles up to 85° are likely to embed if they penetrate the substrate to a depth more than their radius. The material displaced envelopes the spherical particles thus preventing ejection by elastic forces. At 90° the elastic rebound force is sufficiently high to overcome the frictional forces tending to retain the particle. Therefore, it is most unlikely for embedding to occur at this impact angle.
- i) Blasting with glass beads can be used to remove a large fraction of embedded Al_2O_3 particles when applied at an impact angle of 45° . Following this glass bead blasting, the use of liquid nitrogen freezing method or the application and removal of PVC tape can further substantially reduce the embedded particle area coverage.
- j) It was shown that embedded particles shield the substrate from incoming particles and thus reduce the erosion rate of PMMA. In ABS, a composite

layer of particles and eroded polymer was observed to form rapidly, hindering any attempt at further reducing the amount of embedded particles.

8.2 Original Contributions

The original contributions of the thesis are:

- (a) Development of a novel cryogenic abrasive micro-machining technique that enables micro-machining of elastomers, enhances erosion rate in polymers and substantially reduces particle embedding,
- (b) Development of experimentally validated FE model which is useful for determining the size of the cold region, and the effect of scan speed on the temperature distribution during CAJM of PDMS,
- (c) Use of an FE model to account for thermal distortion in the surface evolution prediction of features machined using CAJM,
- (d) Investigation of conditions that lead to particle embedding during AJM of polymers for both angular and spherical particles and determination of embedding criteria for both types of particles at oblique and normal impact angles,
- (e) Development of embedded particles removal techniques and procedures.

8.3 Recommendations for Future Work

The presented thesis is a pioneering work in the area of cryogenic abrasive jet micro-machining and determination of conditions leading to particle embedding. Thus there are several areas that need further development and investigation:

- a) Because the present set-up suggested that the LN₂ flow could be optimized, improvements to the LN₂ dispensing equipment could be made. For example, the possibility of entraining liquid nitrogen should be further investigated. The possibility of the use of three LN₂ nozzles symmetrically positioned that could precisely inject liquid nitrogen could also be investigated. Some preliminary work regarding has been presented in Appendix B.
- b) The thermal analysis showed that the PDMS was over-cooled and that the CAJM process could be further optimized to conserve LN₂ by decreasing its flow rate, or by pulsing the LN₂ jet so that the surface was only cooled periodically. The thermal analysis of pulsating heat sinks in CAJM should be investigated.
- c) The present model assumed that the abrasive jet and the cooling jet occupied the same volume; however, it may be more efficient for the cold jet to precede the abrasive jet so that cooling occurs sooner for a given scan speed and heat transfer coefficient. This possibility can be further explored.
- d) The present thermal analysis suggested that with a centerline temperature of approximately -67°C at a scan speed of 2 mm/s machining of PDMS is

possible suggesting the possibility that a medium other than LN₂, such as dry ice, could be used to effectively cool the PDMS substrate. This possibility should be tested.

- e) Cryogenic abrasive jet micro-machining of planar areas in PDMS should be investigated in the future. Following the work of [116, 117], planar area AJM could perhaps be achieved by oscillating the target.
- f) In Chapter 6 it was found that for the presently studied particle/target systems particle embedding did not depend on particle size for angular particles. Further investigation and experimental verification by taking size distributions of the embedded particles is necessary to generalize the hypothesis that particle embedding is not generally a function of particle size.
- g) Although a number of embedded particle removal methods have been developed and shown to be effective in some polymers, a 4 % area coverage by embedded particles was observed in ABS. The reason for the difficulty in removing the embedded particles in this case was attributed to the formation of an approximately 20 μm thick composite surface layer of Al₂O₃ particles and polymer. There is a need to develop an additional embedded particle removal technique for this material. Investigations should be carried out in order to explore the possibility of removing this layer by blasting with glass beads for longer period of time at 45° under cryogenic conditions.
- h) The possibility of using the Taguchi Methods of experimental design for a given particle-target system could be investigated for the CAJM of PDMS to

conserve LN₂, i.e. to predict an upper limit of abrasive jet scanning speed for a given cooling heat flux and spot size and the resulting erosion rate.

9 Appendices

Appendix A EDX Analysis of Surfaces Machined with and without LN₂

In Chapter 4, EDX mapping of embedded particles for the ABS sample machined at 90° without LN₂ (upper half), and sample micro-machined using LN₂ (the bottom half) were shown. Below the EDX mapping for ABS at 30° and 60°; for PDMS at 30°, 60° and 90°; and for PTFE at 30°, 60° and 90° are also shown. It is seen that in all cases the use of LN₂ reduced the amount of embedded particles.

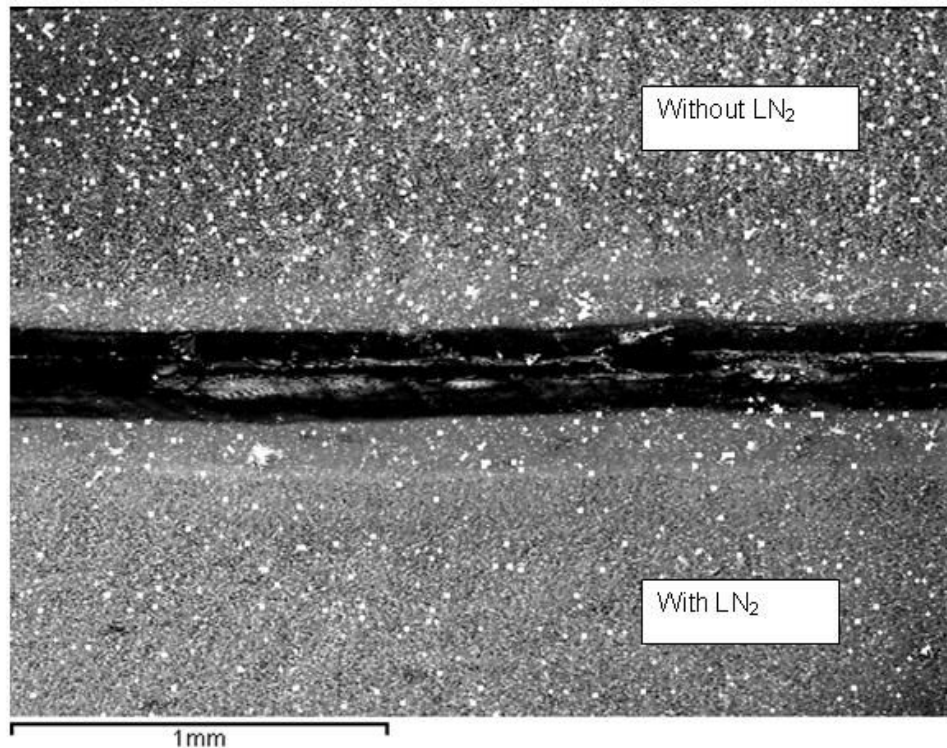


Figure A 1 EDX analysis of surfaces when machining ABS with and without using LN₂ at 30° impact angle. White dots are embedded Al₂O₃ particles.

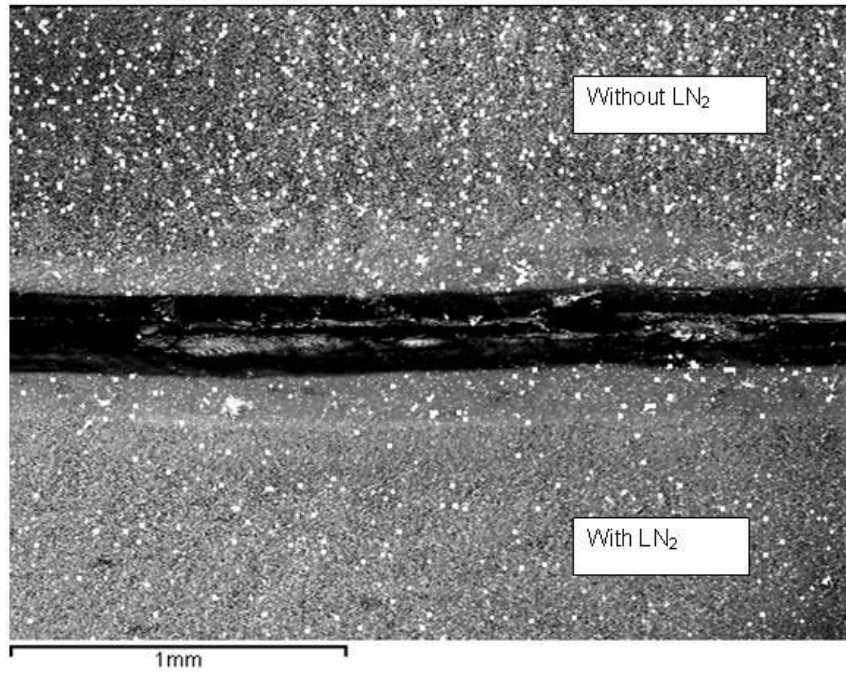


Figure A 2 EDX analysis of surfaces when machining ABS with and without using LN₂ at 60° impact angle. White dots are embedded Al₂O₃ particles.

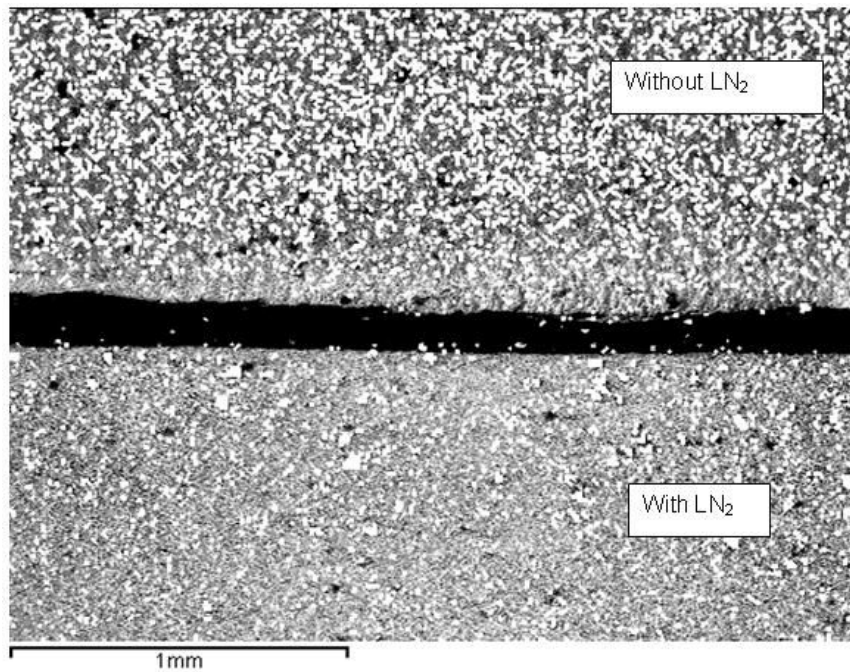


Figure A 3 EDX analysis of surfaces when machining PDMS with and without using LN₂ at 30° impact angle. White dots are embedded Al₂O₃ particles.

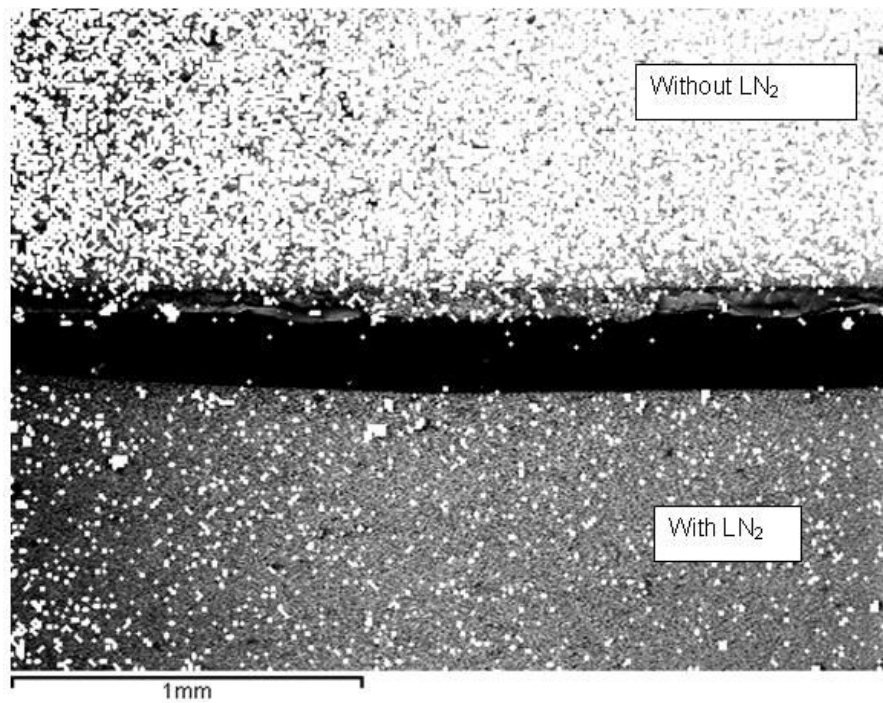


Figure A 4 EDX analysis of surfaces when machining PDMS with and without using LN₂ at 60° impact angle. White dots are embedded Al₂O₃ particles.

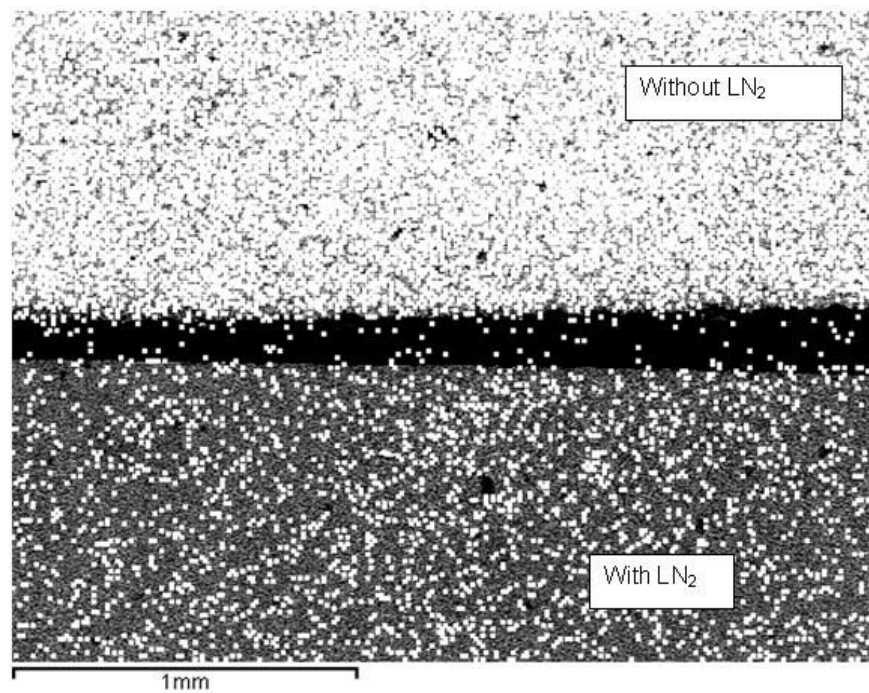


Figure A 5 EDX analysis of surfaces when machining PDMS with and without using LN₂ at 90° impact angle. White dots are embedded Al₂O₃ particles.

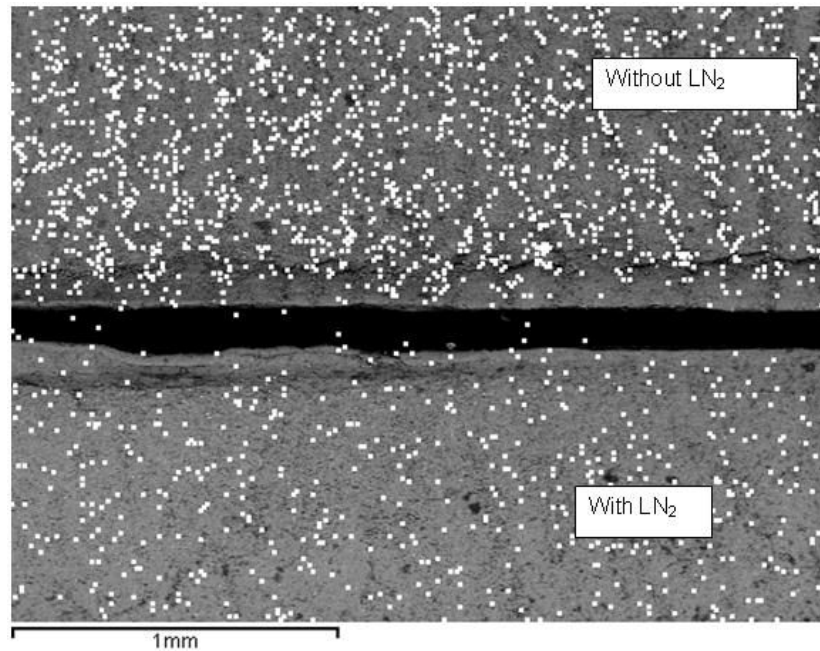


Figure A 6 EDX analysis of surfaces when machining PTFE with and without using LN₂ at 30° impact angle. White dots are embedded Al₂O₃ particles.

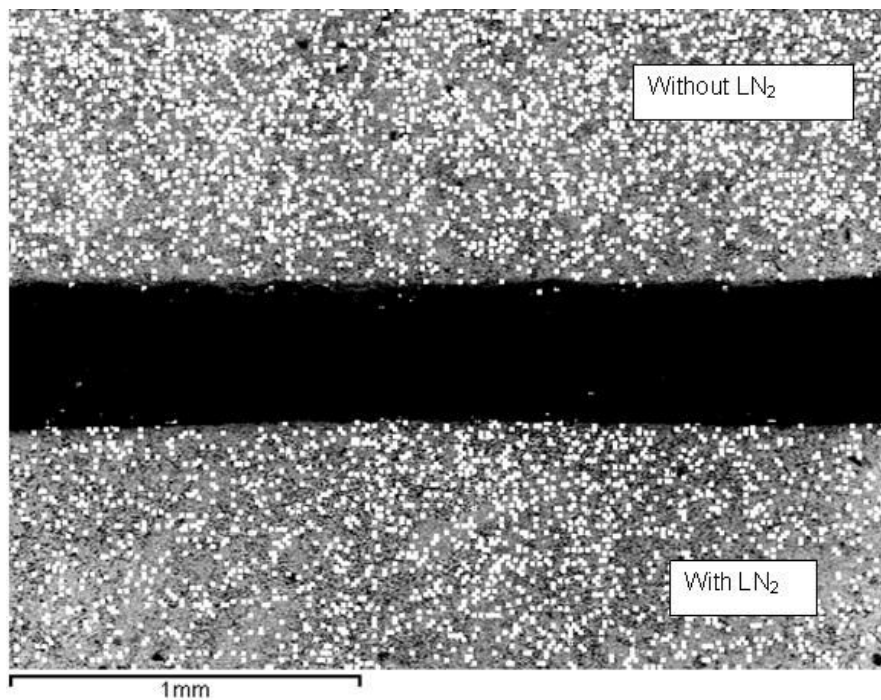


Figure A 7 EDX analysis of surfaces when machining PTFE with and without using LN₂ at 60° impact angle. White dots are embedded Al₂O₃ particles.

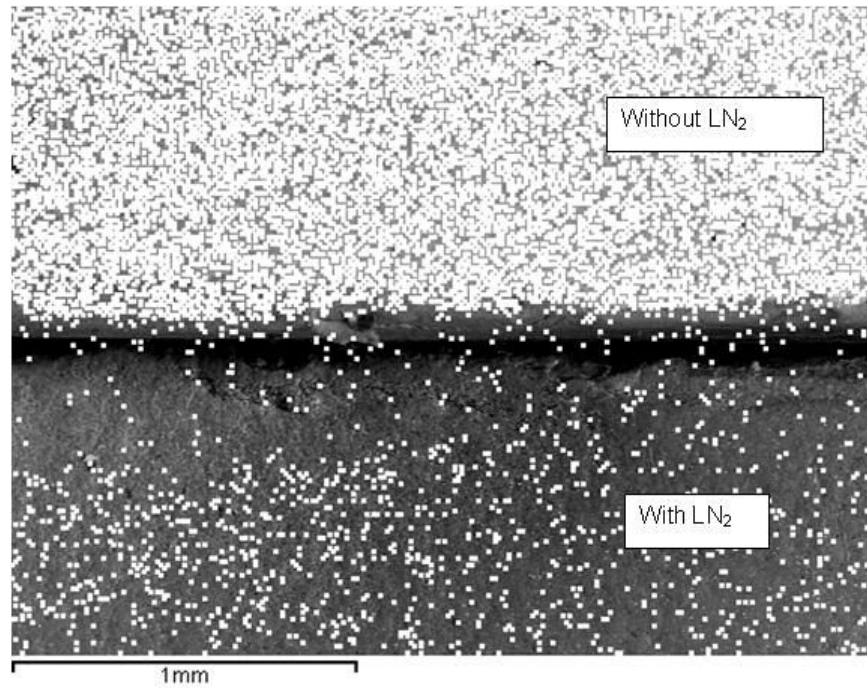


Figure A 8 EDX analysis of surfaces when machining PTFE with and without using LN₂ at 90° impact angle. White dots are embedded Al₂O₃ particles.

Appendix B Analytical Solution of a Moving Circular Heat Sink with Uniform Heat Flux Distribution

A general solution for the transient temperature field in a half-plane under a moving plane heat source or sink of circular shape was presented in [105]. Following the notation of [105], Fig. B1 gives the (X, y, z) coordinates of the moving circular heat sink with velocity v and (x, y, z) form the absolute coordinate system. At time $\tau=t$, the moving circular heat sink of radius r has traveled a distance equal to vt and the temperature drop, θ_p (K), at point P can be determined from

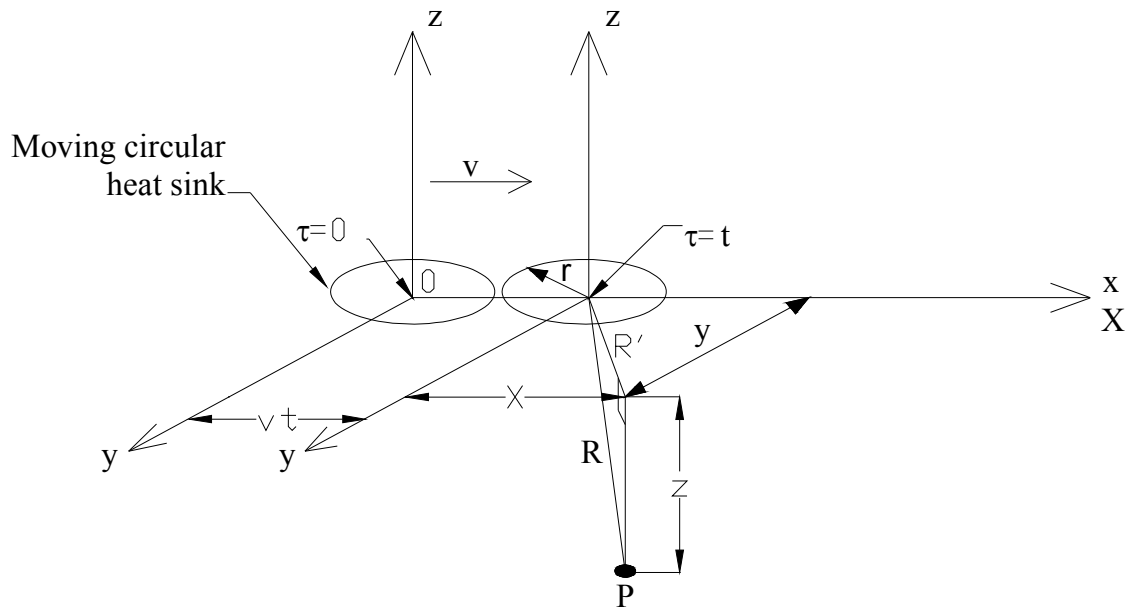


Figure B 1 Schematic of the moving heat sink.

$$\theta_P = \frac{q''v}{8E\kappa\alpha_{td}\pi^{\frac{3}{2}}a_{pl}} \int_{-j}^j Fdy \int_{-k}^k dXGe^{-\left[\frac{Xv}{2\alpha_{td}}\right]} \int_0^{\omega} \frac{d\omega}{\omega^{\frac{3}{2}}} e^{\left(-\omega - \frac{u^2}{4\omega}\right)} \quad (\text{B.1})$$

where $\omega = \frac{v^2t}{4\alpha_{td}}$ (dimensionless number related to the time to reach steady state),

$u = \frac{Rv}{2\alpha_{td}}$ (Peclet number, dimensionless heat transfer parameter relating velocity of the

moving heat sink to the conduction of the system) and R is the radial distance between the center of the moving heat sink and point P [105], a_{pl} is the area of the moving circular heat sink, for circular heat sink, $a_{pl} = \pi r^2$, and the limits of integration are $j=r$ and $k=r$. E, F, G are coefficients that describe the form of the heat flux distribution over the circular area (e.g. normal, parabolic, uniform) [105]. In this study a uniform distribution of q'' was assumed, therefore $E=F=G=1$ [105]. Equation (B.1) was solved numerically and the lower limit used for ω was 0.001 to ensure convergence [105]. Hou and Komanduri [105] estimated that a fully developed temperature field that translates with velocity v is established when $\omega \geq 5$. For example, the time required to establish a quasi-steady state condition for a scan velocity $v=1 \text{ mms}^{-1}$ given the thermal diffusivity of PDMS ($1.06 \times 10^{-7} \text{ m}^2\text{s}^{-1}$), is just over 2 s.

MathCad spreadsheet for solving Eq. B.1

$a_0 := 0.003\text{m}$

$b_0 := 0.003\text{m}$

$$v := 0.001 \frac{\text{m}}{\text{s}}$$

$$E := 1$$

$$C_p := 1460 \text{J} \cdot \text{kg}^{-1} \cdot \text{K}^{-1}$$

$$\rho := 970 \frac{\text{kg}}{\text{m}^3}$$

$$r_0 := a_0$$

$$\kappa := 0.15 \frac{\text{W}}{\text{m} \cdot \text{K}}$$

$$A_{pl} := \pi \cdot a_0 \cdot b_0$$

$$\alpha_{td} := \frac{\kappa}{\rho \cdot C_p}$$

$$q_{pl} := 9500 A_{pl}$$

$$t := 30 \text{s}$$

$$z := 0 \text{m}$$

$$\omega := \frac{v^2 t}{4 \alpha_{td}}$$

$$\alpha_{td} = 1.059 \times 10^{-7} \frac{\text{m}^2}{\text{s}}$$

$$q_{pl} = 0.269 \text{m}^2$$

$$A_{pl} = 2.827 \times 10^{-5} \text{m}^2$$

$$\text{start} := -0.05$$

$$\text{end} := 0.05$$

$$\text{incr} := 0.002$$

$$N := \text{ceil}\left(\frac{\text{end} - \text{start}}{\text{incr}}\right)$$

$$N = 40$$

$$j := 0..N$$

$$\Delta X_j := (\text{start} + j \cdot \text{incr}) \cdot \text{m}$$

$$\theta_{P_j} := \frac{v \cdot q_{pl}}{8 \cdot \kappa \cdot \alpha_{td} \cdot \pi \cdot \frac{3}{2} \cdot A_{pl}} \left[\int_{-b_0}^{b_0} \int_{-a_0}^{a_0} e^{\left[\frac{-(\Delta X_j - X) \cdot v}{2 \cdot \alpha_{td}} \right]} \left[\int_{0.001}^{\frac{v^2 \cdot t}{4 \cdot \alpha_{td}}} e^{-\omega} \left[\frac{\left[\frac{\sqrt{(\Delta X_j - X)^2 + (0 - y)^2 + z^2} \cdot v}{2 \cdot \alpha_{td}} \right]^2}{4 \cdot \omega} \right] d\omega \right] dX dy$$

$$T_i := 25\text{C}$$

$$T := T_i - \theta_M$$

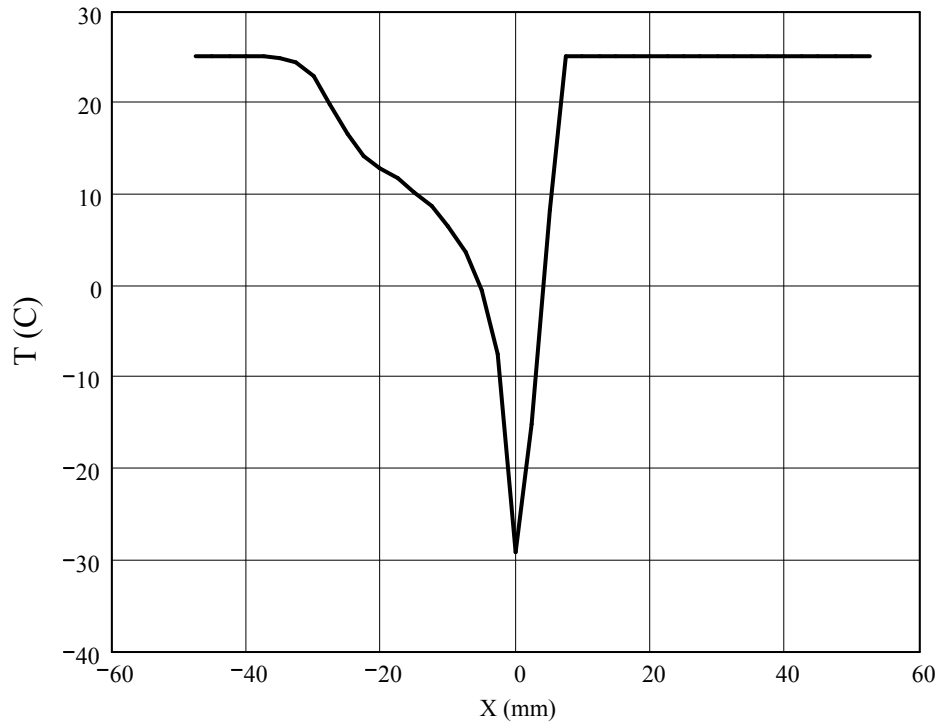


Figure B 2 Temperature distribution in PDMS predicted by the analytical models at the surface along the direction of motion (X -axis) through the center of the circular cooling jet ($Y=0$) for $q''=9500$ W/m^2 , $r=3\text{mm}$, $v=1\text{mm}/\text{s}$, $X=0$ represents the center of the moving jet.

Appendix C Comparison of Temperature Distributions: Heat Sink with Uniform and Gaussian Distributions of h_c

The FEA of Fig. 5.7 assumed that the heat transfer coefficient of the cooling jet had a Gaussian distribution over the circular impingement area (average $h_c=916 \text{ Wm}^{-2}\text{K}^{-1}$). The effect of this assumption was investigated for three scan speeds (0.15, 0.3 and 1 mm/s) by comparing it to a model that assumed a uniform distribution of convective heat coefficient of $916 \text{ Wm}^{-2}\text{K}^{-1}$ over the 6 mm diameter cold spot. Figure C.1 shows that the differences between the models with these two distributions of h grows as the scan speed increases, and that the uniform h_c distribution produces lower temperatures, particularly ahead of the jet centerline ($X=0$). The temperature differences between the models at the center of the jet where most erosion occurs are relatively small (e.g. 1°C at 0.15 mm/s scan speed).

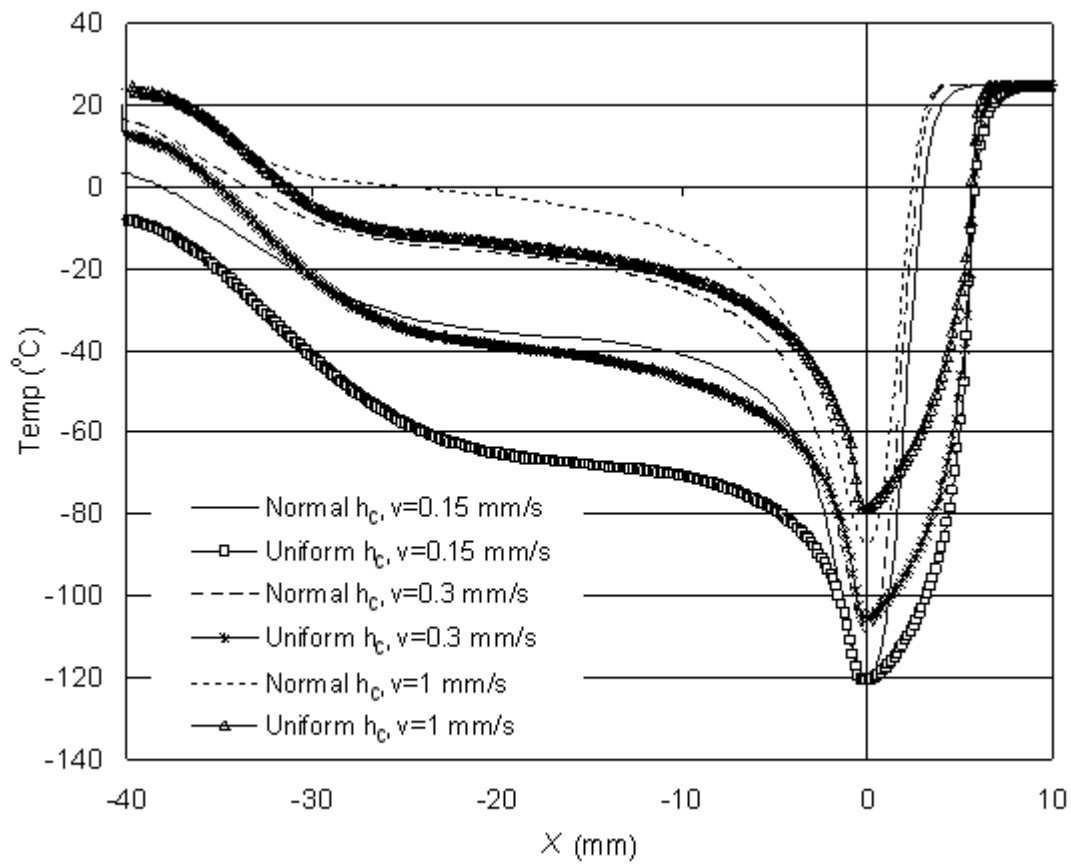


Figure C 1 Temperature distributions in PDMS at the surface along the direction of motion (X-axis) for different scan speeds and two convective heat transfer coefficient distributions – uniform and Gaussian.

Appendix D CAJM of Masked Channels: Overlapping Moving Heat Sinks

It is possible to increase the distance cooled in CAJM by overlapping the heat sinks. For example, at a scan speed of 1 mm/s, two cooling jets each with a 6 mm diameter circular footprint situated 2 mm apart from their centers (Fig D 1b) would create a temperature of -67°C over a distance of 3.9 mm (Fig. D 2), compared with approximately 1.8 mm with a single rectangular heat sink (Fig. 5.7), Chapter 5.

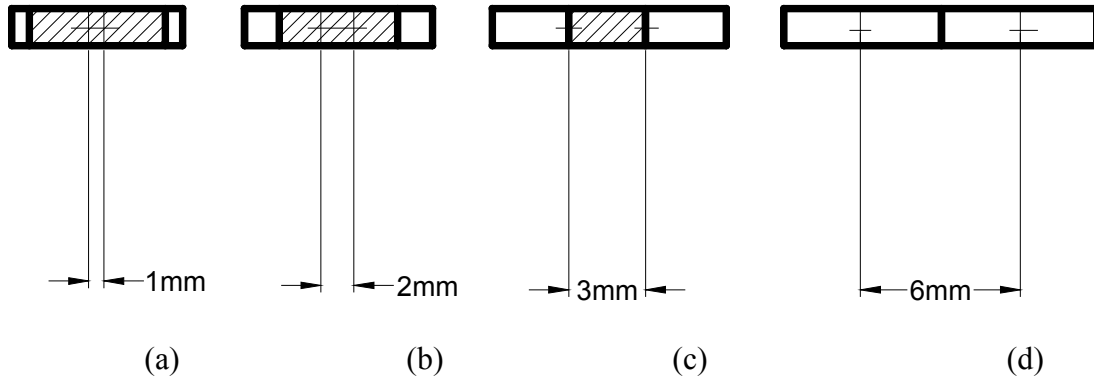


Figure D 1 Schematic of overlapping heat sinks: (a) 1mm apart from their centers, (b) 2 mm apart from their centers, (c) 3mm apart from their centers and (d) two consecutive heat sinks. Hatched region shows the area overlapped.

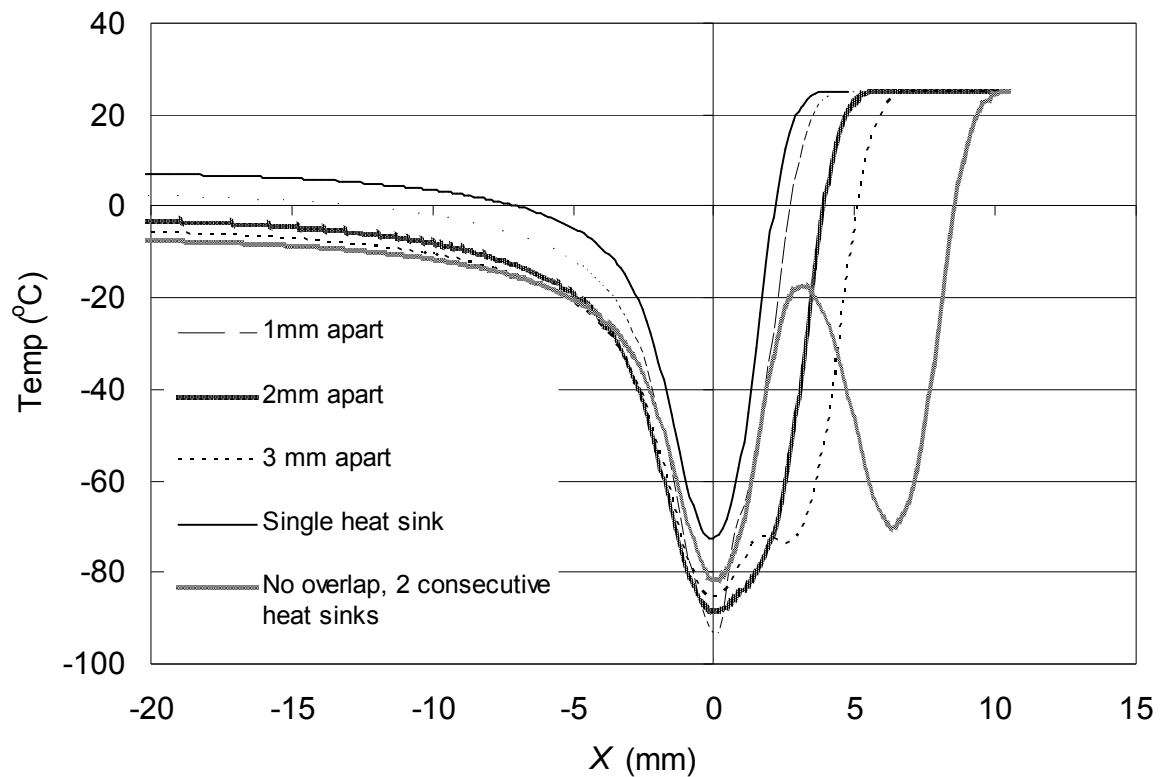


Figure D 2 FE predicted temperature distributions in masked PDMS samples at the surface along the direction of motion (X -axis) and through the center of the mask opening ($Y=0$), for different scan speeds with overlapping heat sinks. The Gaussian convective heat transfer coefficient distribution was used. $X=0$ represents the center of the moving jet.

The largest distance cooled (5.5 mm) to a temperature of -67°C was obtained when the heat sinks were situated 3 mm apart from their centers, i.e. when the trailing edge of the leading heat sink was coincident with the center of the trailing heat sink (Fig. D 1c).

Appendix E Device with LN₂ Entraining Nozzle

The following device was designed to help use LN₂ efficiently. In this design (Fig E 1), LN₂ is entrained to the air and abrasive mixture (at 45°) in the hand piece so that a cold abrasive jet is blasted through the nozzle to the target. The LN₂ entry nozzle is connected directly to the separate pressurizing equipment (Fig. 4.2). This arrangement was tested, however because the LN₂ pressure was lower than (170 kPa) that of the air-abrasive mixture (200 kPa), sufficient LN₂ was not entrained. Sufficient colling of the substrate to enable machining was not achieved. The device, however, may be modified and tested again. For example, use of a pressure vessel that enables supply of LN₂ that enters the abrasive mixture at slightly higher pressure (> 200kPa) than the air and abrasive mixture is a possible option. Also, the LN₂ nozzle inclination angle could be reduced from 45° to minimize the deflection of the abrasive particles and still providing an adequate mixing of the LN₂ with the abrasive jet.

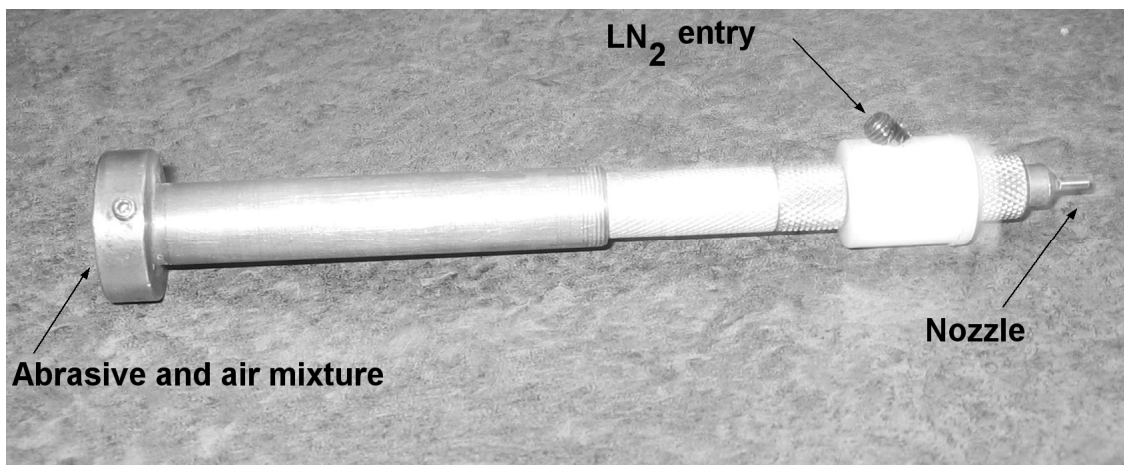


Figure E 1 Air-abrasive mixture hand piece with LN₂ entraining device.

Appendix F Effect of Particle Dose

If the minimum temperature that enables machining of PDMS is known, it is possible to use the thermal modeling techniques presented in Chapter 5 to predict an upper limit of abrasive jet scanning speed for a given cooling heat flux and spot size. However, it is not only the cooling temperature that should be considered, but also the dose of particles the target sees at a given scan speed.

To investigate this, CAJM experiments were performed on masked channels at various scan speeds and with two abrasive particle mass flow rates yielding the channel center line depths shown in Fig. F 1. Scan speeds of 3 mm/s and greater produced negligible erosion at a mass flow rate of 2.83 g/min because the particle dose received per unit area was too small to permit appreciable erosion. When the particle mass flow rate was increased to 6.1 g/min, however, an appreciable erosion rate could be measured at scan speeds of 3 mm/s and lower. The experiment demonstrates that both the cooling temperature and the particle dose per unit area are important in optimizing the CAJM process.

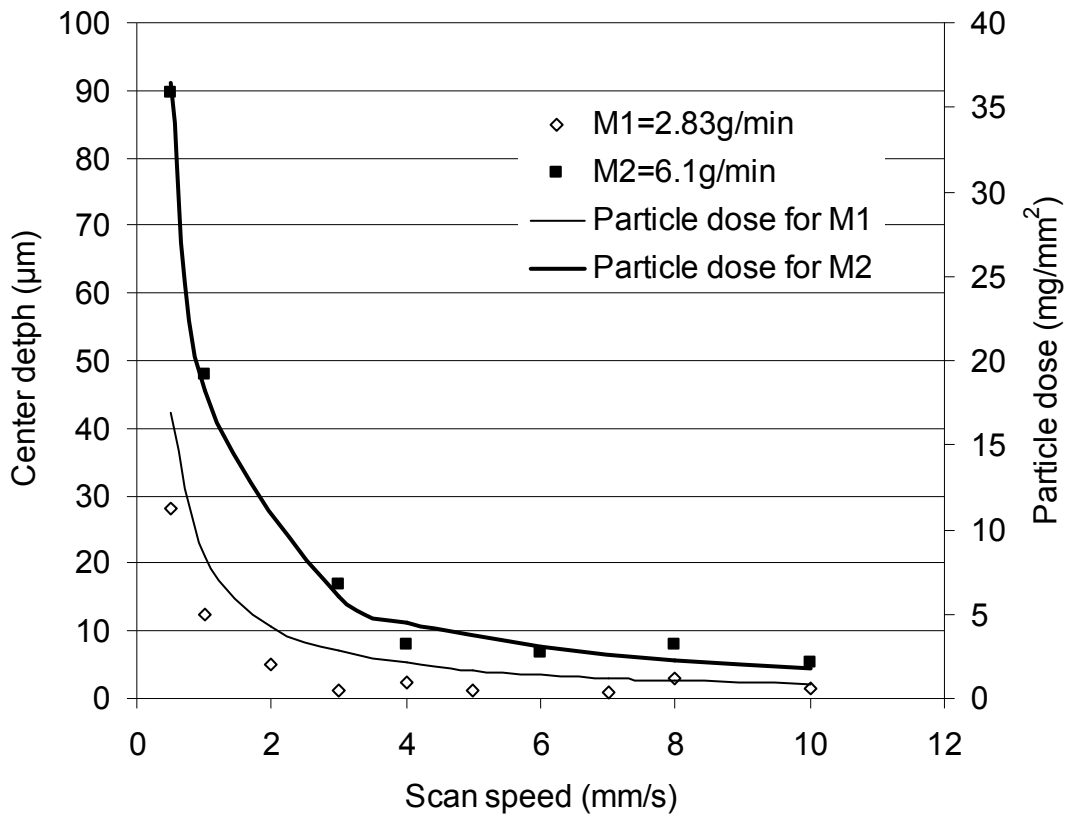


Figure F 1 Measured masked channel center depths as a function of scan speed using CAJM at two abrasive mass flow rates: M1= 2.83 g/min and M2= 6.1 g/min.

Appendix G Particle Size, Aspect Ratio and Area Distributions

In Chapter 6, it was mentioned that the garnet particles were approximated as a collection of idealized rhomboid shaped particles having the same aspect ratio, area and velocity distributions as the actual particles. The aspect ratio of garnet and Al_2O_3 particles were measured using a laser shadowgraphy system (described in Section 3.4) to determine more blocky particles so that they can be represented by a collection of rhomboids. For comparison these measurements were repeated with an optical particle size analyser (described in Section 3.4). Both methods of measurements showed a log-normal size distribution of both 136 μm and 103 μm garnet particles (Fig. 6.4, 6.5, G 9 and g 12). Figs. G 1 to G 12 show the size and aspect ratio distributions of Al_2O_3 and garnet particles of different sizes.

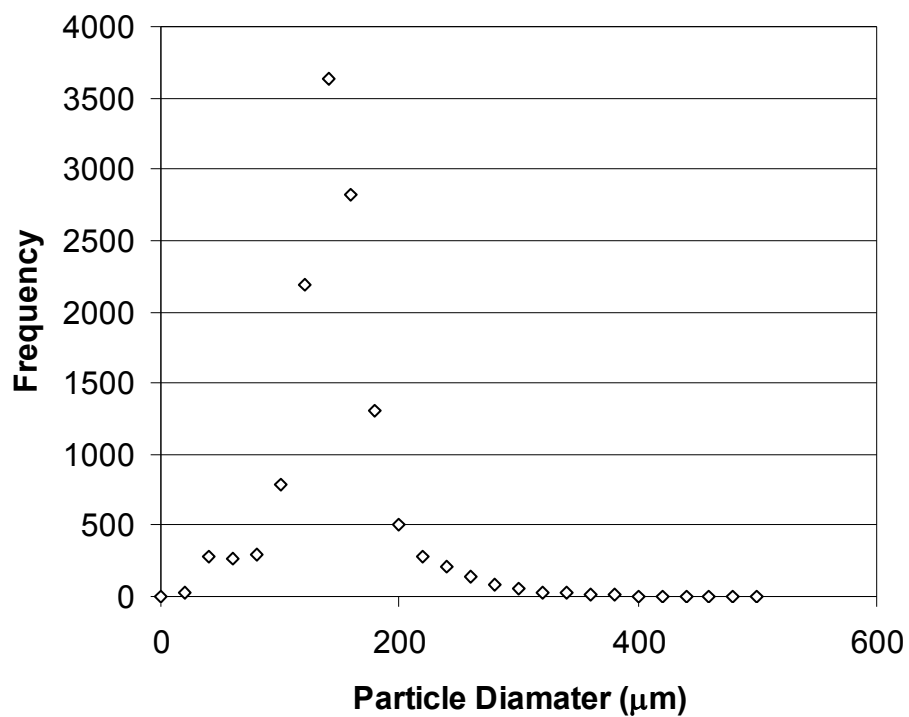


Figure G 1 Particle size distribution of nominally 100 μm particle Al₂O₃, average diameter=137 μm, Standard deviation = 43.5, Number of measurements = 12965. Measurement by optical particle analyzer (Clemex PS3 Research System, Clemex Technologies Inc., Longueuil, Quebec, Canada).

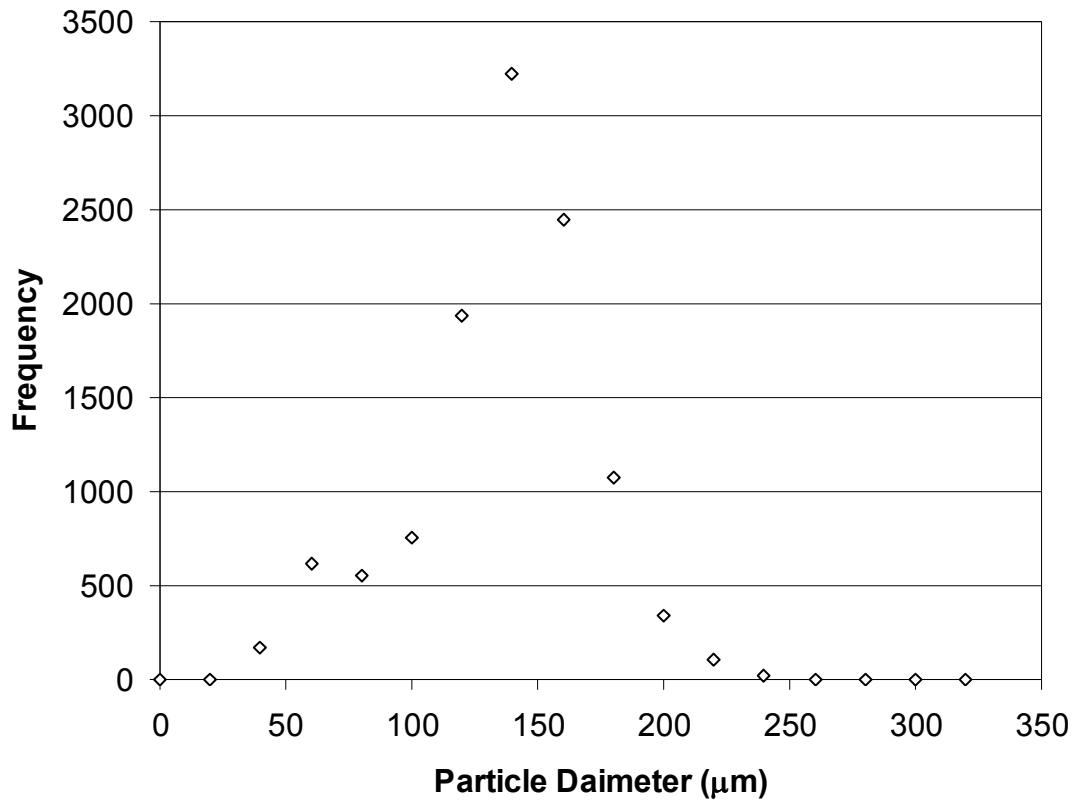


Figure G 2 Particle size distribution of nominally 100 μm particle Al₂O₃, average diameter=126 μm, Standard deviation = 35, Number of measurements = 9702. Shadowgraphy measurements using a laser shadowgraphy system (LaVision GmbH, Goettingen, Germany).

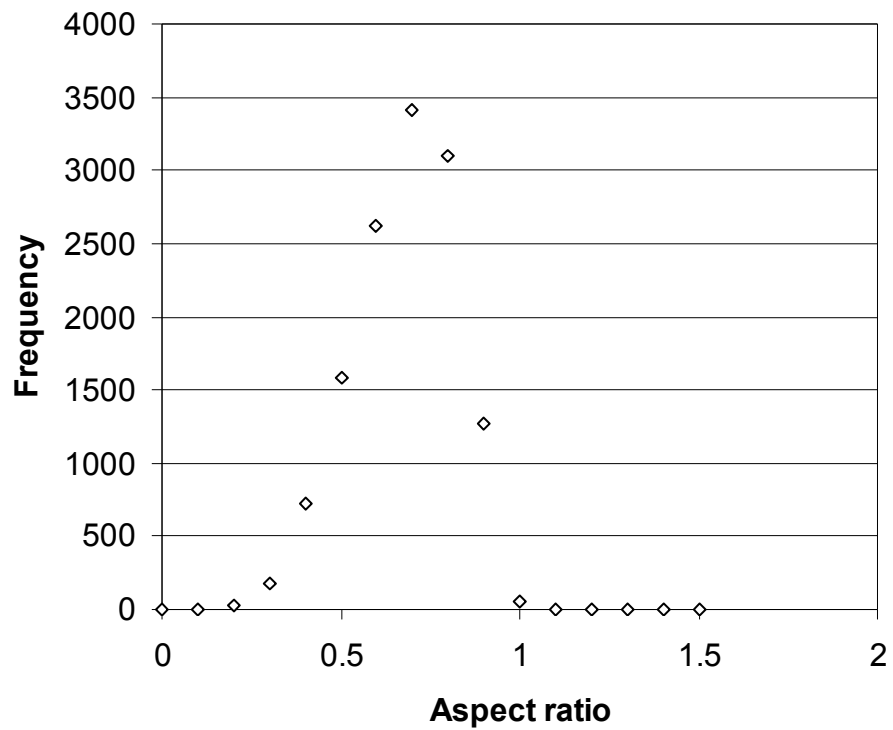


Figure G 3 Aspect ratio distribution of nominally 100 μm Al_2O_3 particle, average aspect ratio=0.55, Standard deviation = 0.14. Number of measurements = 12965. Measurement by optical particle analyzer (Clemex PS3 Research System, Clemex Technologies Inc., Longueuil, Quebec, Canada).

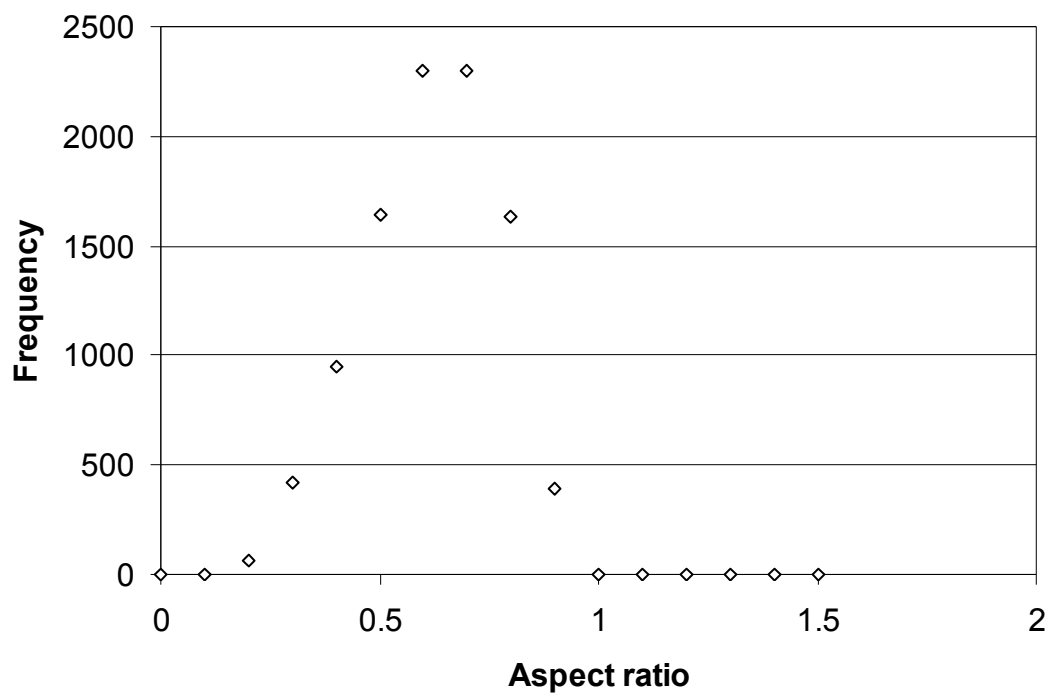


Figure G 4 Aspect ratio distribution of nominally 100 μm particle Al₂O₃, average aspect ratio=0.57 μm, Standard deviation = 0.15, Number of measurements = 9702. Shadowgraphy measurements using a laser Shadowgraphy system (LaVision GmbH, Goettingen, Germany).

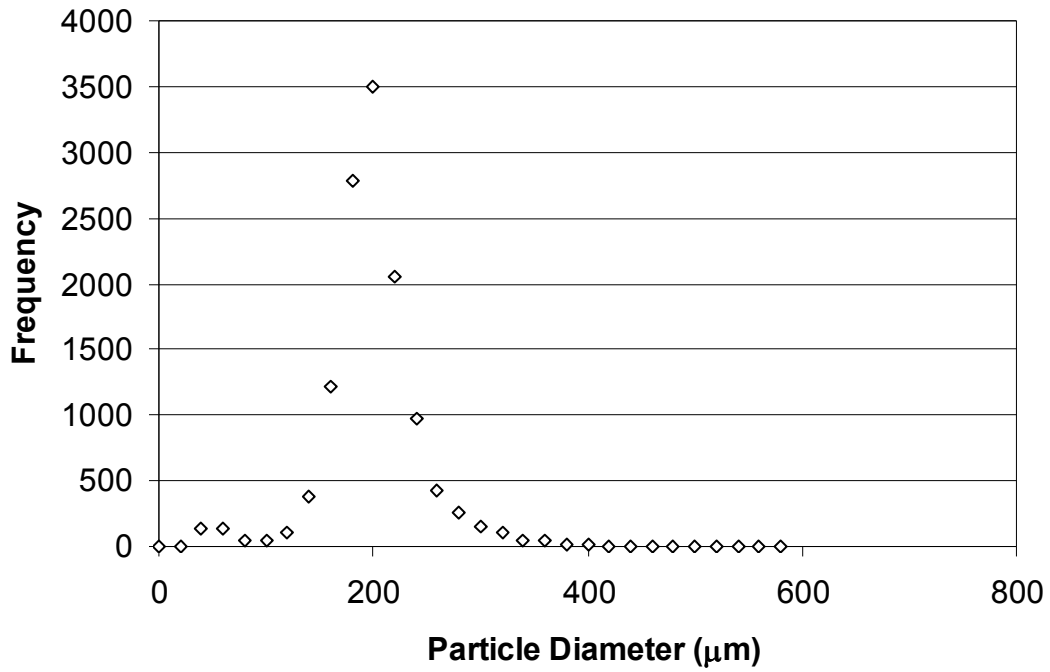


Figure G 5 Particle size distribution of nominally 150 μm particle Al₂O₃, average diameter=189 μm, Standard deviation = 44, Number of measurements = 12433. Measurement by optical particle analyzer (Clemex PS3 Research System, Clemex Technologies Inc., Longueuil, Quebec, Canada).

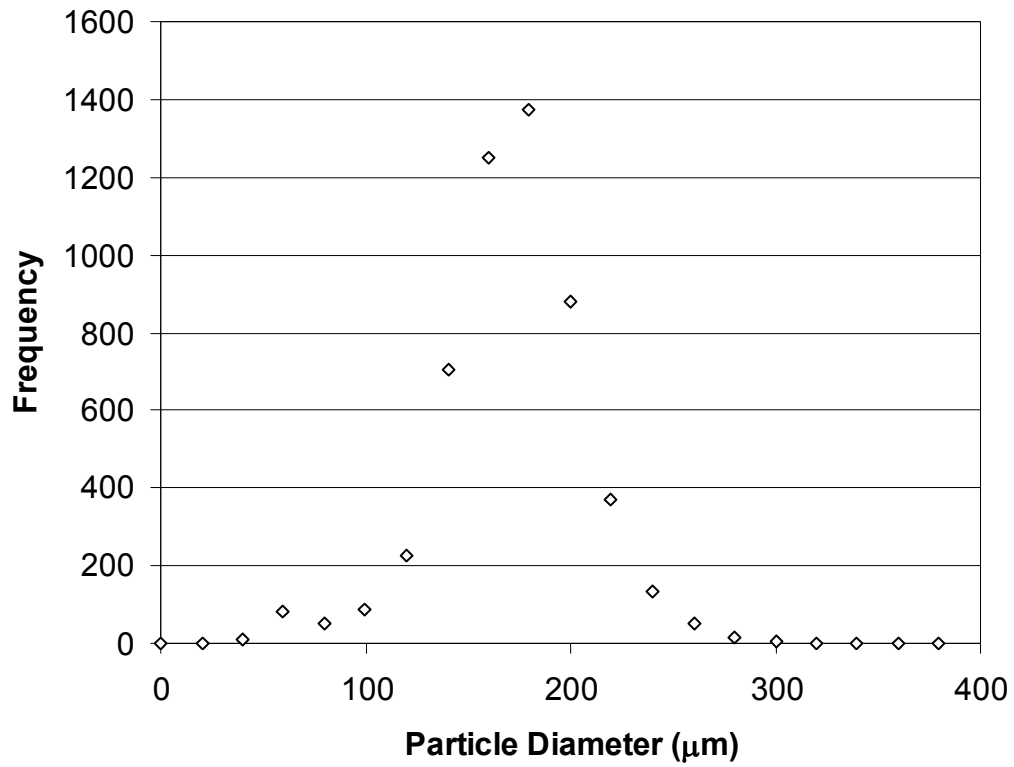


Figure G 6 Particle size distribution of nominally 150 μm particle Al₂O₃, average diameter=162 μm, Standard deviation = 35, Number of measurements = 5211. Shadowgraphy measurements using a laser shadowgraphy system (LaVision GmbH, Goettingen, Germany).

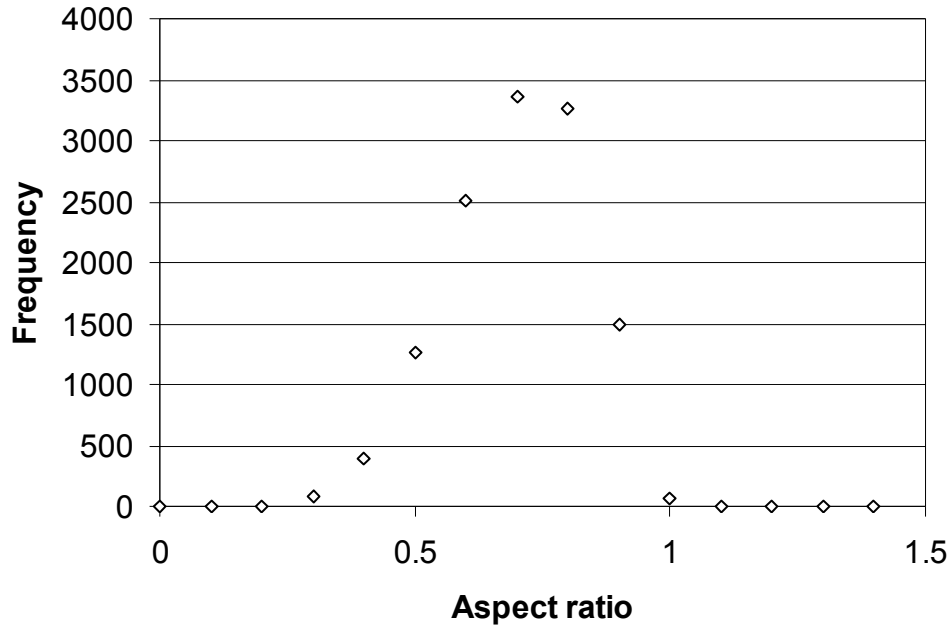


Figure G 7 Aspect ratio distribution of 150 μm Al_2O_3 particle, average aspect ratio=0.54, Standard deviation = 0.12. Number of measurements = 12433. Measurement by optical particle analyzer (Clemex PS3 Research System, Clemex Technologies Inc., Longueuil, Quebec, Canada).

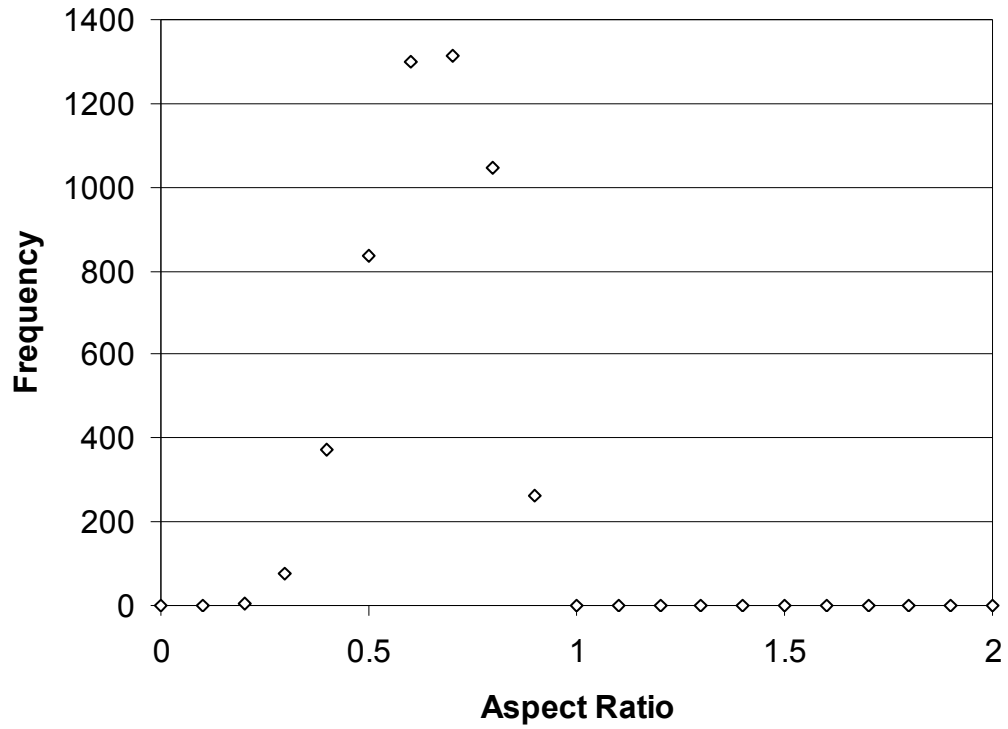


Figure G 8 Aspect ratio distribution of nominally 150 μm particle Al_2O_3 , average aspect ratio=0.6 μm , Standard deviation = 0.13, Number of measurements = 5211. Shadowgraphy measurements using a laser Shadowgraphy system (LaVision GmbH, Goettingen, Germany).

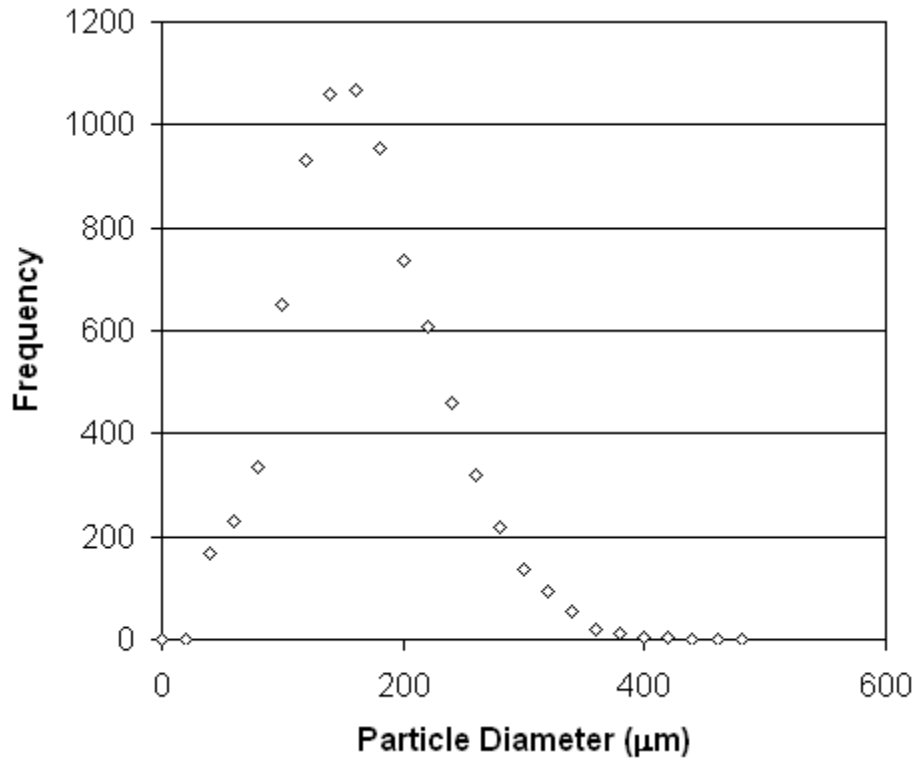


Figure G 9 Particle size distribution of 136 μm garnet particle, average diameter=158 μm, Standard deviation = 63, Number of measurements = 8068. Measurements using optical particle size analyser (Clemex PS3 Research System, Clemex Technologies Inc., Longueuil, Quebec, Canada).

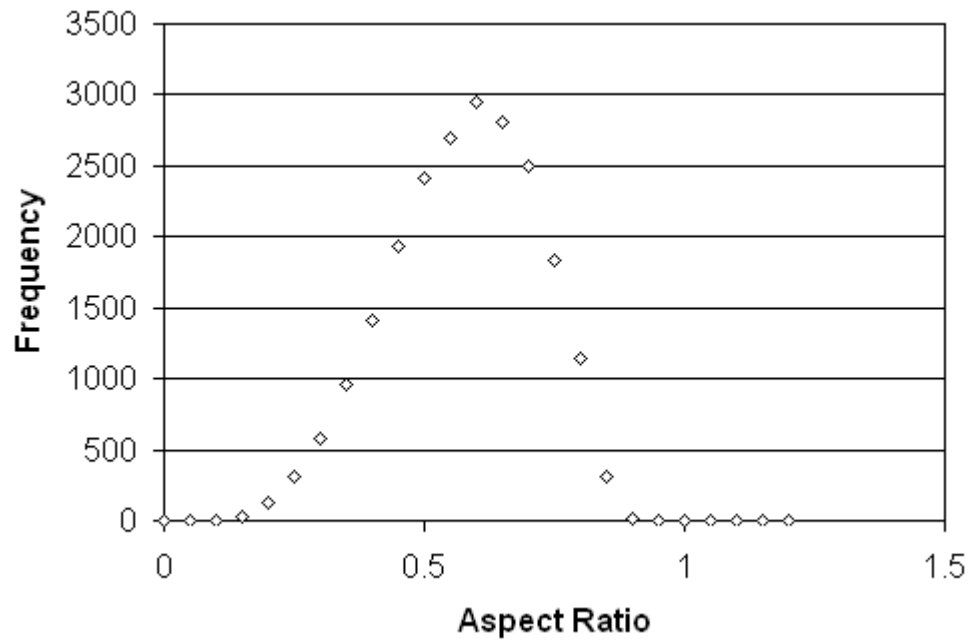


Figure G 10 Particle size distribution of 103 μm garnet particle, average diameter=114 μm , Standard deviation = 25, Number of measurements = 8686. Measurements using optical particle size analyser (Clemex PS3 Research System, Clemex Technologies Inc., Longueuil, Quebec, Canada).

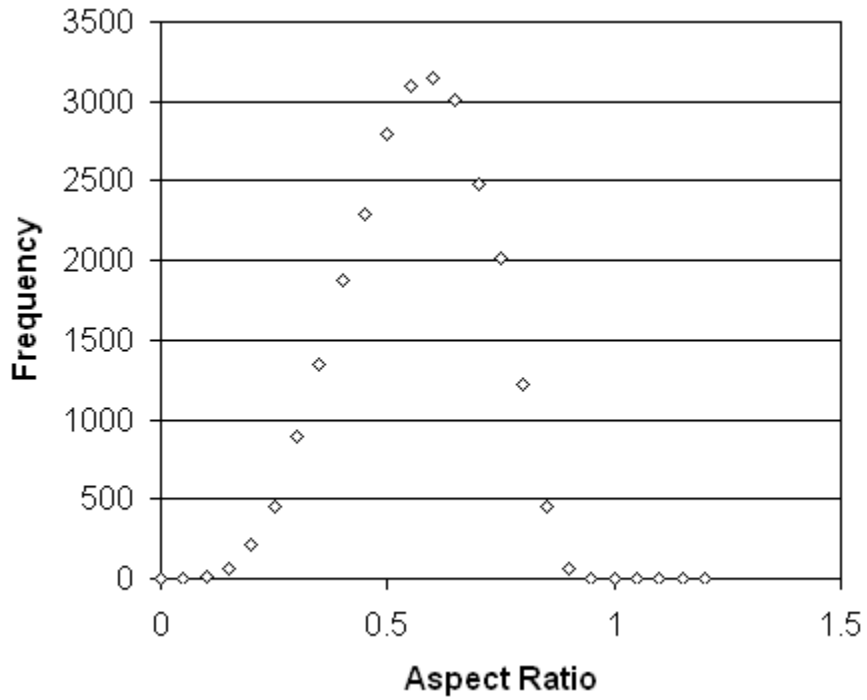


Figure G 11 Aspect ratio distribution of 136 μm garnet particle, average aspect ratio=0.62 μm , Standard deviation = 0.13, Number of measurements = 25461. Measurements using optical particle size analyser (Clemex PS3 Research System, Clemex Technologies Inc., Longueuil, Quebec, Canada).

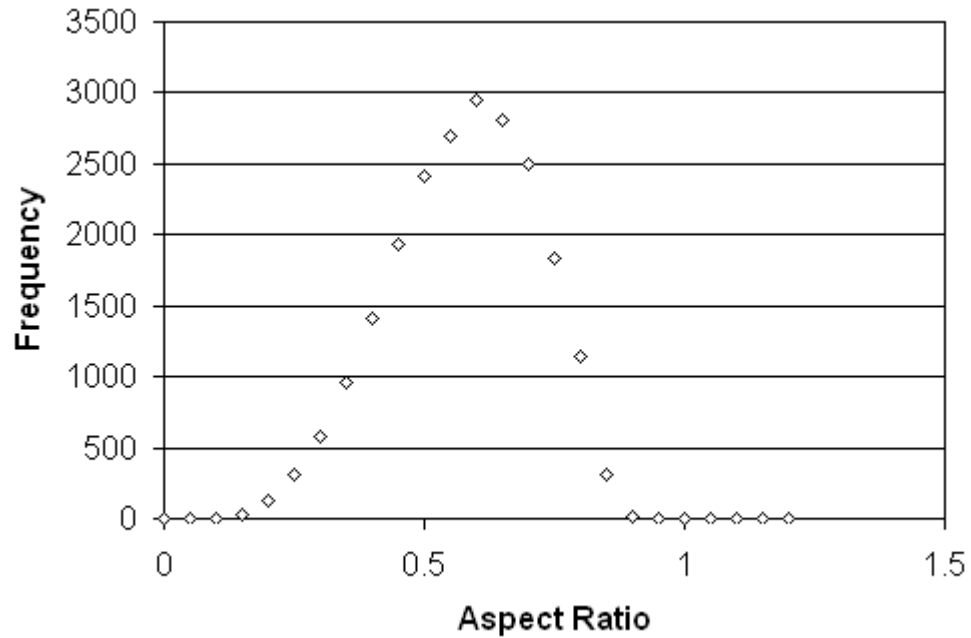


Figure G.12 Aspect ratio distribution of 103 μm garnet particle, average aspect ratio=0.65 μm , Standard deviation = 0.12, Number of measurements = 22025. Measurements using optical particle size analyser (Clemex PS3 Research System, Clemex Technologies Inc., Longueuil, Quebec, Canada).

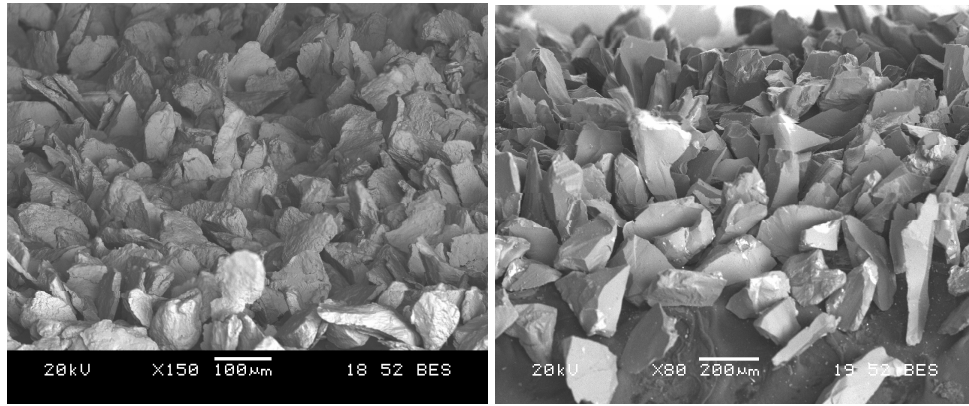
Table G.1 summarizes the measured particle diameters and aspect ratios. The aspect ratios measured using the laser shadowgraphy and the optical particle analyser were found to be very close, with maximum difference of 11 % for Al_2O_3 150 μm particles.

Table G 1 Summary of measured particle sizes and aspect ratios. Numbers in brackets indicate the number of particles measured. Diff.: Difference, Clemex: measured using optical size analyzer, Diff=2 x abs(Clemex-Shadowgraphy)/ Clemex+Shadowgraphy).

Particle	Nominal Diameter (μm)	Measured particle Diameter (μm)			Aspect ratio		
		Method of measurement			Method of measurement		
		Clemex	Shadowgraphy	Diff. (%)	Clemex	Shadowgraphy	Diff. (%)
Al ₂ O ₃	150	189±44 (12433)	162±35 (5211)	15	0.54±0.14	0.60±0.13	11
Al ₂ O ₃	100	137±43 (12965)	126±35 (9702)	8	0.55±0.15	0.57±0.15	4
Garnet	136	158±63 (8068)	136±70 (25461)	15	0.62±0.13	0.66±0.12	6
Garnet	103	114±25 (8686)	103±31 (39992)	10	0.65±0.12	0.66±0.13	2

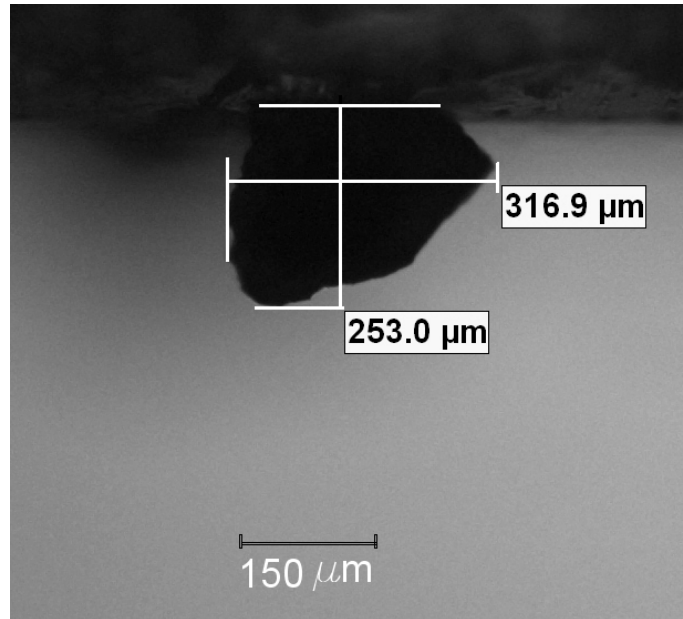
Appendix H **Blocky Particle Selection**

Generally, during solid particle erosion, particles arrive at the target with random orientations. If particles are flaky, they are more likely to strike the target on their flat side. In the present work (model of Chapter 6), it was assumed that the particles strike the target with their sharp edges. Therefore, blocky particles that have greater possibility of striking a target with their sharp edge and that can be represented by collection of rhomboids were used in the impact experiments. In addition to examining garnet particles, other particles were evaluated in order to select the blockiest particle as described in Section 6.1.1. Figs. H1a and H1b show SEM images of Grittal[®] (high chromium alloyed stainless steel grit, Vulkan-INOX, Germany) and Al₂O₃ particles obtained at an inclination of 75° to the mounting plane. In Fig. H1 c an optical microscope was used to measure the dimensions of garnet particles adhering to an adhesive tape in two perpendicular planes; when viewed from above and from the side. The ratio of the average dimensions of 61 measurements taken in these two planes was found to be 0.86. All observations showed that garnet particles were the blockiest particles.



(a)

(b)



(c)

Figure H 1 Qualitative comparison of particles (a) Grittall® particles placed on inclined, SEM at 75° incidence to the detector, (b) Al₂O₃ particles placed on inclined, SEM at 75° incidence to the detector and (c) garnet particle observed from side under optical microscope.

Appendix I Matlab[®] Program for Calculation of Randomly Selecting Area and Aspect Ratio Distributions and Calculating Rhombus Geometries

The model of [68, 69] used in Chapter 6 to determine the first embedding criterion required input parameters; particle angularity (A), impact angle (α), orientation angle (θ), side length (h) and incident velocity (V_i). A program was written in Matlab R2010 (Mathworks), which calculated A and h and assigned a random orientation, θ , in the range -90° - 90° to each particle from the shadowgraphic data sets for the 136 μm and 103 μm particles. The program and samples of the rhombi constructed are given below.

```
clear all;
close all;
clc;
fileName='G:\Embedding experiments\For embedding paper 2\Garnet 106 um and less particles\Input_for_matlab_2';
a=xlsread(fileName);
AR=a(:,1);
AREA=a(:,2);
velocity=a(:,3);
Y=sqrt(2.*AREA./AR);
X=AR.*Y;
H=sqrt((0.5.*AR.*Y).^2+(0.5.*Y).^2);
A=atan(Y./(AR.*Y))*180./pi;
Orientation=[-90:1:90]';
B=[Y,X,H,A,velocity];
numRows = size(B, 1);
shuffledRows = randperm(numRows);
RandomRows = B(shuffledRows(1:10), :);
numRows2 = size(Orientation, 1);
shuffledRows2 = randperm(numRows2);
RandomRows2 = Orientation(shuffledRows2(:, :));
Thetas=RandomRows2(randperm(10),:);
Velo=velocity(randperm(10),:);
Thetas2=Thetas(:,1).*180/pi;
Angularity=RandomRows(:,4).*180/pi;
RandomRows3=[RandomRows,Thetas];
Y2=RandomRows3(:,1);
X2=RandomRows3(:,2);
C1=-0.5.*X2;
D11=zeros(10,1);
C2=0.5.*X2;
D22=zeros(10,1);
D1=-0.5*Y2;
C11=zeros(10,1);
D2=0.5*Y2;
C22=zeros(10,1);
BB1=[C1,C11,C2,C22,C1];
BB2=[D11,D1,D22,D2,D11];
```

```

B3=BB1(1,:);
B4=BB2(1,:);
B5=BB1(2,:);
B6=BB2(2,:);
B7=BB1(3,:);
B8=BB2(3,:);
B9=BB1(4,:);
B10=BB2(4,:);
B11=BB1(5,:);
B12=BB2(5,:);
B13=BB1(6,:);
B14=BB2(6,:);
B15=BB1(7,:);
B16=BB2(7,:);
B17=BB1(8,:);
B18=BB2(8,:);
B19=BB1(9,:);
B20=BB2(9,:);
B21=BB1(10,:);
B22=BB2(10,:);
ROHOMBUSES=plot(B3,B4,B5,B6,B7,B8,B9,B10,B11,B12,B13,B14,B15,B16,B17,B18,B19,B20,B21,B22);
SideLength=RandomRows3(:,3);
Angul=RandomRows3(:,4);
Velocity=RandomRows3(:,6);
RandomOrientation=RandomRows3(:,7);
xlabel('X (um)')
ylabel('Y (um)')
title ('Randomly generated rhombi')
ydir = [0 1 0];
zdir = [0 0 1];
center = [0 0 0];
(' SideLength Angularity Velocity Orientation')
ParticlePropertiesAndLaunchConditions=[SideLength,Angul,Velo,RandomOrientation]
dlmwrite('ParticlePropertiesAndLaunchConditions', ParticlePropertiesAndLaunchConditions, 't')

```

Examples of generated rhombi are shown below.

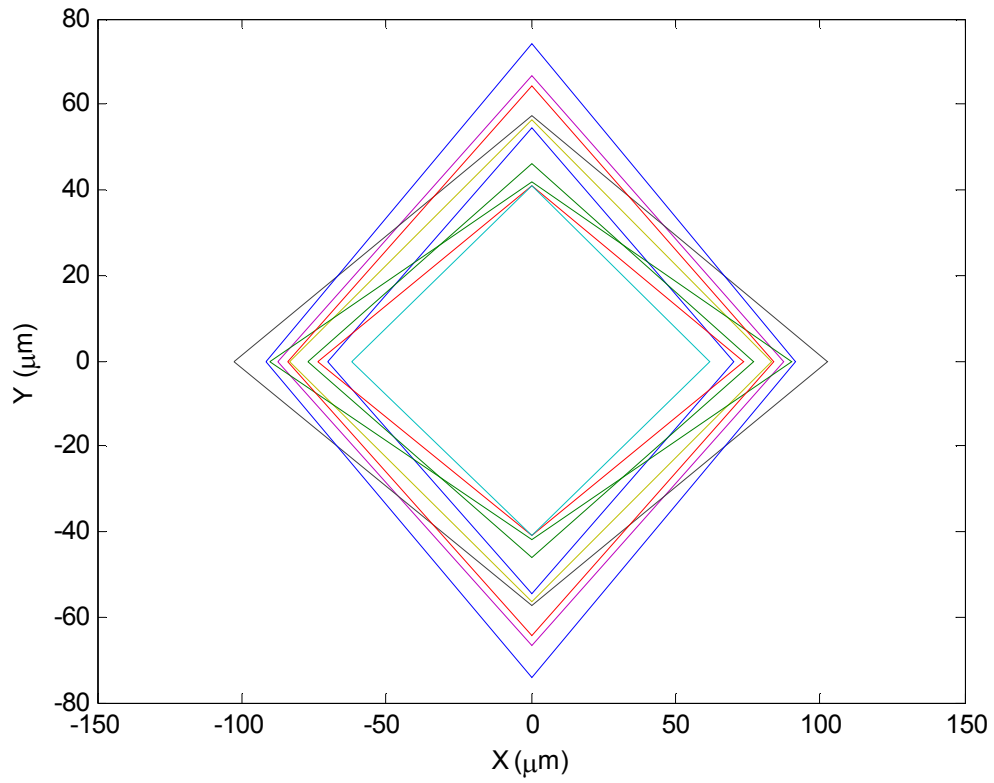


Figure I 1 Randomly generated rhombi (equivalent of 103 μm nominal diameter garnet particles)

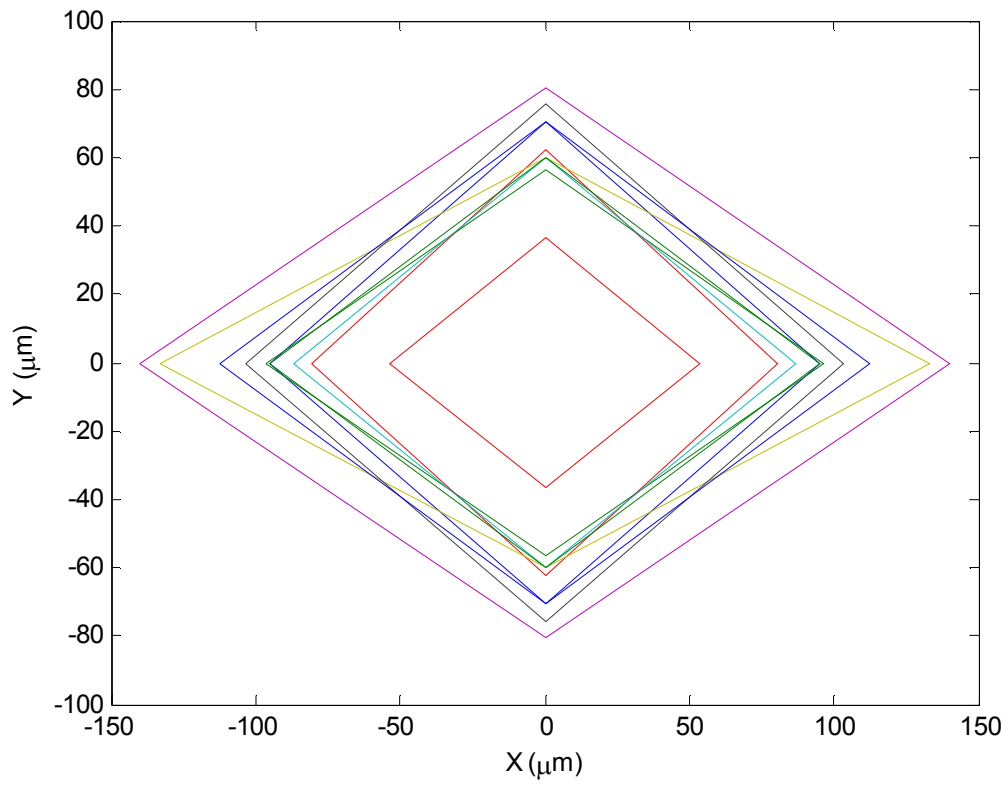


Figure I 2 Randomly generated rhombi (equivalent of 103 μm nominal diameter garnet particles).

10 References

- [1] C. A. Mills, E. Martinez, F. Bessueille, G. Villanueva, J. Bausells, J. Samitier, A. Errachid, Production of structures for micro-fluidics using polymer imprint techniques, *Microelectronic Engineering* 78–79 (2005) 695–700.
- [2] S. Lai, L. J. Lee, L. Yu, K. W. Koelling, M. J. Madou, Micro- and nano-fabrication of polymer based micro-fluidic platforms for bioMEMS applications, *Proceedings of the Materials Research Society Symposium* 729 (2002) U1.7.1- U1.7.11.
- [3] B. Holger, E. L. Laurie, Polymer micro-fluidic devices, *Talanta* 56 (2002) 267–287.
- [4] C. Liu, J. Chen, J. Engel, J. Zou, X. Wang, Z. Fan, K. Ryu, K. Shaikh and D. Bullen, Polymer micro-machining and applications in sensors, micro-fluidics and nanotechnology, *226th National Meeting of the American Chemical Society (ACS)* (2003) 11–17.
- [5] D. Sameoto, M. Hamidi, M. Parameswaran, Characterization of work and power efficiency of micro-machined polymer thermal actuators, *the Canadian Conference on Computer and Electrical Engineering 2007*, Vancouver, BC (2007) 1441-1444.
- [6] A. Taberham, M. Kraft, M. Mowlem and H. Morgan, The fabrication of lab-on-chip devices from fluoropolymers, *J. Microelectronics and Microengineering* 18 (2008) doi:10.1088/0960-1317/18/6/064011.
- [7] A. Brandstadter, K. C. Goretta, J. J. Routbort, D. P. Groppi and K. R. Karasek, Solid-particle erosion of bismaleimide polymers, *Wear*, 147 (1991) 155-164.
- [8] B. deJong, R. Ankone, G. H. Lammertink and M. Wessling, New replication technique for the fabrication of thin polymeric micro-fluidic devices with tunable porosity, *Lab on a Chip* (2005) DOI: 10.1039/b509280a.
- [9] J. C. Lotters, W. Olthuis, P. H. Veltink and P. Bergveld, The mechanical properties of the rubber elastic polymer polydimethylsiloxane for sensor applications, *J. Microelectronics and Micro-engineering* 7 (1997) 145-147.

- [10] G. Wang, J. Xu, Y. Chen, L. Zhang, D. Wang and G. Chen, Fabrication of poly(methylmethacrylate) capillary electrophoresis micro-chips by *in situ* surface polymerization, *Lab on Chip* (2007) DOI 10.1039/b515842g.
- [11] H. Getu, A. Ghobeity, J. K. Spelt and M. Papini, Abrasive jet micro-machining of polymethylmethacrylate, *Wear* 263 (2007) 1008-1015.
- [12] H. Getu, A. Ghobeity, J. K. Spelt and M. Papini, Abrasive jet micro-machining of acrylic and polycarbonate polymers at oblique angles of attack, *Wear* 265 (2008) 888-901.
- [13] L. Chen, G. Luo, K. Liu, J. Ma, B. Yao, Y. Yan and Y. Wang, Bonding of glass-based chips at low or room temperature in routine laboratory, *Optics and Actuators B* 119 (2006) 335-344.
- [14] S. Lathabai, M. Ottmuller, I. Fernandez, Solid particle erosion behaviour of thermal sprayed ceramic, metallic and polymer coatings, *Wear* (1998) 93-108.
- [15] J.G. A. Bitter, A study of erosion phenomena part I, *Wear* 6 (1963) 5-21.
- [16] J.G. A. Bitter, A study of erosion phenomena part II, *Wear* 6 (1963) 169-190.
- [17] I. Finnie, Erosion of surfaces by solid particles, *Wear* 3 (1960) 87-103.
- [18] N. M. Barkoula, and J. Karger-Kocsis, Review processes and influencing parameters of the solid particle erosion of polymers and their composites, *Journal of Materials Science* 37 (2002) 3807-3820.
- [19] J. K. Lancaster, Material specific wear mechanisms: relevance to wear modeling, *Wear* 141 (1990) 159 – 183.
- [20] R. E. Winter and I. M. Hutchings, Solid particle erosion studies using single angular particles, *wear* 29 (1974) 181-194.
- [21] P. J Slikkerveer and F. H in't Veld, Model for patterned erosion, *Wear* 233-235 (1999) 377-386.
- [22] K. V. Pool, C. K. H. Dharan, I. Finnie, Erosive Wear of Composite Materials, *Wear* 107 (1) (1986) 1 - 12.
- [23] M. Roy, B. Vishwanathan and G. Sundararajan, The solid particle erosion of polymer matrix composites, *Wear* 171 (1994) 149–161.

- [24] H. Uuemois, I. Kleis, A critical analysis of erosion problems which have been little studied, *Wear* 31 (1975) 359–371.
- [25] J. C. Arnold and I. M. Hutchings, Flux rate effects in the erosive wear of elastomers, *Journal of Materials Science* 24 (3) (1989) 833-839.
- [26] P. H. Shipway and I. M. Hutchings, A method for optimizing the particle-flux in erosion testing with a gas-blast apparatus, *Wear* 174 (1-2) (1994) 169-175.
- [27] Y.I. Oka, H. Ohnogi, T. Hosokawa, M. Matsumura, The impact angle dependence of erosion damage caused by solid particle impact, *Wear* 203-204 (1997) 573-579.
- [28] I. Finne, G. R. Stevick and J. R. Ridgely, The influence of impingement angle on the erosion of ductile metals by angular abrasive particles, *Wear* 152 (1992) 91-98.
- [29] P. J. Slikkerveer, P. C. P. Bouten, F. C. M. de Hass, High Quality mechanical etching of brittle materials by powder blasting, *Sensors and Actuators* 85 (2000) 296-303.
- [30] R. I. Trezona, M. J. Pickles, I. M. Hutchings, A full factorial investigation of the erosion of durability of automotive clearcoats, *Tribology International* 33 (2000) 559-571.
- [31] P. V. Rao, S. G. Young and D. H. Buckley, Solid spherical glass particle impingement studies of plastic materials, *NASA Tech. Paper 2161* (1983) 1-21.
- [32] A. Brandstadter, K.C. Goretta, J. J. Routbort, D. P. Groppi and K. R. Karasek, Solid-particle erosion of bismaleimide polymers, *Wear* 147 (1991) 155-164.
- [33] S. M. Walley, and J. E. Field, The erosion and deformation of Polyethylene by solid-particle impact, *Philosophical transactions of the royal society of London. Series A, Mathematical and physical sciences*, 321 (1558) (1987) 277-303.
- [34] Y. I. Oka, M. Matsumura and T. Kawabata, Relationship between surface hardness and erosion damage caused by solid particle impact, *Wear* 162-164 (1993) 688-695.
- [35] P. J. Slikkerveer, M. H. A. vanDongen, F. J. Touwslager, Erosion of elastomeric protective coatings, *Wear* 236 (1999) 189-198.
- [36] I. M. Hutchings, D. W. T. Deuchar and A. H. Muhr, Erosion of unfilled elastomers by solid particle impact, *J. Mat. Sci.* 22 (1987) 4071-4076.

- [37] J. Li, and I. M. Hutchings, Resistance of cast polyurethane elastomers to solid particle erosion, *Wear* 135-2 (1990) 293-303.
- [38] G. P. Tilly, Erosion caused by airborne particles, *Wear* 14 (1969) 63-79.
- [39] I. Oka, K. Okamura, T. Yoshida, Practical estimation of erosion damage caused by solid particle impact Part 2: Mechanical properties of materials directly associated with erosion damage, *Wear* 259 (2005) 102-109.
- [40] G. Sundararajan, M. Roy, B. Venkataraman, Erosion efficiency: a new parameter to characterize the dominant erosion micro-mechanism, *Wear* 140 (2) (1990) 369-381.
- [41] S. N. Ratner, I. I. Farberoua, O. V. Radyukeuich and E. G. Lure, Correlation between wear resistance of plastics and other mechanical properties, in *Abrasion of Rubber*, edited by D. I. James, MacLaren, London (1967) 145-154.
- [42] J. C. Arnold, I. M. Hutchings, Erosive wear of rubber by solid particles at normal incidence, *Wear* 161 (1-2) (1993) 213-221.
- [43] B. F. Levin, K. S. Vecchio, J. N. DuPont and A. R. Marder, Modeling solid-particle erosion of ductile alloys, *Metallurgical and Materials Transactions A*, Volume 30 (1999) 1763-1774.
- [44] K. Friedrich, Erosive wear of polymer surfaces by steel blasting, *J. Mat. Sci.* 21 (1986) 3317-3332.
- [45] O. Yano and H. Yamaoka, Cryogenic properties of polymers, *Prog. Polym. Sci.* 20 (1995) 585-613.
- [46] J. Rösler, H. Harders, M. Bäker, Mechanical behaviour of engineering materials: metals, ceramics, polymers and composites, Springer Berlin Heidelberg 2007.
- [47] R. P. Reed, R.E., Schramm and A. F. Clark, Mechanical, thermal, and electrical properties of selected polymers, *Cryogenics* 13 (1973) 67-82.
- [48] A. Hiltner E. Baer, Mechanical properties of polymers at cryogenic temperatures: relationships between relaxation, yield and fracture processes, *POLYMER* 15 (1974) 804-813.

- [49] C. A. Mills, E. Martinez, F. Bessueille, G. Villanueva, J. Bausells, J. Samitier, A. Errachid, Production of structures for microfluidics using polymer imprint techniques, *Microelectronic Engineering* 78–79 (2005) 695–700.
- [50] B. Holger, E. L. Laurie, Polymer microfluidic devices, *Talanta* 56 (2002) 267–287.
- [51] S. Lai, L. J. Lee, L. Yu, K. W. Koelling, M. J. Madou, Micro- and nano-fabrication of polymer based microfluidic platforms for bioMEMS applications, *Proceedings of the Materials Research Society Symposium*, 729 (2002) U1.7.1- U1.7.11.
- [52] C. Zhang, C. Yang, D. Ding, Deep reactive ion etching of PMMA, *Applied Surface Science* 227 (2004) 139–143.
- [53] S. S. Hsieh, J. K. Kuo, C. F. Hwang, H. H. Tsai, A novel design and micro-fabrication for a micro PEMFC, *Microsystem Technologies* 10 (2004) 121–126.
- [54] N. Brown, M. Parrish, Effect of liquid nitrogen on the tensile strength of Polyethylene and Polytetrafluoroethylene, *Polymer letters edition* 10 (1972) 777-779.
- [55] P. Beardmore, S. Rabinowitz, Low Temperature crazing in amorphous polymers, *Journal of Materials Science* (1971) 80-85.
- [56] K. Mizutani, Temperature dependence of fracture toughness of poly(methyl methacrylate), *Journal of Materials Science, Letters* 6 (1987) 915- 916.
- [57] N. R. Dhar, S. Paul, A. B. Chattopadhyay, Role of cryogenic cooling on cutting temperature in turning steel, *Journal of Manufacturing Science and Engineering* 124 (1) (2002) 146-154.
- [58] K. A. Venugopal, S. Paul, A. B. Chattopadhyay, Tool wear in cryogenic turning of Ti-6Al-4V alloy, *Cryogenics* 47 (2007) 12–18.
- [59] M. K. Muju and A.K. Pathak, Abrasive jet machining of glass at low temperature, *Journal of Mechanical Working Technology* 17 (1998) 325-332.
- [60] D. P. Weston, P. H. Shipway, S. J. Harris, Coating removal from an industrial polypropylene blend by cryogenic blasting: the development of substrate damage, *Wear* 258 (2005) 392–401.
- [61] G. Spur, E. Uhlmann, F. Elbing, Dry-ice blasting for cleaning: process, optimization and application, *Wear* 233–234 (1999) 402.

- [62] D. M. Brewis, G. W. Critchlow, C. A. Curtis, Cryoblasting as a pretreatment to enhance adhesion to aluminum alloys: an initial study, *International Journal of Adhesion and Adhesives* 19 (1999) 253-256.
- [63] J. Day, X. Huang and N. L. Richards, Examination of a grit-blasting process for thermal spraying using statistical methods, *Journal of Thermal Spray Technology* 14 (4) (2005) 471-479.
- [64] A. W. Momber, Y. C. Wong, E. Budidharma and R. Tjo, Surface profiling of low-carbon steel with supersonic waterjets, *Wear* 249 (2002) 853–859.
- [65] S. S. Rajahram, T. J. Harvey, J. C. Walker, S. C. Wang, R. J. K. Wood, Investigation of erosion-corrosion mechanisms of UNS S31603 using FIB and TEM, *Tribology International* 46 (1) (2012) 161-173.
- [66] R. Brown and J. W. Edington, Subsurface defect structure of eroded copper single crystals, *Wear* 72 (1981) 377 – 381.
- [67] R. Brown and J. W. Edington, The melting of metal targets during erosion by hard particles, *Wear* 71 (1981) 113 – 118.
- [68] M. Papini and J. K. Spelt, Impact of rigid angular particles with fully-plastic targets Part I: Analysis, *International Journal of Mechanical Sciences* 42 (2000) 991-1006.
- [69] M. Papini and J. K. Spelt, Impact of rigid angular particles with fully-plastic targets Part II: Parametric study of erosion phenomena, *International Journal of Mechanical Sciences* 42 (2000) 1007-1025.
- [70] J. B. Zu, G. T. Burstein and I. M. Hutchings, A comparative study of slurry erosion and free-fall particle erosion of aluminum, *Wear* 149 (1991) 73-84.
- [71] J. J. Kim, Erosion of a reaction bonded silicon nitride, *Journal of Materials Science* 39 (2004) 3849-3851.
- [72] J. Zhou and S. Bahadur, Erosion-corrosion of Ti-6Al-4V in elevated temperature air environment, *Wear* 186-187 (1995) 332-339.
- [73] A. F. Harris, A. Beevers, The effects of grit-blasting on surface properties for adhesion, *International Journal of Adhesion & Adhesives* 19 (1999) 445-452.

- [74] N. Y. Sari, Influence of erodent particle types on solid particle erosion of polyphenylene sulphide composite under low particle speed, *Polymer Composite* (2009) 1442-1449.
- [75] S. Amada, T. Hirose, T. Senda, Quantitative evaluation of residual grits under angled blasting, *Surface and Coatings Technology* 111 (1999) 1–9.
- [76] A. Gröbl, A. Kolb, G. Reinisch, G. Fafilek, G. Skrbensky, R. Kotz, Characterization, quantification, and isolation of aluminum oxide particles on grit blasted titanium aluminum alloy hip implants, *J. Biomed. Mater. Res. B: Appl Biomater.* 83B (2007)127–131.
- [77] F. Negri, E. Bedel, P. Schmitz, Experimental study of alumina particle removal from a plane surface, *The Journal of Adhesion* 78 (2002) 79-95.
- [78] C. Toscano and G. Ahmadi, Particle removal mechanisms in cryogenic surface cleaning, *The Journal of Adhesion*, 79 (2003) 175 – 201.
- [79] A. Ghobeity, H. Getu, T. Krajac, J. K. Spelt, M. Papini, Process repeatability in abrasive jet micro-machining, *Journal of Materials Processing Technology* 190 (1–3) (2007) 51–60.
- [80] H. Getu, J. K. Spelt and M. Papini, Cryogenically assisted abrasive jet micro-machining of Polymers, *J. of Microelectronics and Microengineering* 18 (2008), doi:10.1088/0960-1317/18/11/115010.
- [81] H. Getu, J. K. Spelt and M. Papini, Erosion rate enhancement in the abrasive jet micro-machining of polymers and elastomers, 1st international conference on abrasive processes, Cambridge, UK, September 21-25 (2008).
- [82] A. Ghobeity, D. Ciampini, and M. Papini, An analytical model of the effect of particle size distribution on the surface profile evolution in abrasive jet micro-machining, *Journal of Materials Processing Technology* 209 (20) (2009) 6067-6077.
- [83] P. H. Shipway and I. M. Hutchings, Measurement of coating durability by solid particle erosion, *Surface and Coatings Technology* 71 (1995) 1-8.
- [84] P. H. Shipway, The effect of plume divergence on the spatial distribution and magnitude of wear in gas-blast erosion, *Wear* 205 (1997) 169-177.

- [85] P. H. Shipway and D. P. Weston, Thermal effects in blasting and erosion of polymeric materials, *Journal of Materials Processing Technology* 209 (2009) 6161-6167.
- [86] A. N. J. Stevenson and I. M. Hutchings, The influence of nozzle length on the divergence of the erodent particle stream in a gas-blast erosion rig, *Wear* 189 (1995) 66-69.
- [87] K. Anand, S. K. Hovis, H. Conrad, R.O. Scattergood, Flux effects in solid particle erosion, *Wear* 118 (1987) 243–257.
- [88] D. R. Andrews, N. Horsfield, Particle collisions in the vicinity of an eroding surface, *J. Phys. D: Appl. Phys.* 16 (1983) 525–538.
- [89] D. Ciampini, J.K. Spelt and M. Papini, Simulation of interference effects in particle streams following impact with a flat surface, Part I: Theory and analysis, *Wear* 254 (2003) 237-249.
- [90] D. Ciampini, J. K. Spelt and M. Papini, Simulation of interference effects in particle streams following impact with a flat surface, Part II: Parametric study and implications for erosion testing and blast cleaning, *Wear* 254 (2003) 250-264.
- [91] M. Papini, D. Ciampini, T. Krajac and J. K. Spelt, Computer modeling of interference effects in erosion testing: effect of plume shape, *Wear* 255 (1-6) (2003) 85-97.
- [92] W. D. Bachalo, M. J. Houser, Phase Doppler spray analyzer for simultaneous measurements of drop size and velocity distributions, *Opt. Eng.* 23 (1984) 583–590.
- [93] N. Miyazaki and N. Takeda, Solid particle erosion of fibre reinforced plastics. *J. Comp. Mater.* 27 (1993) 21–31.
- [94] A. Ghobeity, H. Getu, M. Papini, J. K. Spelt, Abrasive jet micro-machining of glass and Polymethylmethacrylate: Surface Evolution Models, 5th Canadian Workshop on MEMS and Microfluidics (*CWMEMS 2007*), Montreal, Canada, August 12-13 (2007).
- [95] S. Arjula, A. P. Harsha, M. K. Ghosh, Solid-particle erosion behaviour of high-performance thermoplastic polymers, *J. Mater. Sci.* 43 (2008) 1757–1768.

- [96] J. H. Neilson, A. Gilchrist, Erosion by a stream of solid particles, *Wear* 11 (1968) 111–122.
- [97] A. C. M. Kuo, J. E. Mark (Editor), Polymer data handbook, Oxford Univ. Press, New York, 999 pp. 411-435.
- [98] I. M. Hutchings and A. Levy, Thermal effects in the erosion of ductile metals, *Wear* 131 (1989) 105-121.
- [99] R. A. Doyle and A. Ball, On thermomechanical effects during solid particle erosion, *Wear* 151 (1991) 87-95.
- [100] A. Ghobeity, T. Krajac, T. Burzynski, M. Papini and J. K. Spelt, Surface evolution models in abrasive jet micro-machining, *Wear*, 264 (3-4), (2008) 185-198.
- [101] H. Getu, J. K. Spelt and M. Papini, Thermal analysis of cryogenically assisted abrasive jet micro-machining of PDMS, *International Journal of Machine Tools and Manufacture* 51 (9) (2011) 721-730.
- [102] H. Getu, J. K. Spelt and M. Papini, Finite element analysis of heat transfer in cryogenically assisted abrasive jet micro-machining of PDMS, *Wear of Materials 2011-18th international conference*, Philadelphia, USA (2011).
- [103] F. W. Schmidt, R. E. Henderson, C. H. Wolgemuth, Introduction to thermal sciences, John Wiley and sons Inc., 1993.
- [104] H. Martin, Heat and mass transfer between impinging gas jets and solid surfaces, in: J. P. Hartnett and T. F. Irvine Jr. (Eds.), *Advances in heat transfer* (1977) 1-60.
- [105] Z. B. Hou and R. Komanduri, General solutions for stationary/moving plane heat source problems in manufacturing and tribology, *International Journal of Heat and Mass Transfer* 43 (10), (2000) 1679-1698.
- [106] A. F. M. Arif, B.S. Yilbas and B. J. Abdul Aleem, Laser Cutting of Thick Sheet Metals: Residual Stress Analysis, *Optics and Laser Technology* 41 (3) (2009) 224-232.
- [107] L. M. Yu, Three-dimensional finite element modelling of laser cutting, *Journal of Materials Processing Technology* 63 (1997) 637-639.

- [108] C. Glynn and D. B. Murray, Jet impingement cooling in microscale, *ECI International Conference on Heat and Fluid Flow in Microscale*, Castelvechio Pascoli, Italy, September 25-30 (2005).
- [109] L. S. Mayboudi, A. M. Birk, G. Zak and P. J. Bates, Laser transmission welding of a lap-joint: thermal imaging observation and three-dimensional finite element modeling, *J. Heat Transfer* 129 (2007) doi:10.1115/1.2740307.
- [110] J. H. M. ten Thije Boonkamp and J. K. M. Jansen, An analytical solution for mechanical etching of glass by powder blasting, *Journal of Engineering Mathematics* 43 (2002) 385–399.
- [111] A. Ghobeity, H. Getu, M. Papini and J. K. Spelt, Surface evolution models for abrasive jet micro-machining of holes in glass and polymethylmethacrylate (PMMA), *Journal of Micromechanics and Microengineering* 17 (2007) 2175-2185.
- [112] B. Schemer, T. Kuriyama, I. Narisawa and K. Friedrich, Simulation of the deformation behaviour and the fracture process of rubber toughened polycarbonate, *Journal of Materials Science Letters* 14 (9) (1995) 660-664.
- [113] M. F. Bukhina and S. K. Kurlyand, Low temperature behaviour of elastomers, Brill Academic Publishers, The Netherlands, Leiden, 2007.
- [114] K. S. Lee, S. J. Park, Y. S. Kim and J. S. Kim, Tensile properties of plastics used in automotive instrument panel over some ranges of strain rates and temperatures, *Proceeding of The 1st International Forum On Strategic Technology "e-Vehicle Technology"*, IFOST 2006 (2006) 112-116.
- [115] A. Govindaraju, A. Chakraborty and C. Luo, Reinforcement of PDMS masters using SU-8 truss structures, *Journal of Micromechanics and Microengineering* 15 (2005) 1303-1309.
- [116] A. Ghobeity, J. K. Spelt and M. Papini, Abrasive jet micro-machining of planar areas and transitional slopes, *Journal of Micromechanics and Microengineering* 18 (2008), doi: 10.1088/0960-1317/18/5/055014.

- [117] A. Ghobeity, M. Papini and J.K. Spelt, Abrasive jet micro-machining of planar areas and transitional slopes in glass using target oscillation, *Journal of Materials Processing Technology* 209 (11) (2009) 5123-5132.
- [118] L. C. Pope and C. W. Ward (editors), Manual on test sieving methods, prepared by ASTM Committee E-29 as guidelines for establishing sieve analysis procedures, ASTM Committee E-29 on Particle and Spray Characterization, 1998.
- [119] D. Dehnadfar, J. Friedman and M. Papini, Laser shadowgraphy measurements of abrasive particle spatial, size and velocity distributions through micro-masks used in abrasive jet micro-machining, *Journal of Materials Processing Technology*, accepted (2011).
- [120] H. Z. Li, J. Wang and J. M. Fan, Analysis and modelling of particle velocities in micro-abrasive air jet, *International Journal of Machine Tools & Manufacture* 49 (11) (2009) 850-858.
- [121] P. H. Shipway and I. M. Hutchings, Influence of nozzle roughness on conditions in a gas-blast erosion rig, *Wear* 162–164 (1993) 148–158.
- [122] I. M. Hutchings, A model for the erosion of metals by spherical particles at normal incidence, *Wear* 70 (3) (1981) 269-281.
- [123] Y. Tirupataiah and G. Sundararajan, A dynamic indentation technique for the characterization of the high strain rate plastic flow behaviour of ductile metals and alloys, *Journal of the Mechanics and Physics of Solids* 39 (2) (1991) 243-271.
- [124] I. M. Hutchings, Deformation of metal surfaces by the oblique impact of square plates, *International Journal of Mechanical Sciences* 19 (1977) 45-52.
- [125] D. C. Montgomery and G. C. Runger, Applied Statistics and Probability for Engineers, 3rd edition, John Wiley and Sons, Inc. USA, 2003.
- [126] D. G. Rickersby and N. H. MacMillan, On the oblique impact of a rigid sphere against a rigid-plastic solid, *Int. J. Mech. Sci.* 22 (1980) 491–494.
- [127] I. M. Hutchings, R. E. Winter and J. E. Field, Solid particle erosion of metals: the removal of surface material by spherical projectiles, *Proc. R. Soc. London A* 348 (1976) 379-392.

- [128] G. Sundararajan, P. G. Shewmon, The oblique impact of a hard ball against ductile, semi-infinite, target materials-experiment and analysis, *Int. J. Impact Eng.* 6(1) (1987) 3–22.
- [129] Ö. Bilgin, Harry E. Stewart, T. D. O'Rourke, Thermal and mechanical properties of polyethylene pipes, *J. Mater. Civ. Eng.* 19 (1043) (2007) 899-1561.
- [130] M. E. Kinsella, B. Lilly, B. E. Gardner, N. J. Jacobs, Experimental determination of friction coefficients between thermoplastics and rapid tooled injection mould materials, *Rapid Prototyping Journal* 11 (3) (2005) 167-73.
- [131] Y. Du and S. Wang, Energy Dissipation in Normal Elastoplastic Impact Between Two spheres, *ASME Journal of Applied Mechanics ASME* 76 (2009) 061010-1-061010-8.
- [132] K. L. Johnson, Contact mechanics, Cambridge University Press 1985.
- [133] S. B. Ratner and E. E. Styller, Characteristics of impact friction and wear of polymeric materials, *Wear* 73 (1981) 213-234.
- [134] H. Getu, J. K. Spelt and M. Papini, Reduction of particle embedding in solid particle erosion of polymers, *Wear* 270 (11-12) 922-928.
- [135] H. Getu, J. K. Spelt and M. Papini, Embedded particle quantification and reduction techniques following solid particle erosion of Polymers, *Wear of Materials 2011-18th international conference*, Philadelphia, USA.
- [136] P. Shewmon and G. Sundararajan, The erosion of metals, *Ann. Rev. Mater. Sci.* 13 (1983) 301-318.
- [137] A. R. daCosta and R. Vilar, Erosion by solid particle impingement: experimental results with cast-iron, laser-treated surfaces, *Tribology Letters* 3 (1997) 379-385.